Search for Standard Model Higgs Boson Produced in Association with a Top-Antitop Quark Pair in 1.96 TeV Proton-Antiproton Collisions

by

Stanley T. Lai

A thesis submitted in conformity with the requirements
for the degree of Doctor of Philosophy
Graduate Department of Physics
University of Toronto

Abstract

Search for Standard Model Higgs Boson Produced in Association with a Top-Antitop Quark Pair in 1.96 TeV Proton-Antiproton Collisions

Stanley T. Lai

Doctor of Philosophy

Graduate Department of Physics

University of Toronto

2007

This thesis describes the first search for Standard Model Higgs boson production in association with a top-antitop quark pair in proton-antiproton collisions at a centre of mass energy of 1.96 TeV. The integrated luminosity for this search corresponds to 319 pb^{-1} of data recorded by the Collider Detector at Fermilab. We outline the event selection criteria, evaluate the event acceptance and estimate backgrounds from Standard Model sources. Three events are observed that satisfy our event selection, while 2.16 ± 0.66 events are expected from background processes. No significant excess of events above background is thus observed, and we set 95% confidence level upper limits on the production cross section for this process as a function of the Higgs mass. For a Higgs boson mass of 115 GeV/c^2, we find that $\sigma_{t\bar{t}H} \times BR(H \to b\bar{b}) < 690$ fb at 95% C.L. These are the first limits set for $t\bar{t}H$ production. This search also allows us to anticipate the challenges and necessary strategies needed for future searches of $t\bar{t}H$ production.

Dedication

(reprinted with permission from S. Harris)

How great are his signs and how mighty are his wonders! His kingdom is an everlasting kingdom, and his dominion is from generation to generation.

Daniel 4:3

To Betty, my love, my life, my hope, and my strength.

Financial support from the University of Toronto and the Province of Ontario is gratefully acknowledged.

Acknowledgements

Pekka: I am forever indebted to you for your supervision, ideas, guidance, patience, understanding, compassion, and your character. You were everything a student could possibly ask for in a supervisor, and I am truly grateful to have had you as a Ph.D. advisor.

Pierre and William: Your advice and insights were invaluable to me, and I sincerely thank you for all your help and assistance.

Bob and David: My thanks to you for being on my committee and providing me with valuable direction and advice.

Oliver und Bernd: Ich möchte mich bei euch bedanken. Ich werde eure Hilfe und Freundschaft immer schätzen.

Tim, Thorsten, Teresa, Simon, Shabnaz, Pascal, Mini-Pierre, Michael, Leslie, Kostas, Ian, Frenchy, Elham, Don, et Dan: Mes amis, merci pour les blagues, les bons temps, votre soutienne, et votre aide.

Betty and Joanna: You are there for me always when I need it. Without your laughter, your company, your presence, my days would have been much darker and joyless.

Mom and Dad: How can I ever repay the support and encouragement you've given me throughout the years? Indeed you have done so much to shape my character, my values, and provided me with all opportunities that any son could ask for. I am always greatly humbled when I think of your sacrifice and generosity and love for your children. God has truly blessed my life to have such great parents.

Jesus of Nazareth, my saviour and redeemer: In you I have placed my life, and in your guidance I trust. My life has been full of great blessings that I am unworthy to receive. May you accept my humble thanks for the people in my life, and may you continue to give me strength and courage as I start another chapter on my life's journey. For I have never known anything so magnificent as your saving grace, the grace upon which I entirely depend. *Sola Gratia, Sola Fide, Solus Christus.*

Stanley Tsai-Ting Lai

Toronto, Ontario, Canada

September 2006

Contents

List of Tables

List of Figures

Chapter 1

Introduction

The field of physics attempts to understand the complexities of nature and the physical phenomena that are observed. In particular, particle physics seeks to understand the constituents of the universe and their interactions at the most fundamental level. Experimental observations over the last century [1] have led to the creation of a theory called the Standard Model of particle physics [2] to explain such physical phenomena.

The Standard Model of particle physics aptly encompasses our knowledge of the fundamental constituents of the universe and their interactions. The Standard Model consists of six quarks and six leptons that constitute the observable matter in the universe, as well as four gauge bosons (photon, gluon, $W^{\pm}$, Z bosons) that mediate interactions between particles. The Standard Model also predicts the existence of a massive, scalar boson called the Higgs boson. The Higgs boson is the only particle predicted by the Standard Model that remains unobserved.

Currently, the only possible place to observe the Higgs boson is at the Fermilab Tevatron, a particle accelerator that collides protons with antiprotons at a centre-of-mass energy of 1.96 TeV. Due to small production cross sections, the Higgs boson is difficult to detect, and searches for the Higgs boson require large data samples and efficient particle identification.

This thesis presents a search for the Higgs boson produced in association with a top quark and an anti-top quark through the interaction process $p\bar{p} \rightarrow t\bar{t}H$. These high energy proton antiproton collisions are produced by the Fermilab Tevatron. This search uses 319 pb^{-1} of data recorded by the upgraded Collider Detector at Fermilab (CDF II).

1.1 The Standard Model of Particle Physics

The Standard Model has enjoyed unprecedented success in predicting fundamental phenomena to a high degree of accuracy [3]. It describes the universe in terms of interacting quantum fields. These fields represent fundamental particles that are divided into two categories: spin-1/2 fermions and spin-1 gauge bosons. The spin-1/2 fermions are comprised of six quarks and six leptons that make up the known matter in the universe. These quarks and leptons are listed in Table 1.1 along with their masses and electric charges. They are also frequently categorized into generations that describe the mass hierarchy between these particles, with the lightest particles belonging to the first generation and the heaviest particles belonging to the third generation. Each lepton generation consists of a charged particle (electron, muon, or tau) and its associated, uncharged, neutrino. Each quark generation is comprised of a quark with an electric charge of $+(2/3)e$, paired with a quark of electric charge -$(1/3)e$.

There are four spin-1 gauge bosons that mediate the interactions between the Standard Model particles. These gauge bosons are listed in Table 1.2, with their respective electric charges and mass. Photons are responsible for mediating the electromagnetic force, the $W^{\pm}$ and Z bosons mediate the weak nuclear force, and the gluons are responsible for mediating the strong nuclear force. The force of gravity is not described by the Standard Model, but due to its extremely weak nature its effect is negligible in the high energy particle interactions that concern us here.

At the heart of the Standard Model lies the concept of electroweak unification, where

Fundamental Fermions (Spin-1/2)					
Quarks			**Leptons**		
Flavor	Charge	Mass [MeV/c^2]	Flavor	Charge	Mass [MeV/c^2]
Up (u)	+2/3	1.5 to 3.0	Electron neutrino (ν_e)	0	$< 1.5 \times 10^{-6}$
Down (d)	−1/3	3 to 7	Electron (e^-)	-1	0.511
Charm (c)	+2/3	(1.0 to 1.4) $\times 10^3$	Muon neutrino (ν_μ)	0	$< 1.9 \times 10^{-4}$
Strange (s)	−1/3	70 to 120	Muon (μ^-)	-1	105.7
Top (t)	+2/3	(174.2 $\pm$ 3.3) $\times 10^3$	Tau neutrino (ν_τ)	0	< 18.2
Bottom (b)	−1/3	(4.2 to 4.7) $\times 10^3$	Tau (τ^-)	-1	1777.1

Table 1.1: Fundamental fermions (quarks and leptons) of the Standard Model [1].

the electromagnetic and weak nuclear forces are described by a single, unified electroweak force that respects the symmetry of the $SU(2) \times U(1)$ gauge group. The electroweak symmetry is broken by the Higgs mechanism [4], whereby a doublet of complex scalar fields breaks the symmetry of the electroweak $SU(2) \times U(1)$ gauge group. This mechanism also gives rise to the masses of the $W^\pm$ and Z gauge bosons. Fermions that interact with the Higgs field also obtain masses that are proportional to their coupling strength with the Higgs field. In addition, the existence of a neutral scalar particle is predicted. Known as the Higgs boson, this is the only particle predicted by the Standard Model that has not yet been observed.

1.2 Electroweak Symmetry Breaking

The fully symmetric $SU(2)_L \times U(1)_Y$ Lagrangian of the Standard Model is given by

$$\mathcal{L} = \overline{\chi}_L \gamma^\mu (i\partial_\mu - g\frac{\tau^a}{2} W_\mu^a - g'\frac{Y}{2} B_\mu)\chi_L + \overline{\psi}_R \gamma^\mu (i\partial_\mu - g' B_\mu)\psi_R - \frac{1}{4} W_{\mu\nu}^a W_a^{\mu\nu} - \frac{1}{4} B_{\mu\nu} B^{\mu\nu}. \quad (1.1)$$

Fundamental Bosons (Spin-1)			
Interaction	Name	Charge	Mass [GeV/c^2]
Electromagnetic	Photon (γ)	0	0
Weak	W boson (W)	1	80.403 ± 0.029
Weak	Z boson (Z)	0	91.1876 ± 0.0021
Strong	Gluon (g)	0	0

Table 1.2: Fundamental bosons of the Standard Model [1].

Here, χ_L are left-handed isospin doublets of fermions, and ψ_R are the right-handed fermion isosinglets. The right-handed fermions are arranged in singlets because the right-handed neutrino does not exist in the Standard Model, since neutrinos are massless in the Standard Model framework. The constants g and g' are the coupling constants of the $SU(2)$ and $U(1)$ gauge groups, respectively, while Y is the $U(1)$ hypercharge. The W_μ^a and τ^a are the three gauge fields and the three generators of the $SU(2)$ group, respectively, while the $U(1)$ gauge boson is given by B_μ. The last two terms in the Lagrangian are the self-energies of gauge bosons ($B_{\mu\nu} = \partial_\mu B_\nu - \partial_\nu B_\mu, \quad W_{\mu\nu} = \partial_\mu W_\nu - \partial_\nu W_\mu$). In the absence of $SU(2)_L \times U(1)_Y$ symmetry breaking, the fermions and gauge bosons have zero mass.

To induce symmetry breaking in the SM, four real self-interacting scalar fields $\phi_i (i = 1, \ldots, 4)$ are introduced and arranged in an isospin doublet with weak hypercharge $Y = 1$:

$$\phi = \begin{pmatrix} \phi^+ \\ \phi^0 \end{pmatrix} \text{ where } \phi^+ = \frac{\phi_1 + i\phi_2}{\sqrt{2}} \text{ and } \phi^0 = \frac{\phi_3 + i\phi_4}{\sqrt{2}}. \tag{1.2}$$

The Lagrangian for these scalar fields is given by

$$\mathcal{L}' = \left| (i\partial_\mu - g\frac{\tau^a}{2} W_\mu^a - g'\frac{Y}{2} B_\mu)\phi \right|^2 + \mu^2 \phi^\dagger \phi - \lambda(\phi^\dagger \phi)^2, \tag{1.3}$$

where the condition $\mu^2 > 0$ and $\lambda > 0$ allows for symmetry breaking.

Choosing a vacuum expectation value of

$$\phi_0 = \sqrt{\frac{1}{2}} \begin{pmatrix} 0 \\ v \end{pmatrix} \tag{1.4}$$

for the scalar isodoublet $\phi(x)$, the scalar fields are shifted such that the scalar isodoublet written in terms of physical fields becomes

$$\phi(x) = \sqrt{\frac{1}{2}} \begin{pmatrix} 0 \\ v + h(x) \end{pmatrix}. \tag{1.5}$$

Of the four original scalar fields, only the field $h(x)$ remains, which is the Higgs field. The other three fields are the Goldstone bosons that are absorbed into the longitudinal polarizations of three gauge bosons that acquire mass through this mechanism. The Higgs mechanism results in two gauge bosons

$$W^{\pm} = \frac{W^1 \mp iW^2}{\sqrt{2}} \tag{1.6}$$

that have mass $M_W = vg/2$. There also exists a massive neutral Z boson and a massless photon

$$Z_\mu = \frac{gW^3_\mu - g'B_\mu}{\sqrt{g^2 + g'^2}} \text{ and } A_\mu = \frac{g'W^3_\mu - gB_\mu}{\sqrt{g^2 + g'^2}}, \tag{1.7}$$

where $M_Z = \frac{1}{2}v\sqrt{g^2 + g'^2}$ and $M_A = 0$. In addition, the Higgs mechanism allows fermions to acquire mass proportional to the vacuum expectation value v. The surviving remnant of the scalar isodoublet is the Higgs field $h(x)$ with a mass given by $m_H^2 = 2v^2\lambda$.

From the experimental determination of the Fermi coupling constant G_F [5] and the relation $1/2v^2 = G_F/\sqrt{2}$, the vacuum expectation v of ϕ^0 is determined to be $v = 246$ GeV, which sets the scale for electroweak symmetry breaking. The interaction terms of Standard Model particles with the Higgs boson depend on v but not λ, and are proportional to the masses acquired due to the Higgs mechanism. Therefore the strength of Higgs boson interactions with Standard Model particles is predicted. However, since the mass of the Higgs boson depends on the unknown parameter λ, there is no direct Standard Model prediction of the value m_H.

1.3 Properties of the Higgs Boson

Because the Higgs boson has not yet been observed, we do not know its mass. However, it is possible to restrict the range of the Higgs mass based on theoretical considerations and fits of various well-measured parameters to the predictions of the Standard Model. In addition, the Standard Model predicts the coupling parameters of the Higgs boson to other particles. This allows us to calculate the Higgs boson production cross section and its branching decay ratios.

1.3.1 The Mass of the Higgs Boson

Direct searches for the Standard Model Higgs boson have yielded negative results. The most stringent limit on the Higgs mass comes from a direct search at LEP II [6]. This search involved searching for $e^+e^- \to HZ$ production in a variety of final states: $HZ \to b\bar{b}q\bar{q}$, $HZ \to b\bar{b}\nu\bar{\nu}$, and $HZ \to b\bar{b}l^+l^-$, where l stands for a charged lepton (e, μ, or τ). The lower limit for the Higgs mass for this search is $m_H > 113.5$ GeV/c^2 at 95% C.L. Other searches at Tevatron Colliders have set upper limits on Higgs production cross sections in a variety of production channels [7].

In addition to the constraints on the Higgs mass from direct searches, precision electroweak measurements also constrain the range of m_H. The masses of the W and Z gauge bosons are sensitive to loop corrections involving the top quark and the Higgs boson, depending quadratically on m_t and logarithmically on m_H. Feynman diagrams illustrating these loop corrections can be seen in Figure 1.1. Thus precision measurements of the W mass [8, 9] and the top quark mass [10] give bounds on the possible values of m_H. Using the results from these measurements, constraints on the Higgs mass can be calculated. A fit to the latest electroweak measurements yields $m_H = 91^{+45}_{-32}$ GeV/c^2 or $m_H < 186$ GeV/c^2 at a 95% confidence level [11]. Figure 1.2 shows the 68% confidence regions of the W boson and top quark masses, in addition to the allowed range of m_W as a function

of m_t for various values of m_H.

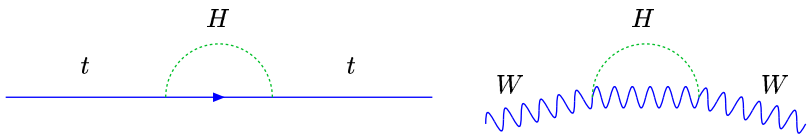

Figure 1.1: Feynman diagrams of Higgs boson loop corrections to the top quark and W boson propagators.

Theoretical constraints on the Higgs mass can also be inferred from the relationship between the energy scale Λ of physics beyond the Standard Model and the Higgs mass m_H. Knowing the lower limit of Λ from experimental tests of the Standard Model allow one to set upper and lower bounds on the Higgs mass [12].

The lower bound on the Higgs mass is obtained by requiring the electroweak minimum be the absolute minimum up to the scale Λ. If m_H is too small, then the Higgs potential obtains a global minimum at an energy lower than Λ, and new physics would be observed at an energy scale lower than that given by the Standard Model.

By requiring that the Higgs self-coupling λ be small enough for Higgs boson interactions to remain perturbative, an upper bound on λ can be set. Because the Higgs mass is related to λ by $m_H^2 = 2v^2\lambda$, this results in an upper limit on m_H. This limit, however, is only a mathematical requirement, since there does not exist a physical requirement for the Higgs self-coupling to remain perturbative. In the case where the Higgs coupling λ is not perturbative, the predictivity of the Standard Model Higgs sector can no longer be achieved through perturbative quantum field calculations.

Based on these theoretical constraints, the maximum and minimum Higgs mass can be computed as a function of the energy scale Λ at which the Standard Model is no longer valid. This is illustrated in Figure 1.3.

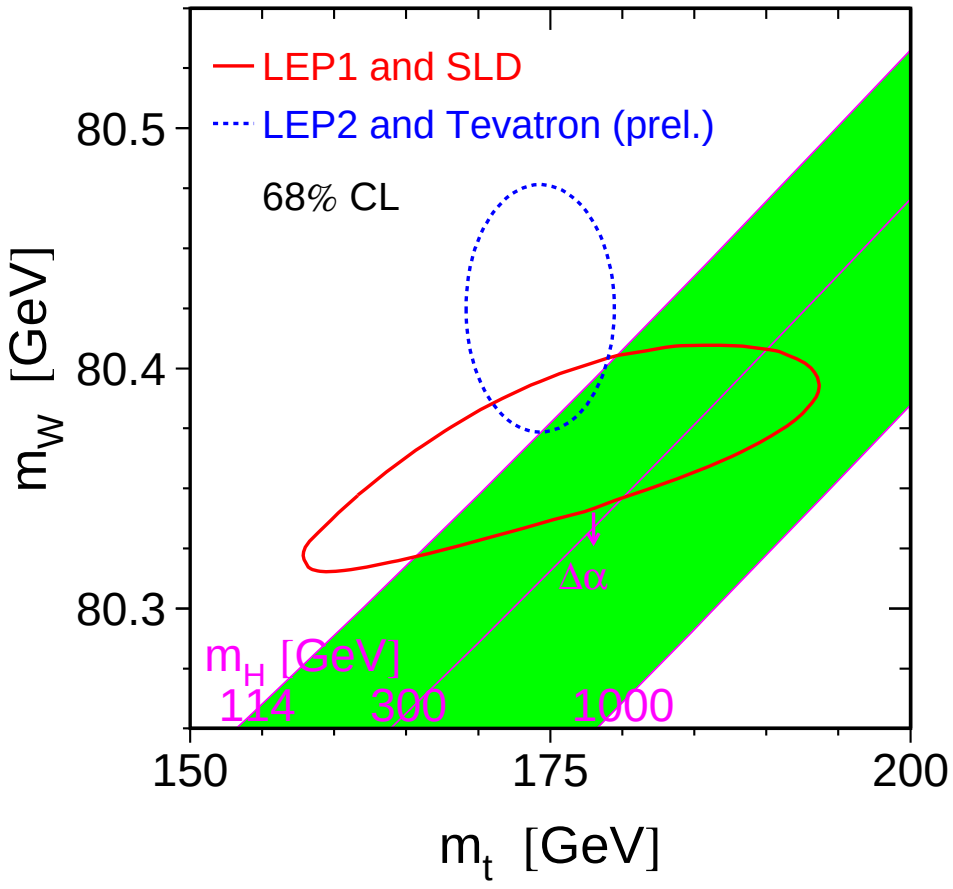

Figure 1.2: Contours of 68% confidence level in the $m_t - m_W$ plane and the constraint on the Higgs boson mass as a function of m_t and m_W. The solid red curve shows the constraints (68% C.L.) coming from studies at the Z boson pole at the LEP and SLD e^+e^- colliders. The dashed blue curve shows constraints (68% C.L.) from precision measurements of m_W and m_t using data from the LEP and Fermilab Tevatron experiments. The arrow labelled $\Delta\alpha$ shows the change in the constraints of the e^+e^- colliders if the value of $\alpha_{EM}(m_Z^2))$ is shifted by one standard deviation.

1.3.2 Higgs Boson Decays and Branching Ratios

Because the Higgs couplings to other Standard Model particles are known, the decay rates of the Higgs boson to Standard Model particles are determined for a given value

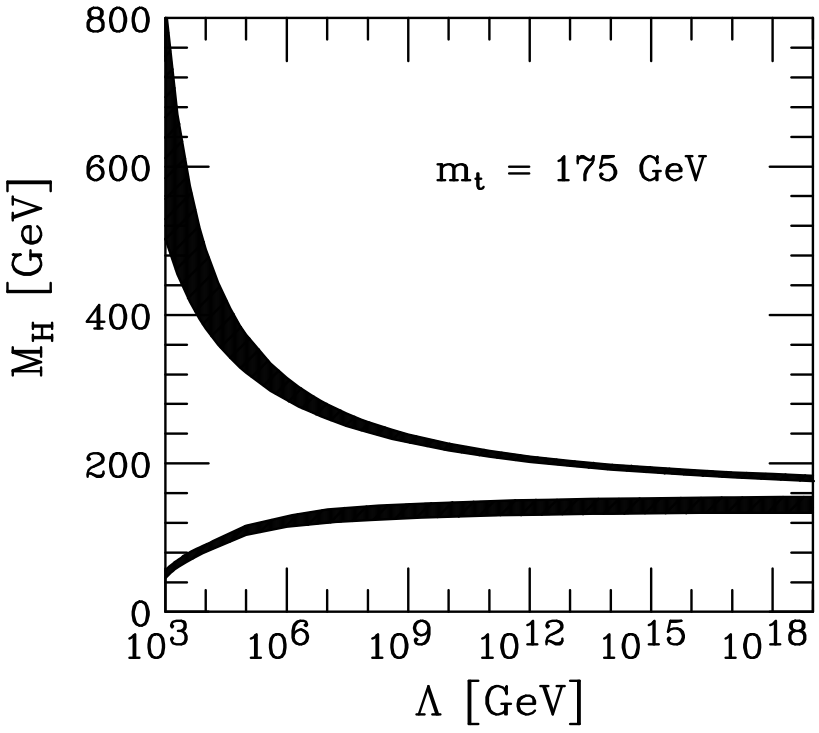

Figure 1.3: The upper and lower Higgs mass bounds as a function of the energy scale Λ at which the Standard Model is no longer valid. The shaded areas represent theoretical uncertainties in the calculation of the Higgs mass bounds.

of the Higgs mass [13]. These branching ratios are shown in Figure 1.4 for a range of Higgs masses from 80 to 200 GeV/c^2. These branching ratios include QCD corrections at next-to-leading order. The tree level branching ratios are proportional to masses of the decay daughters, but a Higgs boson decay to massless particles is also possible through loops of heavy quarks.

For a Higgs boson with $m_H \lesssim 135$ GeV/c^2, the decay mode $H \to b\bar{b}$ dominates, with a small contribution from $\tau^+\tau^-$ and gg decays. However at larger m_H the $b\bar{b}$ decay rate drops off rapidly, and the branching ratio of $H \to W^+W^-$ becomes dominant above $m_H \simeq 140$ GeV/c^2, peaking close to unity at $m_H \simeq 170$ GeV/c^2. At high masses, the decay $H \to ZZ$ is also relevant.

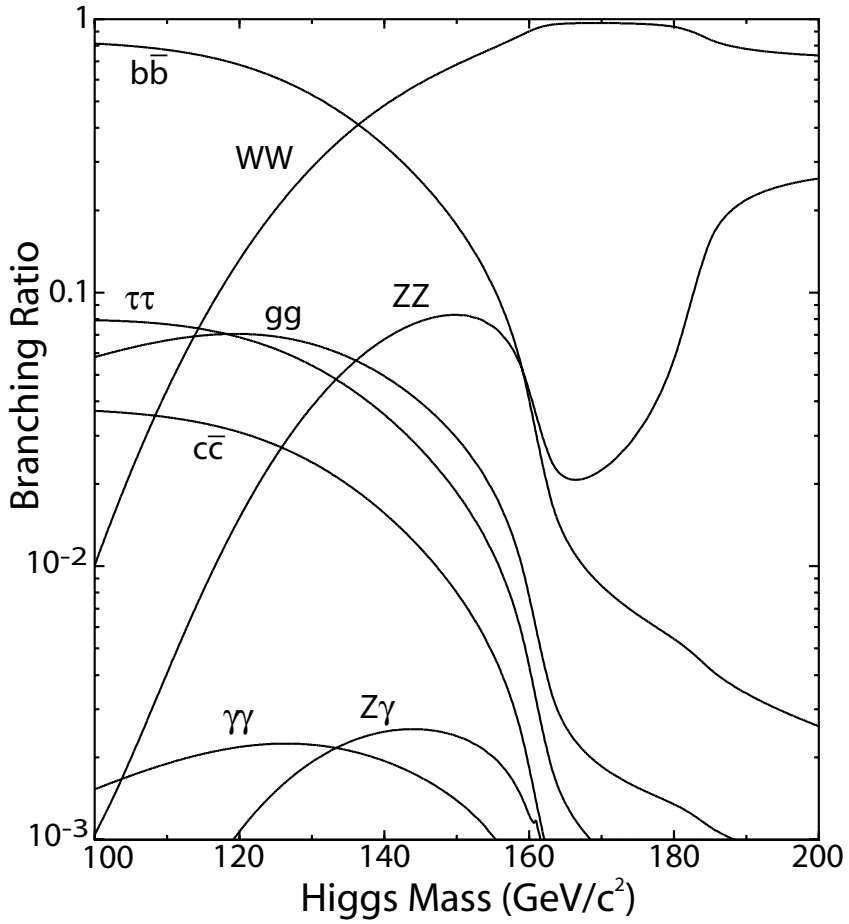

Figure 1.4: Branching ratios for decay modes of the Standard Model Higgs boson as a function of the Higgs boson mass.

1.3.3 Higgs Boson Production Cross Sections at the Tevatron

Because the Higgs boson couples to Standard Model fermions and bosons, it can be produced through numerous processes. The cross sections for Higgs boson production in $p\bar{p}$ collisions at 2.0 TeV have been calculated for various values of the Higgs mass [13], and are shown for different Higgs boson production mechanisms in Figure 1.5.

It can be seen that the dominant production mechanism of the Standard Model Higgs boson in $p\bar{p}$ collisions at $\sqrt{s} = 2.0$ TeV is through gluon fusion, which proceeds predominantly through a top quark triangle loop. For a Higgs boson with $m_H \lesssim 135$ GeV/c^2, the primary signature in this production channel would be through $gg \to H \to$

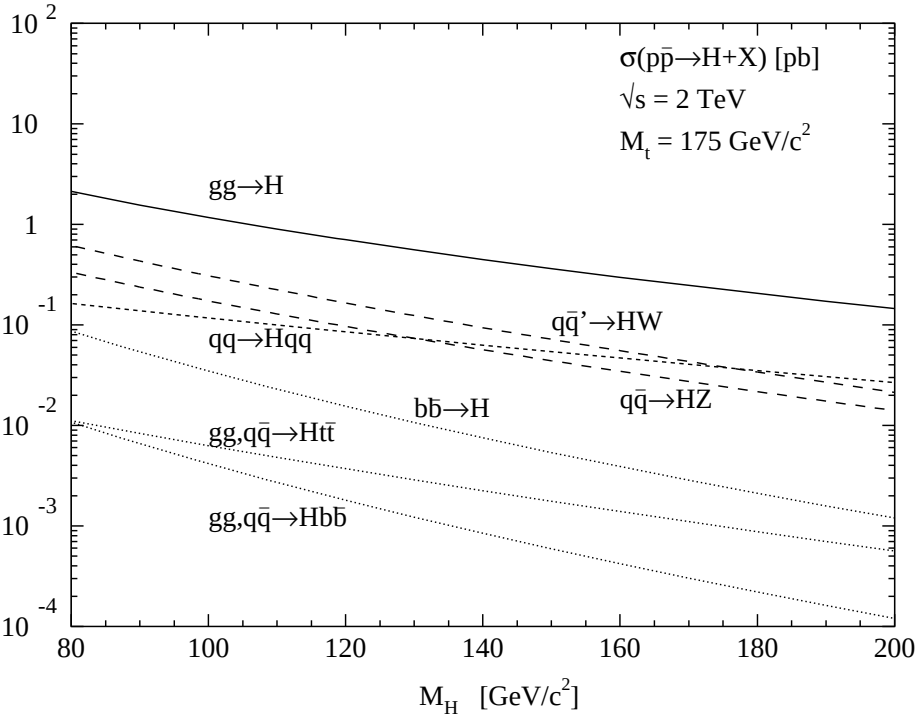

Figure 1.5: Higgs boson production cross sections at Tevatron energies of 2.0 TeV for various production mechanisms as a function of the Higgs boson mass.

$b\bar{b}$. However, due to the overwhelming multijet background to the $b\bar{b}$ final state at the Tevatron which is measured to be more than 10^6 times larger than the predicted Higgs boson yield, the observation of a Higgs boson in this channel is almost impossible, even for a large dataset. For a Higgs boson with $m_H \gtrsim 140$ GeV/c^2, the signature $gg \to H \to W^+W^-$ is the primary mode for Higgs boson discovery.

The cross sections for associated Higgs boson production with a W or Z boson are approximately an order of magnitude lower than those for gluon fusion. This process proceeds through quark-antiquark annihilation into a virtual vector boson that undergoes Higgs radiation ($q\bar{q}' \to V^* \to VH$). The cross section for $q\bar{q}' \to W^{*\pm} \to W^{\pm}H$ ranges from 0.3 pb to 0.02 pb in the Higgs mass range between 100 and 200 GeV/c^2. For associated Higgs production with a Z boson instead of a W boson, the cross section is roughly a factor of two lower over the same mass range. For a low mass Higgs boson of $m_H \lesssim 135$ GeV/c^2, these channels are potentially the most promising discovery

modes. However, extracting a signal in these channels is difficult due to the large $Vb\bar{b}$ background, and additional criteria that help distinguish Higgs boson production from the $Vb\bar{b}$ background are necessary to obtain a statistically significant signal. For high mass SM Higgs bosons with $m_H \gtrsim 135$ GeV/c^2, this channel proceeds primarily through $q\bar{q} \to V^*H \to VW^+W^-$, which can give a distinctive like-sign dilepton signature with manageable background levels.

1.4 The $t\bar{t}H$ Production Channel

The production channel that is the focus of this thesis is the associated production of the Higgs boson with a top-antitop quark pair ($p\bar{p} \to t\bar{t}H$) where the Higgs boson decays to $b\bar{b}$. The cross section for $t\bar{t}H$ production is of the order 0.01 pb, which means that a search requires large datasets, efficient detection, and high background rejection [14]. This search also complements searches for the Higgs boson in the other channels such as WH [15] and ZH production. Another motivation for searching in this channel is to rule out anomalously large $t\bar{t}H$ production cross sections that greatly exceed the Standard Model estimate.

The cross sections for $p\bar{p} \to t\bar{t}H$ at $E_{CM} = 1.96$ TeV have been computed at next-to-leading order [16]. Selected leading order Feynman diagrams for the process $p\bar{p} \to t\bar{t}H$ are shown in Figure 1.6.

From Figure 1.4, we see that such a search will be sensitive to Higgs masses up to 135 GeV/c^2. Due to the top quark exclusively decaying by $t \to W^+\bar{b}$ [17], this search looks for experimental signatures consistent with the process $p\bar{p} \to t\bar{t}H \to W^+W^-b\bar{b}b\bar{b}$.

This search also focuses on the scenario where one of the W bosons decays leptonically to $e\nu_e$ or to $\mu\nu_\mu$. This leaves a final state experimental signature of a high p_T electron or muon, missing transverse energy ($\not\!\!E_T$) due to the undetected neutrino, four b-jets, and two jets from light quark hadronization and fragmentation.

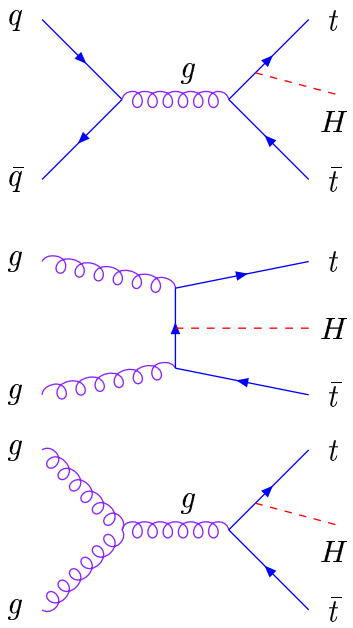

Figure 1.6: Leading order Feynman diagrams for $p\bar{p} \to t\bar{t}H$.

We use 319±19 pb^{-1} of data collected with the Collider Detector at Fermilab (CDF II) from proton-antiproton collisions at $E_{CM} = 1.96$ TeV produced by the Fermilab Tevatron for this search. The data is selected by requiring the presence of a electron or muon candidate. This search features improved and novel b-quark identification algorithms and robust background estimates. The event selection criteria, evaluation of background yields, and the search method are not influenced by the resultant signal yield. In this way, the measurement is "blinded" from events in the signal region that might otherwise bias our determination of the event selection [18].

The remainder of the thesis proceeds as follows: Chapter 2 describes the experimental apparatus employed to perform this search, including the CDF detector and the Fermilab Tevatron accelerator; Chapter 3 details the event selection criteria; the event detection efficiency for $t\bar{t}H$ events is described in Chapter 4; the method and evaluation of the background estimates is discussed in Chapter 5; kinematic distributions of the events that pass the selection criteria and the results of the search are discussed in Chapter 6; the conclusions drawn from this analysis are given in Chapter 7.

Chapter 2

Experimental Apparatus

This search for $t\bar{t}H$ involves the measurement of particle properties that have experimental signatures resembling $t\bar{t}H$ production as a result of proton-antiproton collisions at 1.96 TeV. These collisions are produced by the Tevatron accelerator located at the Fermi National Accelerator Laboratory (Fermilab) in Illinois, USA. The particles that result from these collisions are detected by the Collider Detector at Fermilab (CDF II), a multi-purpose detector placed at one of the collision points of the Tevatron ring.

2.1 The Accelerator

The Tevatron accelerates protons and antiprotons and collides them at a centre-of-mass energy of 1.96 TeV. The process of creating proton and antiproton beams and accelerating them to the required energy is performed by the proton source, the Main Injector, the antiproton source, and the Tevatron. A diagram of the accelerator chain is shown in Figure 2.1.

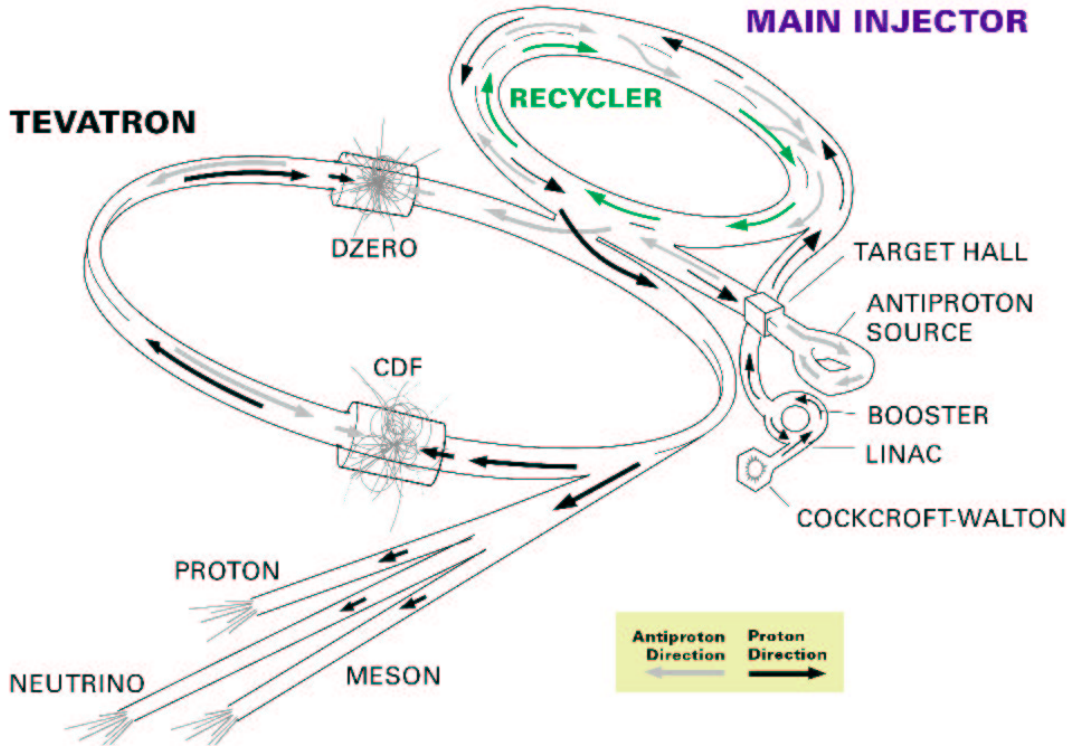

Figure 2.1: The Fermilab accelerator chain.

2.1.1 The Proton Source

A Cockcroft-Walton electrostatic accelerator ionizes hydrogen gas by adding an extra electron to the hydrogen atoms to make charged ions. It then accelerates these ions to an energy of 750 keV. These ions enter a 130 m linear accelerator (Linac) where they are accelerated to energies of 400 MeV by radio-frequency cavities. At the tail end of the Linac, there are carbon foils placed to remove the two valence electrons from the hydrogen ions. The resultant protons are then accelerated by a synchotron accelerator (booster) with a circumference of 475 m. The protons travel around the booster ring until they reach an energy of 8 GeV before being transferred to the Main Injector.

2.1.2 The Main Injector

The Main Injector is a synchotron accelerator with a 3 km circumference. It takes the 8 GeV protons from the booster, and accelerates a fraction of them to 150 GeV and injects them into the Tevatron. The remaining protons are accelerated to 120 GeV and sent to the Target Station. The Main Injector also accepts 8 GeV antiprotons from the antiproton source and accelerates them to 150 GeV before injecting them into the Tevatron.

2.1.3 The Antiproton Source

The protons of energy 120 GeV from the Main Injector are smashed onto a nickel target in the Target Station. The antiprotons are separated from the other resultant particles by a pulsed magnet and are focused into a beam. This beam of antiprotons is sent to a synchotron called the Debuncher, used to reduce the spread in energy of the antiprotons. The antiproton beam continues to the Accumulator, which is a storage ring used to accumulate antiprotons at a rate of 7×10^{10} per hour. While in the Accumulator, the antiprotons also experience stochastic cooling [19] to reduce the beam emittance. Once the emittance and intensity of the antiproton beam meet minimal quality requirements, the antiprotons are then sent to the Tevatron for further acceleration.

2.1.4 The Tevatron

The Tevatron is a synchotron accelerator and has a circumference of 6.3 km. Protons and antiprotons are injected into the Tevatron at 150 GeV and accelerated to an energy of 980 GeV. To accelerate the protons and antiprotons, the Tevatron uses 774 superconducting dipole magnets, each with a magnetic field of 4.2 T. The beams traverse the circumference of the ring in 36 distinct bunches of protons and antiprotons.

The CDF detector sits at one of the dedicated collision points on the Tevatron accel-

erator ring. At this collision point, the Tevatron uses special-purpose focusing magnets to reduce the proton and antiproton beam sizes to less than 30 μm.

The collision rate at the CDF detector is given by $R = \mathcal{L}\sigma_{int}$, where σ_{int} is the interaction cross section for proton-antiproton collisions at 1.96 TeV, and $\mathcal{L}$ is the luminosity of the colliding beams. The luminosity is defined by

$$\mathcal{L} \equiv f \times \frac{n_p n_{\bar{p}}}{4\pi\sigma_x\sigma_y}. \tag{2.1}$$

Here, f is the bunch collision frequency, $n_p, n_{\bar{p}}$ are the numbers of protons and antiprotons in each bunch, and σ_x, σ_y are the widths of the Gaussian beam profiles in the horizontal and vertical directions.

Because the luminosity decreases exponentially with time, with an approximate half-life of 5 hours, the proton and antiproton beams are extracted from the Tevatron ring after about 20 hours. The period of time between beam injection and extraction is called a store. After the beams are extracted, the process of accelerating proton and antiproton beams to 980 GeV begins again with a new store.

2.2 The CDF Detector

The data from proton-antiproton collisions at a centre-of-mass energy of 1.96 TeV are collected and analyzed with the upgraded CDF detector [20]. CDF is a general purpose, forward-backward and azimuthally symmetric solenoidal detector. It uses charged particle tracking, electromagnetic and hadronic calorimetry, and fine grained muon detection to measure particle properties. A pictoral representation of CDF is shown in Figure 2.2.

The CDF detector surrounds the accelerator beamline. Tracking systems are placed closest to the interaction region to measure trajectories of charged particles in a uniform, solenoidal magnetic field pointed in the proton beam direction of 1.4 T. This magnetic field is produced by a 4.8 m long solenoid placed outside the tracking system at a radius of 1.5 m from the beamline. Calorimeters are placed outside the tracking volume to

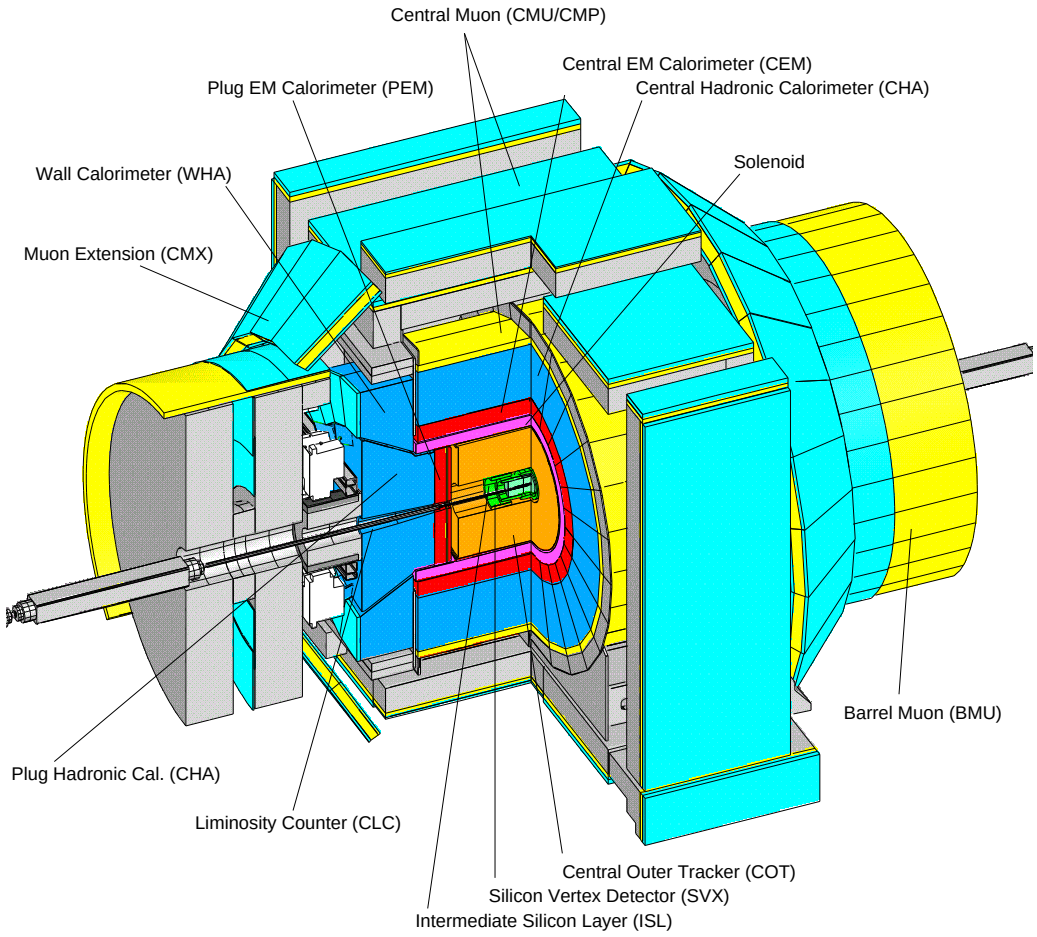

Figure 2.2: A pictoral representation of the Collider Detector at Fermilab.

provide energy measurements of electrons, photons, and jets. The calorimeter modules are arranged in a projective tower geometry. The outermost part of the detector is the muon detection system, consisting of drift chambers.

The CDF coordinate system is defined with the positive z-axis pointing in the proton direction, the x-axis pointing outwards from the Tevatron ring, and the y-axis pointing away from the centre of the Earth. Cylindrical coordinates r, θ, and ϕ are more commonly used, where r is the distance away from the centre of the interaction region, ϕ is the azimuthal angle and θ is the polar angle of the coordinate system. The pseudorapidity $\eta = -\frac{1}{2}\ln(\tan\theta)$ is often used instead of θ to describe the polar angle.

2.2.1 The Tracking System

The CDF subsystem closest to the interation point is the tracking system. The tracking system consists of Layer 00 (L00), the Silicon Vertex Tracker (SVX), the Intermediate Silicon Layers (ISL), and the Central Outer Tracker (COT). A schematic view of the CDF tracking system is shown in Figure 2.3. The entire tracking system is immersed in a 1.4 T magnetic field, produced by a superconducting solenoid. The magnetic field, parallel to the proton beam, causes charged particle trajectories to curve, allowing the tracking system to measure the trajectory and momentum of charged particles.

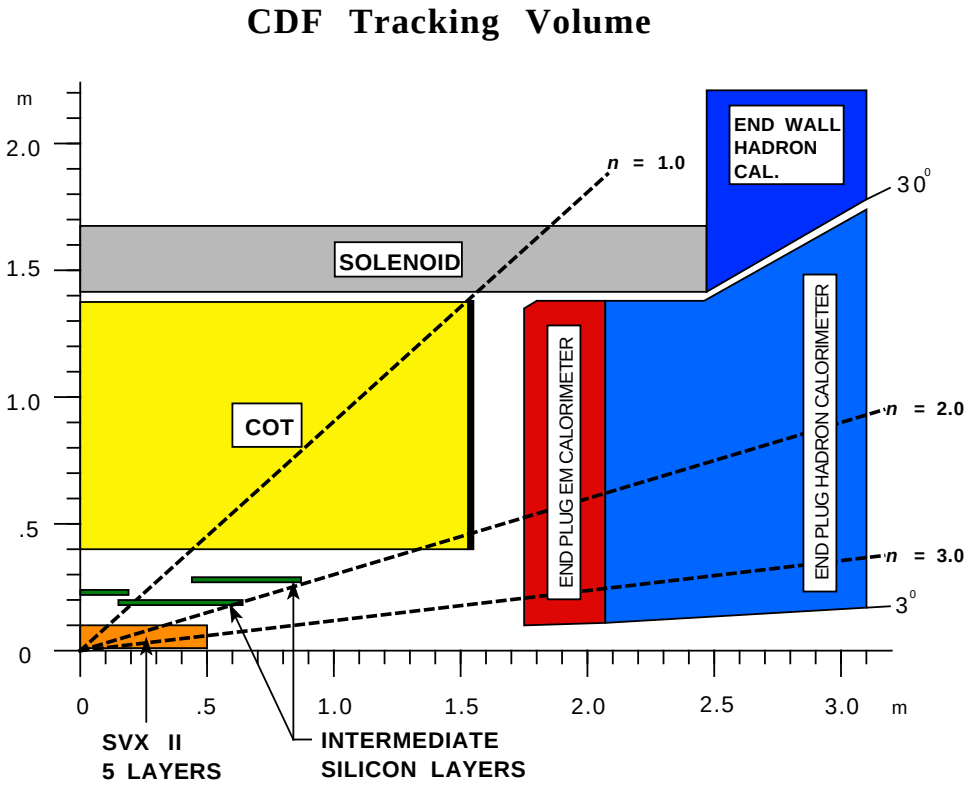

Figure 2.3: A schematic view of one quadrant of the CDF tracking system.

The Central Outer Tracker

The Central Outer Tracker (COT) is the outermost component of the CDF tracking system. It is a cylindrical drift chamber that provides tracking coverage in the region

$|\eta| \lesssim 1$. It is 310 cm long and encloses the volume between an inner radius of 44 cm to an outer radius of 132 cm. Within this volume, the COT consists of 96 concentric layers divided into 8 distinct groups called superlayers.

The COT chamber is filled with 50% argon and 50% ethane gas. Longitudinal sense wires acting as anodes and field planes acting as cathodes are strung between two end-plates to produce an electric field. Charged particles passing through the gas in the COT chamber create electron-ion pairs. The electric field allows the free electrons to drift toward the sense wires. The electron movement also creates further ionization of molecules, causing an electron avalanche onto the sense wire that creates an electrical pulse. The COT electronics measure the time-of-arrival of the pulse relative to the collision.

With a drift speed of 50 μm/ns in the argon-ethane gas mixture, the particle position in each layer can be determined using the measured drift time. The magnetic field causes the charged particle trajectory to curve, leaving a helical track in the COT.

Four of the COT superlayers have wires that are strung parallel to the beam axis to provide particle track reconstruction in the transverse $r - \phi$ plane. Alternating with these are four superlayers with wires strung at small stereo angles of $\pm 2^\circ$ to the beamline to allow for track reconstruction in the z-direction.

The COT single hit resolution is 180 μm. The transverse momentum of each track is calculated by measuring its helical trajectory inside the 1.4 T magnetic field provided by the solenoid: $p_T = Bqr$, where B is the magnitude of the magnetic field in Tesla, q is the charge of the particle (in units of elementary charge e) and r is the radius of curvature of the track in m and p_T is in GeV/c. The momentum resolution of tracks reconstructed in the COT is $\sigma_{p_T}/p_T^2 \approx 1.7 \times 10^{-3}$ (GeV/c)$^{-1}$.

The Silicon Tracker

The silicon tracking system consists of Layer 00 (L00), closest to the interaction region, followed by the Silicon Vertex Tracker (SVX). The Intermediate Silicon Layers (ISL) populate the region between the SVX and the COT. The end view of the silicon detectors is shown in Figure 2.4.

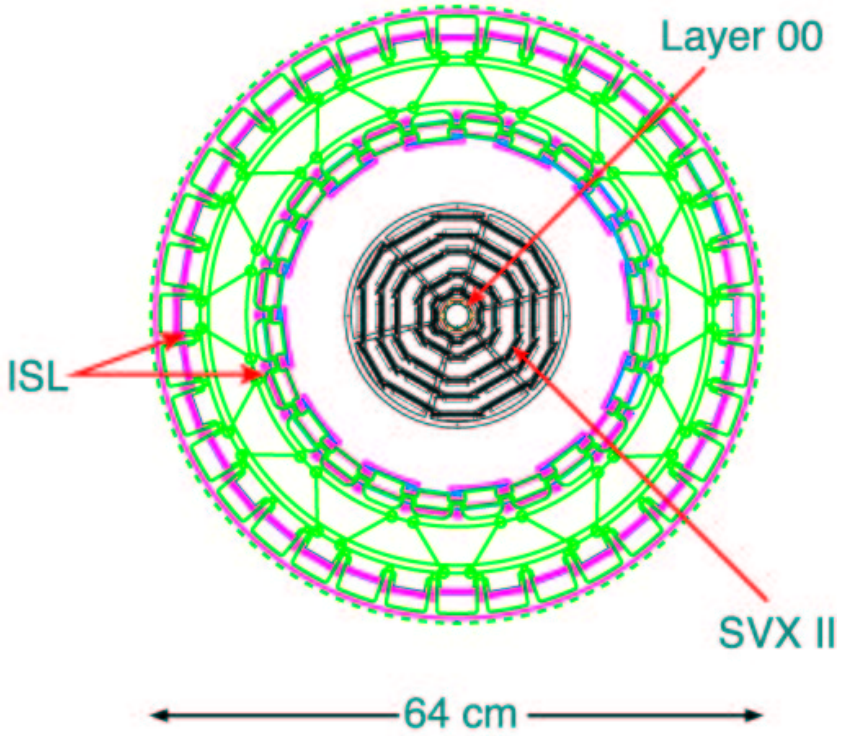

Figure 2.4: End view of the CDF silicon tracking system.

L00 is single-sided layer of silicon microstrip arrays with a readout pitch of 50 μm that provides position measurements in the $r - \phi$ plane. This layer is mounted directly onto the Tevatron beampipe at radius r=1.6 cm.

The SVX is made of 5 concentric layers of silicon detectors with each layer arranged in 12 distinct wedges of silicon strips divided into azimuthal units. The SVX is 96 cm long and the layers range from radii of 2.4 cm to 10.7 cm. Each wedge is made of double-sided silicon detectors. One side of the strip provides an axial hit position measurement. Three of the five layers also have strips positioned at a stereo angle of 90° on the second

side, providing position measurements in the z direction. The stereo strips on the remaining two layers are arranged at a small stereo angle of 1.2°, allowing them to provide information in both the z and ϕ directions. The strip pitch is 55-65 μm for axial strips, 60-75 μm for 1.2° stereo strips and 125-145 μm for 90° stereo strips. The SVX detector's instrinsic resolution for an axial measurement point is approximately 12 μm.

The ISL consist of three double-sided silicon layers that are located at radii from 20 cm to 29 cm. One side of the silicon detectors contains axial strips with a strip pitch of 55 μm while the other side contains stereo strips at an angle of 1.2° with a strip pitch of 73 μm. The ISL measure the axial position of tracks with a resolution of approximately 16 μm providing one additional measurement point in the central region ($|\eta| < 1$) between the SVX and the COT, as well as two additional measurement points in the forward region ($1 < |\eta| < 2$). This is illustrated in Figure 2.5.

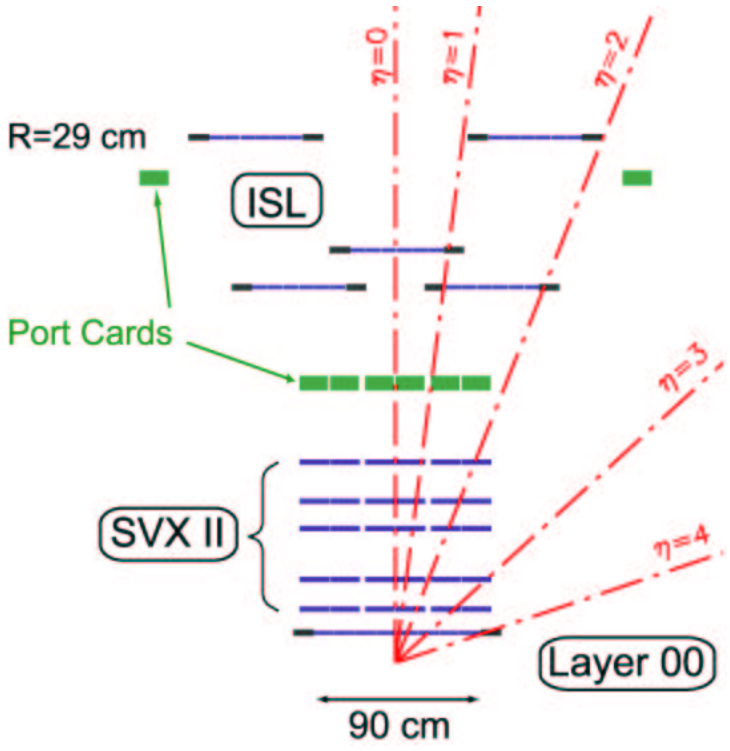

Figure 2.5: Side view of one half of the CDF silicon tracking system.

2.2.2 The Calorimeter

The CDF calorimeter is located outside the tracking system and the solenoid. It is a sampling scintillator calorimeter that measures the energy of particles that enter its volume. The calorimeter consists of alternating layers of active, scintillating material with absorbing material such as lead and steel.

The calorimeter is divided into electromagnetic and hadronic calorimeter subsystems. The electromagnetic calorimeter is closer to the interaction region, and consists of the Central Electromagnetic Calorimeter (CEM) with pseudorapidity coverage of $|\eta| < 1.1$ and the Plug Electromagnetic Calorimeter (PEM) with coverage between $1.1 < |\eta| < 3.6$. The hadronic component of the calorimeter surrounds the electromagnetic component, and consists of the Central Hadronic Calorimeter (CHA), the Plug Hadronic Calorimeter (PHA), and the Wall Hadronic Calorimeter (WHA). The physical placement of these subsystems can be seen in Figure 2.2.

The Electromagnetic Calorimeter

The electromagnetic calorimeter has 23 alternating layers. The absorbing layer of 4.5 mm is made of lead that alternates with 4 mm of active scintillator. The calorimeter is divided into wedges forming a projective tower geometry pointing towards the interaction point. Figure 2.6 shows the geometry of a single wedge in the calorimeter.

Electrons passing through the electromagnetic calorimeter radiate photons as they cross the absorbing material. These photons create electron-positron pairs as a result of their interaction with lead. The electrons and positrons continue to radiate, creating a chain of particles called a shower. The shower is detected by the scintillator and converted to a light pulse with an amplitude proportional to the energy of the particles. Light guides collect the photons and pass them to photo-multiplier tubes (PMTs).

The resolution of the electromagnetic calorimeter is expressed by $\sigma_E/E = 0.135/\sqrt{E_T}$ for the central component and $\sigma_E/E = 0.144/sqrtE \oplus 0.7\%$ for the plug component (E

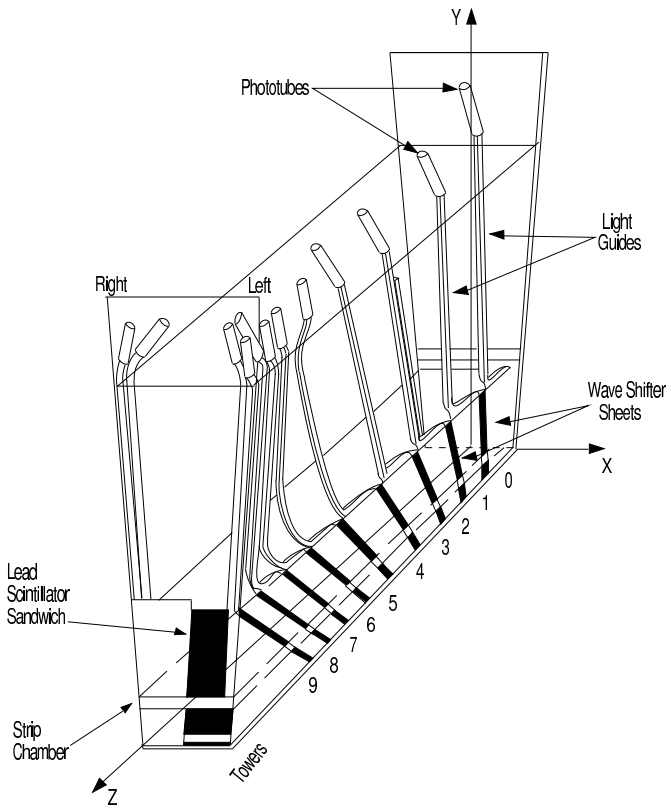

Figure 2.6: Diagram of a CEM wedge.

measured in GeV).

A multi-wire proportional chamber (CES) in the central region and a scintillator strip detector (PES) in the plug region are placed at a depth in the calorimeter where electromagnetic showers are maximally developed. The CES and PES measure the $\phi - \eta$ position of the shower with a precision of approximately 2 mm.

The Hadronic Calorimeter

The hadronic calorimeter consists of 23 alternating layers. It uses 5 cm layers of iron as the absorbing material that alternate with 6 mm layers of active scintillator. Like the electromagnetic calorimeter, the hadronic calorimeter is also divided into wedges that form towers pointing to the interaction point.

Charged particles passing through the hadronic calorimeter collide with iron nuclei,

creating secondary hadrons. These also interact with other nuclei, creating a shower of hadrons. Electromagnetic processes also contribute to the shower. The shower is detected by the scintillator layers, and the generated light pulse is passed to PMTs, as in the electromagnetic calorimeter.

The energy resolution of the hadronic calorimeter is given by $\sigma_E/E = 0.75/\sqrt{E}$ for the central component and $\sigma_E/E = 0.74/\sqrt{E} \oplus 3.8\%$ for the plug component (E measured in GeV).

2.2.3 The Muon Detection System

Muons are minimally ionizing particles, and thus deposit only a small fraction of their energy in the calorimeters. Hence, the muon detection system is placed outside the calorimeter modules. The CDF muon detection system is divided into four independent subsystems of proportional wire chambers and scintillators. The Central Muon detector (CMU) and the Central Muon Upgrade (CMP) give muon detection coverage of $|\eta| < 0.6$. The Central Muon Extension (CMX) detects muons with $0.6 < |\eta| < 1.0$. The Barrel Muon Detector (BMU) covers the pseudorapidity range $1.0 < |\eta| < 1.5$ but this system is not used in this search.

The CMU system consists of four layers of drift chambers as shown in Figure 2.7. The chambers are filled with a mixture of argon and ethane gases. Muons passing through the muon chambers ionize the gas in the drift chambers. The hit position in the drift cells are determined from the drift time of the ions to the wire.

The CMP system also consists of four layers of wire drift chambers. The design is identical to the CMU, except that the layers are staggered by a half cell per layer. The chambers are located behind 60 cm of steel and form a rectangular box around the detector. The CMP is used together with the CMU detector in the central region, and the combined subsystem is referred to as the CMUP muon detector. The CMX system consists of eight layers of wire drift chambers placed in a conical pattern. A layer of

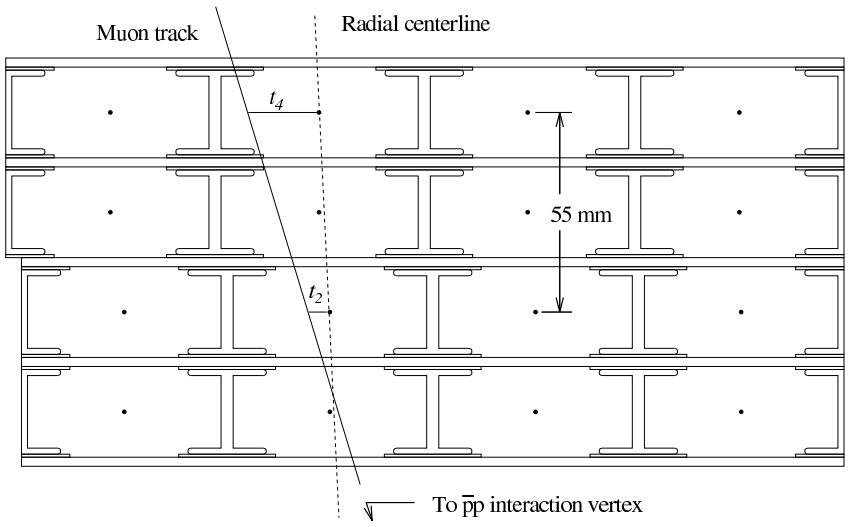

Figure 2.7: Four layers of drift chambers in the CMU.

scintillator plates is placed on the outermost edge of the CMP and CMX to provide additional timing information.

2.2.4 The Cherenkov Luminosity Counter

The Cherenkov Luminosity Counters (CLC) measure the luminosity of the $p\bar{p}$ interactions [21]. The CLC is made of modules of Cherenkov counters located at each end of the CDF detector, covering the region $3.6 < |\eta| < 4.6$. The modules carry PMTs that detect the Cherenkov ultraviolet light emitted by the charged particles passing through the modules. A large amount of light detected by the CLC points to the presence of particles generated from an inelastic $p\bar{p}$ collision. The instantaneous luminosity of the proton and anti-proton beams can be inferred from the rate of inelastic collisions detected by the CLC.

The instantaneous luminosity $\mathcal{L}$ is given by:

$$\mathcal{L} = \frac{R_{p\bar{p}}}{\epsilon_{CLC} \times \sigma_{inelastic}}, \tag{2.2}$$

where $R_{p\bar{p}}$ is the measured rate of inelastic $p\bar{p}$ collisions, ϵ_{CLC} is the CLC detector acceptance and $\sigma_{inelastic}$ is the total inelastic cross section.

2.2.5 The Trigger and Data Acquisition System

The Tevatron collides proton and antiproton bunches at a rate of 2.5 MHz. Since the information from all detector channels per event is 250 kilobytes, this rate is too high for each collision to be recorded. Because a small fraction of the inelastic $p\bar{p}$ collisions produce events of interest, a trigger system is used by CDF to identify selected events of interest to be recorded. CDF uses a three level trigger structure. The level 1 trigger is able to cope with data at the rate of 2.5 MHz, filtering out events such that subsequent levels can deal with a lower rate of data flow. Consequently, the level 1 trigger uses less sophisticated methods to select events, with subsequent levels increasing in sophistication. A schematic of the data flow through the three distinct trigger levels are shown in Figure 2.8.

The level 1 trigger uses custom-built hardware to select events based on preliminary information from calorimeters, COT, and the muon detectors. The data for each bunch crossing is stored in a pipeline for 6 μs, the time in which the level 1 trigger must make a decision whether to accept or reject the event. At this stage, jets and electron candidates are reconstructed from the electromagnetic and the total energy deposited in a trigger tower that exceed a minimum threshold. The missing transverse energy ($\not\!\!E_T$) [1] and the total sum of energy in the event is also computed. Muon candidates are inferred from hits in the muon detector that are consistent in arrival time. Charged particle tracks are also formed by the Extremely Fast Tracker (XFT), which reconstructs particle trajectories in the axial layers of the COT. This information is used by the level 1 trigger to make a decision. The maximum output rate of the level 1 trigger is 20 kHz.

The level 2 trigger combines both custom hardware and modified commercial processors. This level of the trigger consists of the Secondary Vertex Trigger (SVT) and the cluster finder hardware. The SVT uses silicon hit information to trigger on tracks

[1] Missing transverse energy for the trigger is defined by $\not\!\!E_T = -\sum_{e,jets} E_T$ where the transverse energy is given by $E_T = E \times \sin\theta$. A more detailed definition will be provided in chapter 3.

displaced from the primary vertex. The cluster finder forms clusters of energy from neighboring calorimeter towers to form more reliable electron and jet candidates. The data from these systems as well as the data used for the Level 1 decision are sent to the level 2 trigger processor crate, where a decision is made whether to accept or reject the event. If accepted, the event data is read from the buffer and sent to the Level 3 trigger. The maximum level 2 trigger output rate is 300 Hz.

The level 3 trigger is a farm of 300 dual processors connected by high-bandwidth networks to digital readout and storage devices. These processors run a simplified version of the offline CDF reconstruction algorithm. The processing time is about one second per event. Events are accepted by the level 3 trigger at a maximum rate of about 75 Hz. The data for accepted events are sent to permanent storage for subsequent processing by the full event reconstruction algorithms.

These reconstruction algorithms process the data to build software data structures to represent physics objects such as electron, muon, or jet candidates. Further details on the selection of these candidates is discussed in the next chapter. The data used in this analysis was collected during the period August 2002 to August 2004, and filtered to ensure that all major subsystems of the CDF detector were functioning reliably during the recording of the event data.

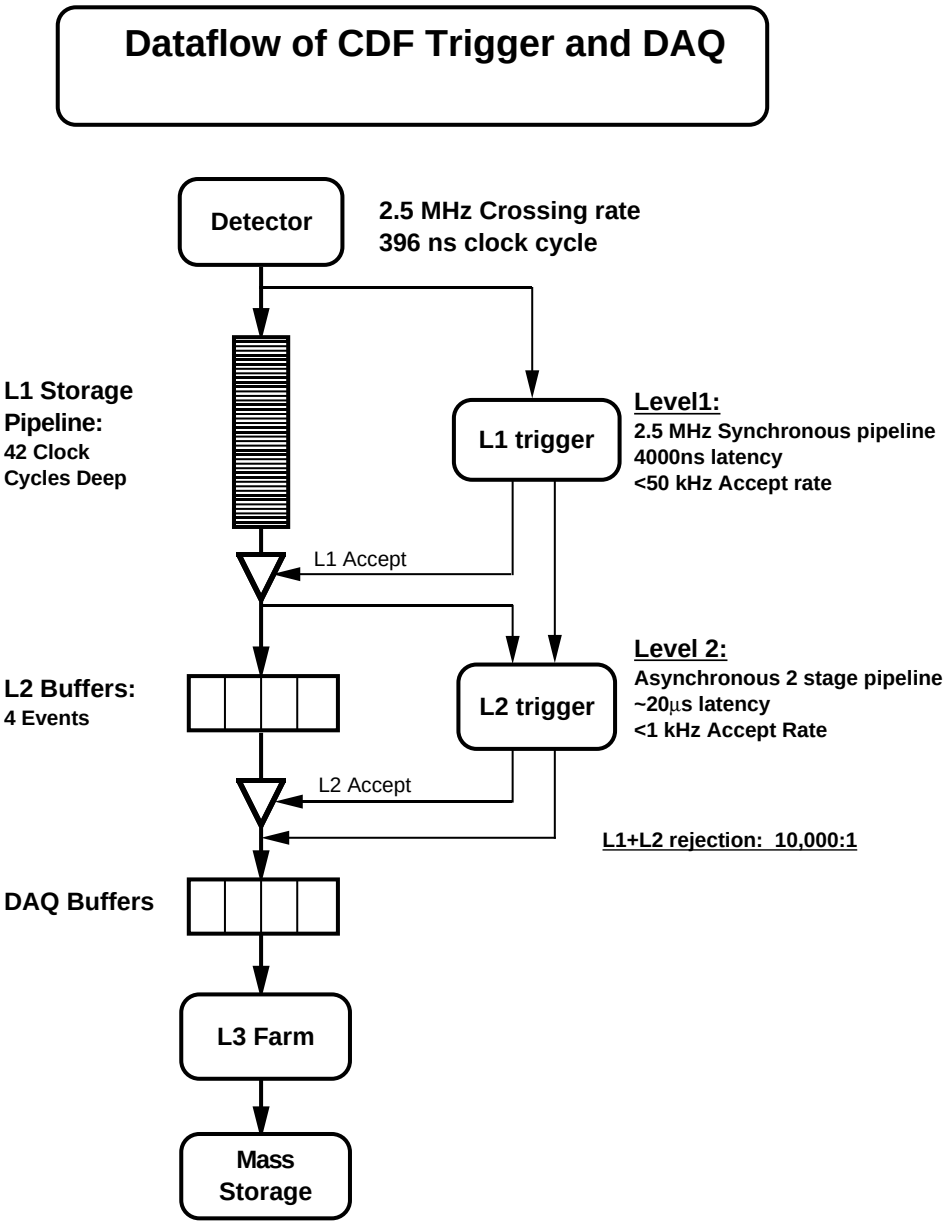

Figure 2.8: Schematic representation of the data flow in the CDF trigger and data acquisition systems.

Chapter 3

Event Selection

3.1 Selection Strategy

We search for evidence of $t\bar{t}H$ production in 319 pb^{-1} of $p\bar{p}$ collisions at a centre-of-mass energy of 1.96 TeV. The selection strategy for this search will be to implement a set of criteria that will distinguish the $t\bar{t}H$ signal from other Standard Model background. However, due to the low cross section of this process, we cannot afford to be overly stringent with such criteria, so we devote considerable effort to maximizing the efficiency of our search.

We focus on a search for a Higgs boson decaying via the process $H \to b\bar{b}$. The search for $t\bar{t}H$ thus consists of identifying events of the form $W^+W^-b\bar{b}b\bar{b}$. Therefore, the final state experimental signature includes four b-jets and the decay products of the W bosons. We also focus our search on events where one of the W bosons decays to two jets and the other W boson decays leptonically to a charged lepton and a neutral lepton.

Our event selection requires that there be at least 5 jets detected with transverse energy $E_T > 15$ GeV and $|\eta| < 2.0$. Figure 3.1 shows the fraction of $t\bar{t}H$ events that populate each jet bin based on Monte Carlo calculations ($m_H = 115$ GeV). Requiring four jets or more only increases the signal efficiency by 25%, while increasing the $t\bar{t}$

background by a factor of four from Monte Carlo studies.

We also demand evidence for a leptonic W decay, involving $W^- \to e^- \bar{\nu}_e$ or $W^- \to \mu^- \bar{\nu}_\mu$. We also include the possibility of the decay $W^- \to \tau^- \bar{\nu}_\tau \to e^- \bar{\nu}_e \nu_\tau \bar{\nu}_\tau$ or $W^- \to \tau^- \bar{\nu}_\tau \to \mu^- \bar{\nu}_\mu \nu_\tau \bar{\nu}_\tau$ [1]. This requirement significantly reduces background from QCD multi-jet events. We therefore apply selection criteria that indicate the presence of a charged high p_T lepton (electron or muon) and missing transverse energy[2] $\not\!\!E_T$. This would signal the presence of at least one leptonic W boson decay.

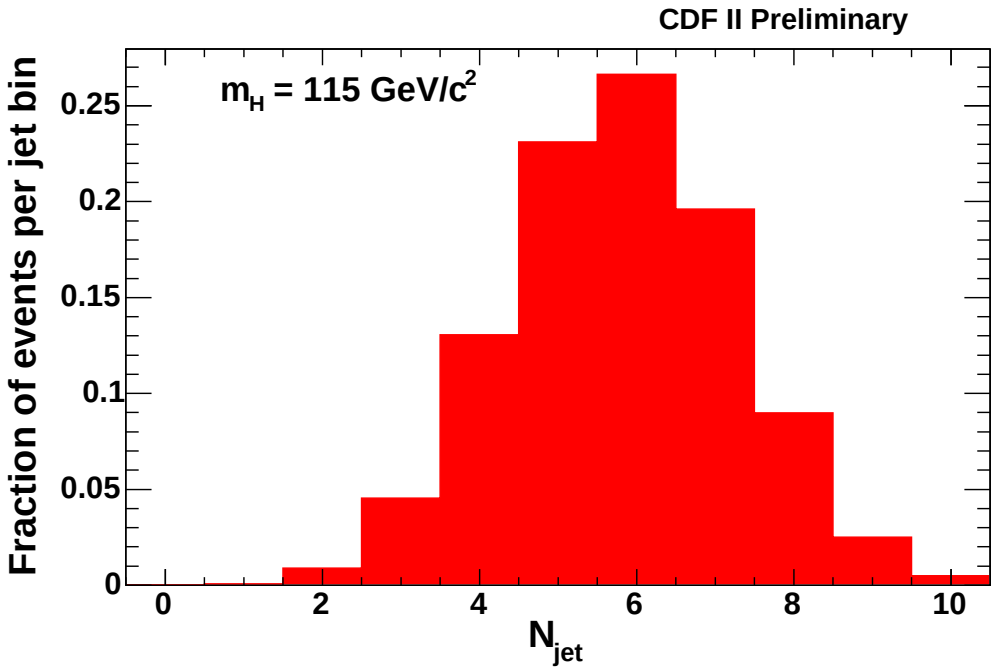

Figure 3.1: Jet Multiplicity distribution for $t\bar{t}H$ events in Monte Carlo simulation for $m_H = 115$ GeV for jets with $E_T > 15$ GeV and $|\eta| < 2.0$.

The distinctive feature of the final state signature of $t\bar{t}H$ events with the decay $H \to b\bar{b}$ is that there are four b quarks produced, each of which results in a jet of particles in which a B hadron is embedded. Because B hadrons have a relatively long lifetime, jets

[1] These decays and their equivalent charge conjugate decays are considered

[2] Here we correct the missing transverse energy for the presence of muons so that $\not\!\!E_T = -\sum_{e,\mu,jets} E_T$. A more robust definition is given in Section 3.3.3.

that originate from b quarks usually include secondary vertices that are displaced from the primary vertex. Candidate jets that include evidence of a secondary vertex are b-tagged jets. This search will require at least three b-tagged jets in candidate $t\bar{t}H$ events. Requiring at least four jets that are b-tagged reduces the signal by more than a factor of five, which is too large a reduction in the signal event yield given that the production cross section is quite small.

3.2 Trigger Requirements

There are two distinct data samples used for this analysis. One of the data samples was collected by requiring that the event satisfy the central electron trigger, which records events that have electron candidates in the CEM. The other sample was obtained by requiring that the event pass the central muon trigger, which records events that have muon candidates in the CMU/CMP or in the CMX.

3.2.1 The Central Electron Trigger

The central electron trigger records events with electron candidates in the CEM using a three level process. At level 1, energies from calorimeter towers that are divided into $0.2 \times 15^\circ$ units in $\eta - \phi$ space are summed with at least one trigger tower satisfying $E_T > 8$ GeV and the ratio of hadronic to electromagnetic energy satisfying the condition $E_{had}/E_{em} < 0.125$. Level 1 of the trigger also requires the existence of at least one COT track with $p_T > 8$ GeV/c. At level 2, a calorimeter cluster is formed by adding adjacent towers with $E_T > 7.5$ GeV to the seed tower found in level 1. The sum of energy in this cluster is required to exceed 16 GeV. At level 3, an electromagnetic cluster with $E_T > 18$ GeV and $E_{had}/E_{em} < 0.125$ must be found by the reconstruction algorithm with a COT track of $p_T > 9$ GeV/c pointing to this cluster. The efficiency of the trigger for $W \to e\nu$ candidates is $96.6 \pm 0.2\%$ [22].

3.2.2 The Central Muon Trigger

The central muon trigger also uses a three level process to identify muon candidates in the CMU/CMP and the CMX. At level 1, the trigger requires hits in at least 3 layers of the CMU or the CMX. In the case where the hits are found in the CMU, level 1 also requires that CMP hits in at least 3 of 4 layers are found, consistent in ϕ with the observed CMU hits. For the case where the hits are found in the CMX, a matching hit pattern in the CSX scintillator counters must also be found. These matched hit patterns are typically referred to as stubs. Additionally, a COT track with $p_T > 4$ GeV/c must be associated with the stub. At level 2, the track requirement is increased to $p_T > 8$ GeV/c, and the trigger also requires that the track is matched to the hits in the muon detector systems. At level 3, a fully reconstructed COT track with $p_T > 18$ GeV/c must be matched with stubs in the CMU/CMP chambers or the CMX. The efficiency of the combined CMU/CMP and CMX triggers for $W \to \mu\nu$ candidates is $92.5 \pm 1.1\%$ [22].

3.3 W Boson Selection

To detect the presence of W candidates that decay leptonically, events must pass the lepton trigger described in the previous section. We impose more stringent criteria on the electron or muon candidates in the full event reconstruction. We also require that there is missing transverse energy in the event, which indicates that a neutrino was produced that passed through the detector without interacting.

3.3.1 Electron Identification

Electron candidates are identified by the presence of a cluster of electromagnetic calorimeter towers with energy deposition, and a track identified by the COT pointing in the direction of the cluster. The algorithm for constructing a calorimeter tower starts with a seed tower containing a minimum transverse energy of $E_T > 3$ GeV. Adjacent towers

to the seed tower are added to the cluster up to a maximum of three towers in η. Only calorimeter showers in the CEM are considered.

The following additional variables are used to select electron candidates: The total transverse energy in the calorimeter cluster $E_T^{cluster}$, the transverse momentum p_T of the COT track pointing to the cluster, the ratio of cluster energy for the hadronic to electromagnetic calorimeters E_{had}/E_{em}, the number of axial and stereo hits associated with the COT track pointing to the calorimeter cluster, and the isolation of the electron candidate. The isolation is defined by

$$I \equiv \frac{E_T^{cone} - E_T^{cluster}}{E_T^{cluster}}, \tag{3.1}$$

where E_T^{cone} is the total transverse energy in the towers within a cone radius of $\Delta R = \sqrt{\Delta\eta^2 + \Delta\phi^2} = 0.4$ of the calorimeter cluster.

The selection criteria for electron candidates are summarized in Table 3.1. In addition, electron-positron pairs coming from the process $\gamma \to e^+e^-$ are reconstructed and rejected.

Electron Candidate	
$E_T^{cluster}$	$\geq$ 20 GeV
P_T	$\geq$ 10 GeV/c
E_T if $P_T \leq$ 50 GeV/c	$\leq$ 100
E_{had}/E_{em}	$\leq$ 0.055+0.00045*E/GeV
# axial SL	$\geq$ 3
# stereo SL	$\geq$ 2
Isolation	$\leq$ 0.1

Table 3.1: Offline selection criteria for electrons.

The effect of this set of criteria on electrons has been studied on electron candidates in $Z \to e^+e^-$ candidate events [22], which provide a clean sample of high p_T electrons with very little contamination from hadronic jets. The distributions of a subset of these selection variables for the $Z \to e^+e^-$ candidates are shown in Figure 3.2.

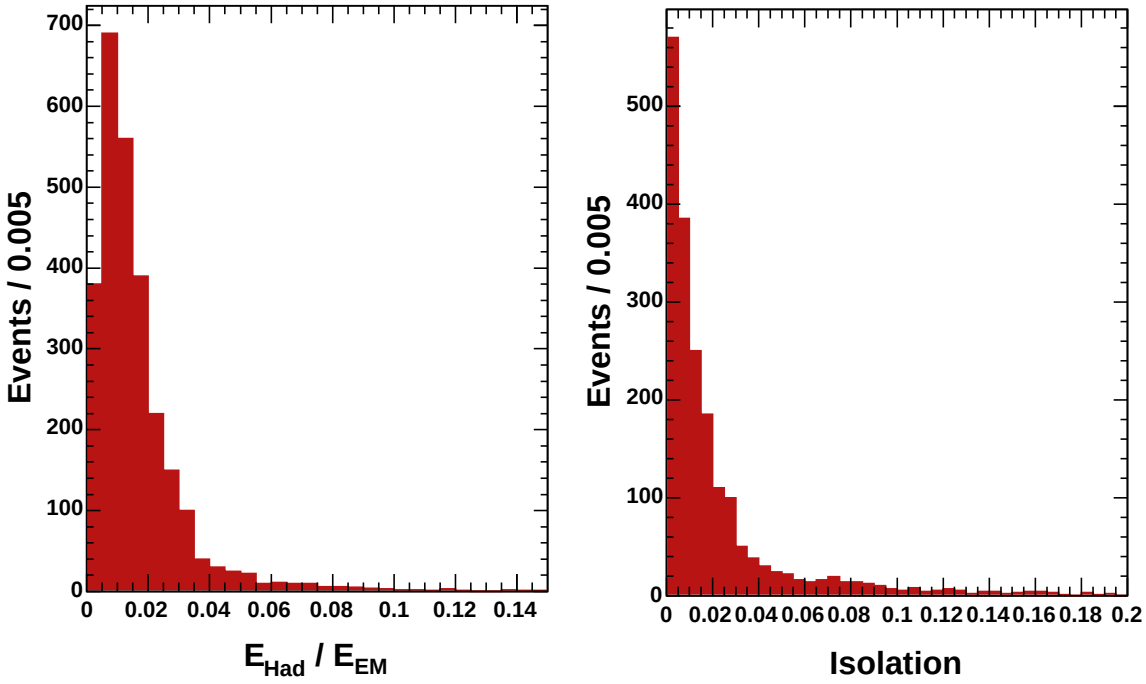

Figure 3.2: Distributions of electron selection variables E_{had}/E_{em} and isolation from $Z \to e^+e^-$ candidate events.

3.3.2 Muon Identification

The selection criteria for muons require a track segment (stub) found in the muon chambers (CMUP or CMX), and an associated COT track pointing in the same direction as the stub.

The following quantities are used to identify muon candidates: The transverse momentum of the COT track pointing to the muon stub, P_T, the energy deposited in the hadronic and electromagnetic calorimeters within a cone radius of $\Delta R = 0.4$ of the muon trajectory, E_{had} and E_{em}, the distance between the extrapolated track and the muon stub in the $r - \phi$ plane, $|\Delta x|$, the number of axial and stereo hits associated with the COT track pointing to the muon stub, and the muon isolation. The isolation, I, is defined by

$$I \equiv \frac{E_T^{cone} - P_T}{P_T}, \tag{3.2}$$

where E_T^{cone} is the total transverse energy in towers within a cone radius $\Delta R = 0.4$ of the muon trajectory.

CMUP Muon Candidate	
P_T	$\geq$ 20 GeV/c
E_{had}	$\leq$ 6.0+ max(0, 0.0280 $*$ (p $-$ 100.0)) GeV
E_{em}	$\leq$ 2.0+ max(0, 0.0115 $*$ (p $-$ 100.0)) GeV
$\lvert\Delta x_{CMU}\rvert$	$\leq$ 3.0 cm
$\lvert\Delta x_{CMP}\rvert$	$\leq$ 5.0 cm
# axial SL	$\geq$ 3
# stereo SL	$\geq$ 2
Isolation	$\leq$ 0.1

Table 3.2: Offline selection criteria for muon candidates in the CMUP.

The offline selection criteria for muons are summarized in Table 3.2. The distributions of a subset of these muon selection variables are shown in Figure 3.3 for $Z \rightarrow \mu^+\mu^-$ candidate events. The hit distribution for axial and stereo segments for COT tracks are shown for both muons and electrons in $Z \rightarrow l^+l^-$ candidate events in Figure 3.4, where l stands for an electron or a muon [22].

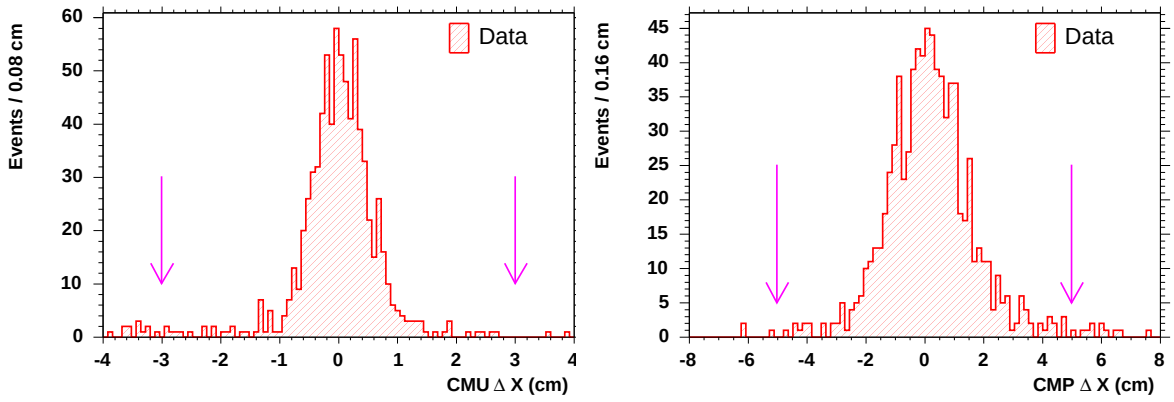

Figure 3.3: Distributions of muon selection variables $|\Delta x|_{CMU}$ and $|\Delta x|_{CMP}$ from $Z \rightarrow \mu^+\mu^-$ candidate events. The arrows indicate the selection cut applied on these variables.

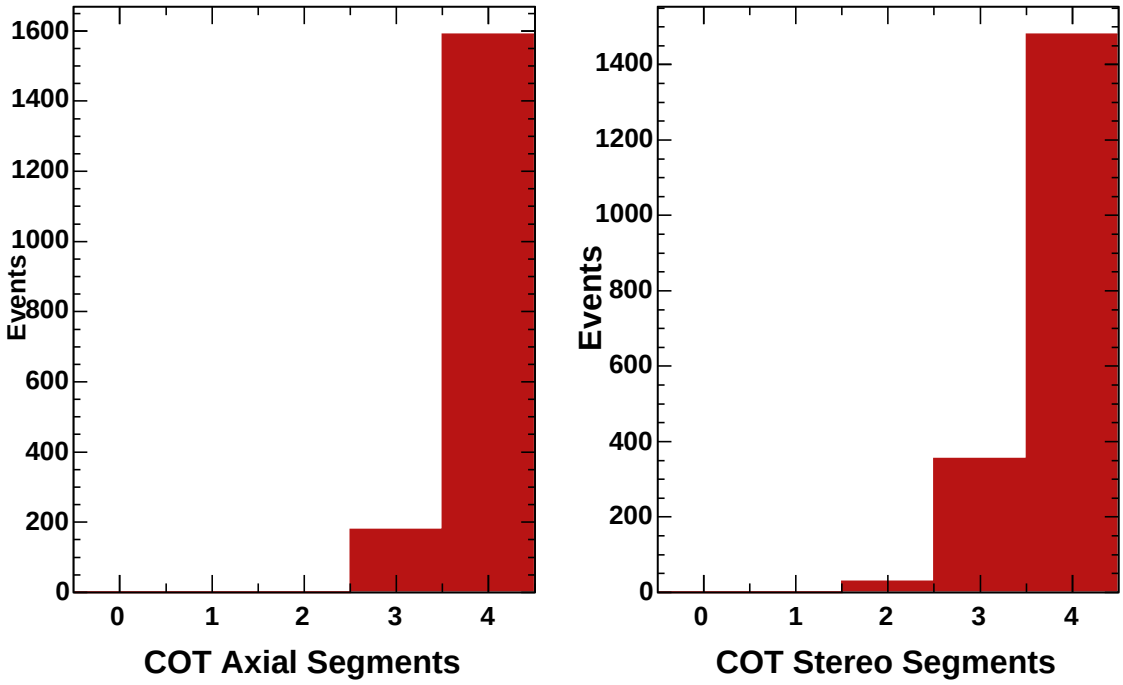

Figure 3.4: Hit distribution for axial and stereo layers in COT tracks in $Z \rightarrow l^+l^-$ events.

3.3.3 Missing Transverse Energy Requirements

Because the initial $p\bar{p}$ collision has no momentum in the transverse direction, the final state particles should have a net transverse momentum equal to zero, due to momentum conservation. However, neutrinos from W boson decay pass through the detector without interacting, thus leaving a missing transverse energy signature. Thus, the presence of a neutrino can be inferred from an imbalance in the transverse energy measured, called the missing transverse energy $\not\!\!E_T$.

The missing transverse energy[3] is defined as the negative vector sum of the transverse energy measured over all calorimeter towers:

$$\not\!\!E_T = -\sum_i E_i sin\theta_i \hat{n}_i \tag{3.3}$$

[3]Though the quantity $\not\!\!E_T$ is a vector quantity, our selection criteria is only concerned with the magnitude of the missing transverse energy.

where E_i is the energy deposited in the ith calorimeter tower, θ_i is the polar angle of the ith tower, and $\hat{n}_i$ is the unit vector in the azimuthal plane pointing from the interaction point to the ith tower.

For events with a muon candidate, it is necessary to account for the muon momentum in the evaluation of $\not\!\!E_T$, since muons only leave a modest amount of energy in the calorimeter. The $\not\!\!E_T$ calculation is corrected for the presence of the muon by equating the transverse momentum of the muon with its transverse energy (neglecting the small mass of the muon). This inferred transverse energy of the muon provides extra terms for the summation in equation 3.3. We require that $\not\!\!E_T > 10$ GeV in our event selection, which is a relatively loose requirement compared to other selection strategies that look for evidence of a leptonic W decay.

3.4 Jet Selection

The identification of hadronic jets uses a cone-clustering algorithm [23] that sums the energy of calorimeter towers contained inside a cone radius $\Delta R = \sqrt{\Delta\eta^2 + \Delta\phi^2} = 0.4$. However, this preliminary calculation underestimates the actual energy of the original jet. Thus, the jet energy calculation is corrected using a multi-step process.

3.4.1 Jet Energy Corrections

The corrections to the jet energies are performed in successive levels. Each of these levels incorporates the energy corrections of the previous levels. The first level correction ensures that the calorimeter response is uniform over the entire azimuthal and polar coverage of the calorimeter. Next, a correction is applied to account for aging effects that alter the gain in the calorimeter PMTs. Then, the jet energies are scaled to the calibrations performed in Ref. [24]. Finally, a correction is applied to account for additional energy attributed to the jet that does not originate from the original parton energy, but

from multiple $p\bar{p}$ interactions during the same bunch crossing.

The event selection for this analysis requires at least 5 jets with a corrected $E_T > 15$ GeV and with pseudorapidity $|\eta| < 2.0$.

3.4.2 b-jet Identification

The distinctive feature of $t\bar{t}H$ events where the Higgs decays via $H \to b\bar{b}$ is the existence of four b quarks in the final state. These b quarks hadronize and form B mesons that subsequently decay. Because the B mesons have a relatively long lifetime of $\tau \sim 10^{-12}$ s and have an average p_T of 60 GeV/c, the hadrons that originate from b quarks can travel a distance of a few millimetres before decaying [4]. The charged particles that come from the B meson decay do not originate from the original interaction vertex, but from the secondary vertex at the location of the B meson decay. A pictorial diagram showing tracks from secondary vertex decay is shown in Figure 3.5.

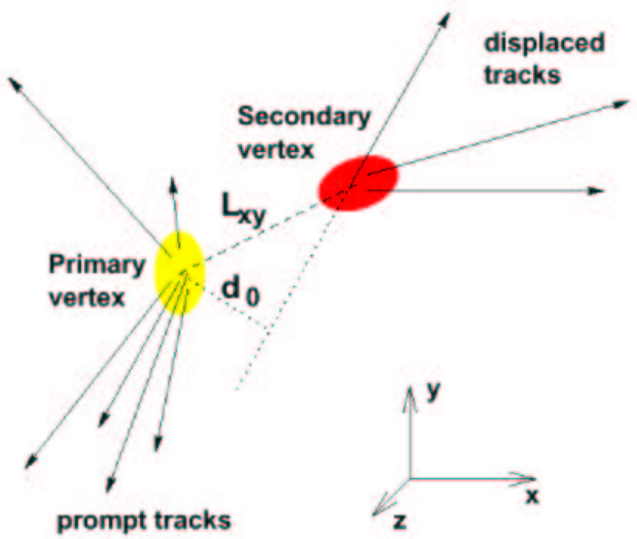

Figure 3.5: A diagram of tracks originating from a secondary decay vertex.

Therefore, the reconstruction of these tracks originating from B meson decay can be

[4] Mesons with c quarks also can decay a distance of a few hundred microns away, but the typical decay distance is shorter than B mesons.

used to infer the existence of a b quark, called b-tagging. In this analysis, two b-tagging algorithms are used: one is called SECVTX [25] and the other is called JETPROB [26]. We also combine the two algorithms into a super-algorithm, known as the Combined Tagger [27], that exploits information available from both taggers.

The SECVTX algorithm identifies b-jet candidates by fitting secondary vertices to tracks with large impact parameters. If such a secondary vertex is displaced far enough away from the primary vertex, then the jet is tagged as a b-jet candidate. SECVTX has "tight" and "loose" versions, the tight tagger having a higher purity of b-jets in the b-tagged sample, while the loose tagger has better efficiency of identifying b-jets. The efficiency of the SECVTX tagger is shown in Figure 3.6 as a function of the jet E_T and η.

JETPROB forms a joint probability that tracks associated with the jet originate from the primary vertex by using the impact parameter of each track. Based on this, a p-value that the jet itself originates from the primary interaction vertex is calculated. This quantity is called the jet probability, and jets with a jet probability below a certain threshold are tagged as b-jet candidates. The jet probability distribution for b-jets, c-jets, and light quark jets from Monte Carlo is shown in Figure 3.7.

The Combined Tagger combines the information from the SECVTX and JETPROB algorithms in a logical "OR". Using this information, the Combined Tagger is able to tag jets at higher efficiency than the SECVTX or JETPROB taggers alone. The Combined Tagger also has tight and loose configurations.

The SecVtx Algorithm

The SECVTX algorithm reconstructs secondary vertices from tracks that are significantly displaced from the primary interaction vertex. The algorithm first classifies tracks within a cone radius of 0.4 of the jet into two categories: Pass 1 tracks and Pass 2 tracks. The selection criteria are different for the tight and loose configurations of the SECVTX tagger.

These tracks must pass certain quality criteria. Thus the tracks are required to

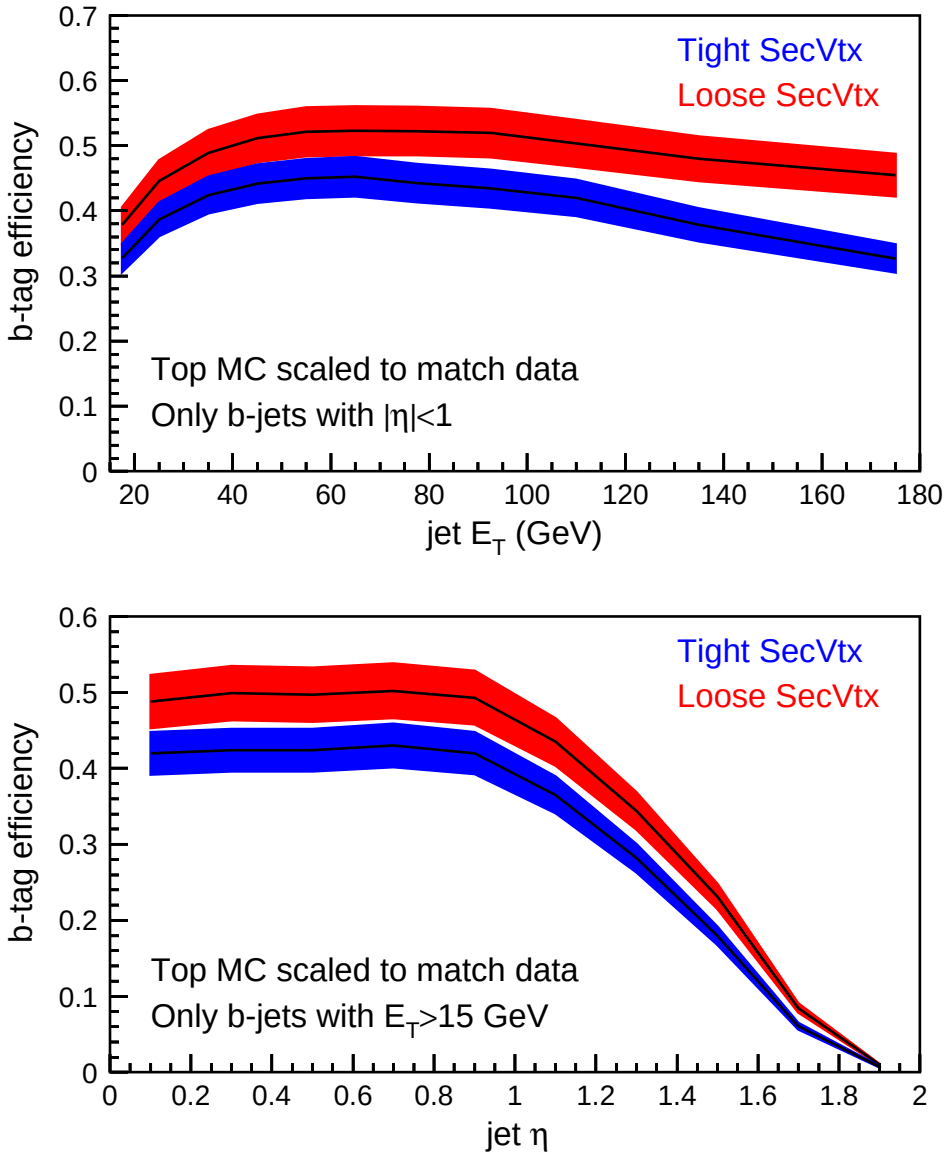

Figure 3.6: The tagging efficiency for the SECVTX tight and loose algorithm as a function of the jet E_T and η. These are based on Monte Carlo datasets, but corrected for discrepancies between the Monte Carlo and data.

exceed the minimum number of SVX $r-\phi$ layers; to have an acceptable track helix χ^2 normalized to the degrees of freedom, to exceed the minimum track p_T cut, and to have an impact parameter less than the maximum track impact parameter d_0; to not exceed the maximum track displacement in the z-direction $\delta(z_0)$; and to exceed the minimum

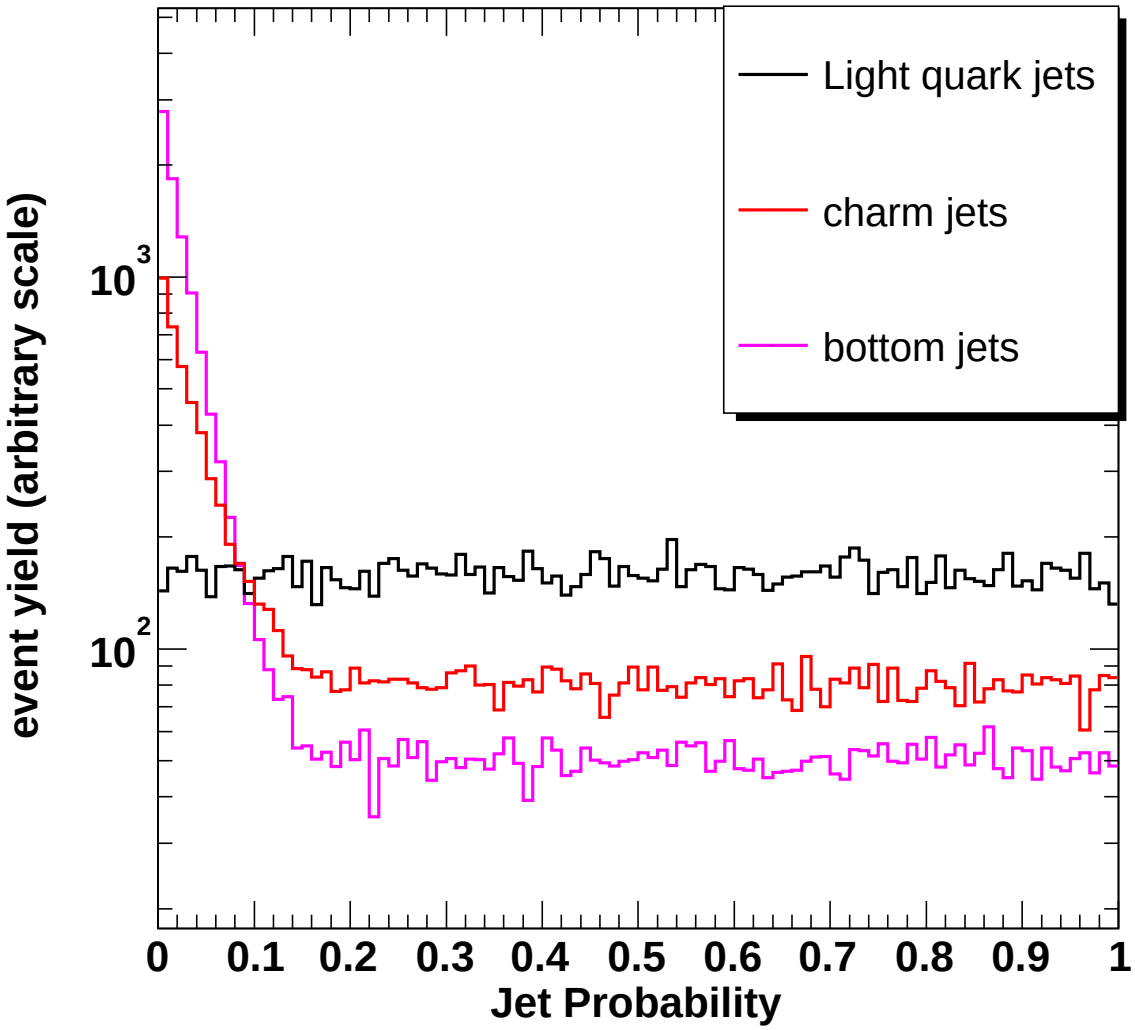

Figure 3.7: Jet probability distributions for b-jets, c-jets and light quark jets.

track d_0 significance $d_0/\sigma(d_0)$. This set of criteria ensures that Pass 1 and Pass 2 tracks are well measured by the SVX and are displaced from the primary vertex. The criteria are detailed in Table 3.3.

The SECVTX algorithm then attempts to make a vertex with Pass 1 tracks. There must be at least one track that satisfies $p_T > 1.0$ GeV/c. Pairs of tracks with invariant masses consistent with K^0 and Λ mass are removed. The algorithm then attempts to fit a vertex by using at least three tracks. The tight SECVTX algorithm prunes tracks that

SecVtx Track Quality Requirements				
SecVtx Configuration	**Tight**		**Loose**	
	Pass 1	Pass 2	Pass1	Pass2
No. of SVX $r-\phi$ layers $\geq$	3	3	2	3
Track normalized $\chi^2 <$	8.0	8.0	8.0	8.0
Track P_T (GeV/c) $>$	0.5	1.0	0.5	1.0
Track d_0 significance $>$	2.0	3.5	2.0	3.0
Track $\delta(z_0)$ (cm) $<$	2.0	2.0	2.0	2.0
Track d_0 (cm) $<$	0.15	0.15	0.15	0.15

Table 3.3: Criteria for SECVTX Pass 1 and Pass 2 tracks for tight and loose configurations.

cause the vertex χ^2 to increase by 45 or more, while the loose SECVTX algorithm prunes tracks that cause the vertex χ^2 to increase by 90 or more. The final vertex must have a χ^2 of less than 50 for the tight SECVTX tagger and less than 120 for the loose SECVTX tagger.

If the algorithm fails to find three Pass 1 tracks that make such a vertex, it then attempts to fit a vertex with Pass 2 tracks. One of these tracks must have $p_T > 1.5$ GeV/c and the invariant mass of the track pair must not be consistent with the mass of K^0 and Λ particles. The algorithm attempts to fit a vertex using at least two Pass 2 tracks, with the tight SECVTX algorithm pruning those that contribute an increase in vertex χ^2 of 90 and the loose SECVTX algorithm pruning those that contribute a 1000 unit increase in vertex χ^2. The final vertex must not exceed a χ^2 of 50 for the tight SECVTX tagger or 2000 for the loose SECVTX tagger.

The secondary vertex formed using displaced tracks is then compared to the primary interaction vertex. The displacement of the secondary vertex in the $r-\phi$ plane, L_{xy}, must satisfy $L_{xy}/\sigma(L_{xy}) > 7.5$ for the tight SECVTX tagger and > 9.0 for the loose

SECVTX tagger for the jet to be considered b-tagged. These additional criteria for the SECVTX algorithm are summarized in Table 3.4.

SecVtx Vertex Fit Requirements				
SecVtx Configuration	**Tight**		**Loose**	
	Pass 1	Pass 2	Pass1	Pass2
Highest p_T track (GeV/c) >	1.0	1.5	1.0	1.5
Track prune χ^2 <	45	30	90	1000
Vertex fit χ^2 <	50	50	120	2000
Vertex L_{xy} significance >	7.5	7.5	6.0	6.0

Table 3.4: Additional criteria for the tight and loose configurations of the SECVTX algorithm.

The JetProb Algorithm

The JETPROB algorithm forms a p-value that a jet originates from the primary interaction vertex using the impact parameters of tracks in a jet. The JETPROB algorithm classifies tracks into 72 different track categories, and models the impact parameter distributions of tracks in each category. The track categories are based on the number of SVX hits associated with the track, the track p_T, and the track pseudorapidity η_{trk}. These distributions $R(s; p_i)$ versus the impact parameter of the tracks, s, are modelled using two Gaussian distributions along with an exponential tail for each track category. The track categories are divided according to track properties p_i which are: the number of $r-\phi$ SVX layers hit, the transverse momentum of the tracks p_T^{trk}, and the track pseudorapidity η_{trk}.

Given the track impact parameter distributions, one can form a track probability for each track

$$P_{trk}(s; p_i) = \int_{-\infty}^{-|s|} R(t; p_i) dt, \tag{3.4}$$

where s is the impact parameter of the track in question, with properties p_i.

A jet probability can then be formed using the track probabilities of positively signed impact parameter jets. This jet probability is given by

$$P_{jet} = \Pi \sum_{k=0}^{N-1} \frac{(-\ln \Pi)^k}{k!}, \tag{3.5}$$

where $\Pi = P_1 P_2 ... P_N$ is the product of the individual track probabilities.

Jets with a low jet probability are considered b-tagged. A typical value for this jet probability cutoff is 0.01.

The Combined Tagger

The Combined Tagger uses both the SECVTX and JETPROB algorithms and combines them into a logical "OR". There are two configurations of the Combined Tagger: tight and loose.

The tight Combined Tagger considers a jet b-tagged if the tight SECVTX algorithm has tagged the b-jet. If tight SECVTX tagger has not tagged the jet, then the Combined Tagger looks at the the information provided by JetProb algorithm. If the jet has at least two tracks and a jet probability of less than 0.01, then the jet is also considered b-tagged. The loose Combined Tagger combines the SECVTX and JETPROB taggers in a similar way, except it uses the loose configuration of the SECVTX algorithm and a jet probability threshold of 0.02.

Studies of the performance have been performed on $t\bar{t}$ Monte Carlo events to evaluate the efficiency of these b-tagging algorithms. The misidentification rate of b-tagging light quark jets as b-jet candidates is also measured for the b-taggers in inclusive jet samples and by tagging the jets using negative impact parameter tracks. The comparison of the efficiency and mistag rates of these b-taggers is shown in Figure 3.8.

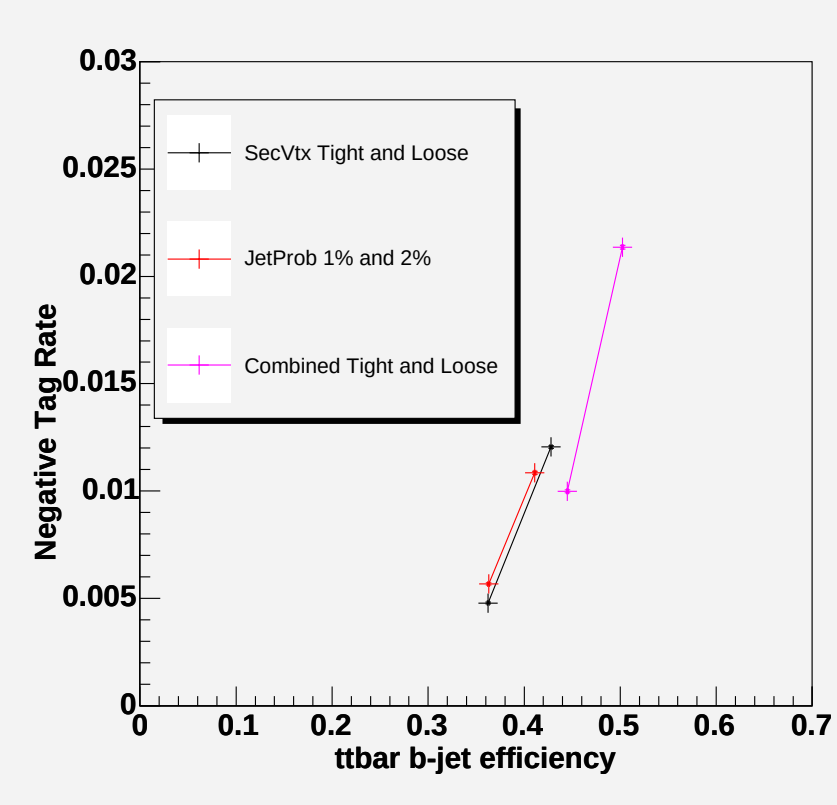

Figure 3.8: Comparison of efficiency and mistag rates for the different b-tagging algorithms. The black points show the efficiency and mistag rates for the SecVtx tagger, the red points for the JetProb tagger, and the purple points for the Combined Tagger.

3.5 Other Selection Criteria

In addition to finding evidence for W boson candidates and the jet requirements mentioned previously, there are further criteria applied to the data sample to further reduce backgrounds.

Z bosons that decay leptonically can mimic a W boson when one of the leptons is not reconstructed and jet mismeasurements allow the event to pass the $\not\!\!E_T$ threshold. Therefore, we apply a Z boson veto which removes events where the lepton candidate and an isolated track form an invariant mass within a window of 15 GeV/c^2 of the Z boson mass [28]. In addition, we also reject events with more than one identified lepton candidate.

We also reject electron candidates that are consistent with $\gamma \to e^+e^-$ conversions. This cuts out events with a pair of oppositely charged tracks, one belonging to the electron candidate, that have a separation of less than 2 mm in the $r - \phi$ plane and a difference in $\cot\theta < 0.04$, where θ is the opening angle of the two tracks.

Finally, we reject events with a muon candidate that are not consistent with the timing of the beam crossing to reject cosmic ray muons.

The effect of these selection criteria on the event detection efficiency will be discussed in the next chapter.

Chapter 4

Event Acceptance

The predicted number of $t\bar{t}H$ signal events in a given sample is

$$N_{evt}^{predict} = \sigma_{t\bar{t}H}^{SM} \times A_{evt} \times \mathcal{L}_{int}, \tag{4.1}$$

where $\sigma_{t\bar{t}H}^{SM}$ is the Standard Model predicted cross section for $p\bar{p} \to t\bar{t}H$ events at 1.96 TeV, A_{evt} is the event detection efficiency (event acceptance), and $\mathcal{L}_{int} = \int \mathcal{L}dt$ is the total integrated luminosity of the data sample. The event acceptance A_{evt} is the fraction of $t\bar{t}H$ events that pass our selection criteria.

In this chapter, we describe the estimation of the event acceptance A_{evt} for $t\bar{t}H$ events at CDF. We use events from Monte Carlo generation to determine this efficiency and we correct this efficiency with factors derived from data studies for lepton identification, b-tagging, and trigger efficiencies. We then consider various sources of systematic uncertainties and calculate their effects on the event acceptance.

4.1 Monte Carlo Acceptances

To understand the behaviour and interaction of $t\bar{t}H$ events with the CDF detector, we rely on Monte Carlo techniques. Using such techniques, we can simulate the detector response to $t\bar{t}H$ events, without statistical limitations.

Monte Carlo event generators generate random events in the kinematical phase space, and assign a differential cross section to each event by evaluating the matrix element squared for the physical process and multiplying it with the phase space factor. Based on this, the Monte Carlo generators provide kinematical distributions of final state particles that reliably model the respective physical processes.

We use the Pythia Monte Carlo generator [29] to generate $p\bar{p} \to t\bar{t}H$ events at a centre-of-mass energy of 1.96 TeV. These events are generated for a range of Higgs masses from 100 to 135 GeV/c^2. The top quark mass for these Monte Carlo samples is set to 175 GeV/c^2 [10].

The detector response to these Monte Carlo events is simulated using a CDF detector simulation [30] which is based on the GEANT 3 package [31]. Most of the interactions of particles with matter are modelled using the standard GEANT algorithms. However, charged particle ionization and drift properties in the COT are parameterized and tuned to data. In addition, the behaviour of calorimeter showers is modelled by the use of the parameterized shower development package called GFLASH [32], with the parameters of the electromagnetic and hadronic showers tuned to inclusive jet data.

Using the event selection described in Chapter 3, we assign each successive cut a stage number. Stage 0 is the initial jet binning in the Monte Carlo reconstruction. Stage 1 requires a primary vertex to be observed with $|z| < 60$ cm. Stage 2 requires the existence of at least one electron or muon candidate with the lepton isolation cut to be applied later. Leptons can be identified as CEM electrons, CMUP muons, or CMX muons. Stage 3 requires that the event $\not\!\!E_T$ be larger than 10 GeV. Stage 4 requires that the electrons and muons pass the isolation cut of 0.1. Stage 5 vetoes events where more than one electron or muon candidate has been identified. Stage 6 vetoes events that are consistent with the presence of a Z boson candidate, identified by having an electron or muon candidate and an isolated track forming an invariant mass within the window (76,106) GeV/c^2. Stage 7 requires that the identified lepton candidate passes conversion cuts for

Stage Number	Description
0	Initial
1	primary vertex $\|z\| < 60$ cm
2	≥ 1 lepton
3	$\not\!\!E_T > 10$ GeV
4	Lepton isolation < 0.1
5	Veto multi-leptons
6	Z-boson veto
7	Veto conversion and cosmic events
8	$\|z_{lepton} - z_{vtx}\| < 5$ cm
9A	≥ 3 SECVTX tight tags
9B	≥ 3 SECVTX loose tags
9C	≥ 3 Combined tight tags
9D	≥ 3 Combined loose tags

Table 4.1: Successive event selection criteria stages.

electrons events and cosmic ray event cuts for muon events. Stage 8 demands that the event primary vertex be within 5 cm of the lepton z_0. Finally, Stage 9 requires 3 or more b-tagged jets. We divide Stage 9 into four different categories: 9A refers to events with 3 or more b-tagged jets using the SECVTX tight tagger; 9B for the SECVTX loose tagger; 9C for the Combined tight tagger; and 9D for the Combined loose tagger. These event selection stages are shown in Table 4.1.

We tabulate the Monte Carlo event flows for $t\bar{t}H$ events where $m_H = 120$ GeV/c^2 for each jet bin. The event flows for CEM electron events are shown in Table 4.2. Analogous event flows for CMUP and CMX muon events are shown in Tables 4.3 and 4.4, respectively.

Based on these Monte Carlo event flows, we obtain a Monte Carlo acceptance A_{MC}

CEM Electrons	0-jet	1-jet	2-jet	3-jet	4-jet	5-jet	$\geq$ 6-jet	Total
Stage 0	31	777	8349	42735	123201	220543	565206	960842
Stage 1	28	737	8080	41259	118506	211910	543036	923556
Stage 2	10	268	2880	12649	29848	42112	67752	155519
Stage 3	9	266	2823	12410	29144	40814	63950	149416
Stage 4	9	259	2582	10607	22864	28476	33478	98275
Stage 5	2	161	1775	8200	19686	26327	32264	88415
Stage 6	2	145	1585	7433	18328	25060	31330	83883
Stage 7	2	145	1575	7324	17851	24049	28469	79415
Stage 8	2	145	1575	7315	17817	23973	28251	79078
Stage 9A	0	1	12	247	1147	2230	3195	6832
Stage 9B	0	1	25	462	1998	3680	5317	11483
Stage 9C	0	1	24	478	1996	3869	5471	11839
Stage 9D	0	1	41	691	2983	5413	7690	16819

Table 4.2: Event flow for Monte Carlo $t\bar{t}H$ events with a CEM electron candidate (m_H = 120 GeV/c^2).

CMUP Muons	0-jet	1-jet	2-jet	3-jet	4-jet	5-jet	≥6-jet	Total
Stage 0	31	777	8349	42735	123201	220543	565206	960842
Stage 1	28	737	8080	41259	118506	211910	543036	923556
Stage 2	10	210	1872	7847	16689	19954	20080	66662
Stage 3	10	207	1837	7692	16322	19441	19520	65029
Stage 4	9	186	1643	6600	13237	15000	13247	49922
Stage 5	4	113	1069	4992	11210	13914	12743	44045
Stage 6	3	99	956	4613	10597	13389	12379	42036
Stage 7	3	99	956	4607	10576	13364	12339	41944
Stage 8	3	99	956	4606	10572	13357	12335	41928
Stage 9A	0	0	3	179	743	1245	1358	3528
Stage 9B	0	0	10	310	1258	2077	2338	5993
Stage 9C	0	1	8	313	1294	2119	2346	6081
Stage 9D	0	1	26	443	1849	2978	3337	8634

Table 4.3: Event flow for Monte Carlo $t\bar{t}H$ events with a CMUP muon candidate (m_H = 120 GeV/c^2).

CMX Muon	0-jet	1-jet	2-jet	3-jet	4-jet	5-jet	≥6-jet	Total
Stage 0	31	777	8349	42735	123201	220543	565206	960842
Stage 1	28	737	8080	41259	118506	211910	543036	923556
Stage 2	5	77	689	2721	5578	6392	6525	21987
Stage 3	5	77	671	2671	5444	6224	6327	21419
Stage 4	5	72	602	2336	4554	4954	4532	17055
Stage 5	1	40	372	1692	3812	4542	4364	14823
Stage 6	1	35	333	1545	3601	4363	4237	14115
Stage 7	1	35	333	1545	3596	4355	4233	14098
Stage 8	1	35	333	1543	3595	4353	4228	14088
Stage 9A	0	0	2	73	274	446	503	1298
Stage 9B	0	0	5	111	467	714	808	2105
Stage 9C	0	0	7	116	452	755	831	2161
Stage 9D	0	0	11	161	632	1045	1206	3055

Table 4.4: Event flow for Monte Carlo $t\bar{t}H$ events with a CMX muon candidate (m_H = 120 GeV/c^2).

for our range of selected Higgs masses. From these event flows, it is evident that the requirement of an identified charged electron or muon and the requirement of three b-tags are the greatest sources of inefficiency. The event selection requires that at least 5 jets pass the jet selection criteria.

4.2 Data Corrections

It is known that the Monte Carlo simulation does not perfectly model the response of the CDF detector. Therefore, the Monte Carlo acceptance A_{MC} needs to be corrected to account for such differences.

The event flows shown in Tables 4.2-4.4 already take into account the difference in b-tagging efficiency between Monte Carlo events and events in data. The ratio of b-tagging efficiencies $\epsilon_{data}^{b-tag}/\epsilon_{MC}^{b-tag}$ for the four different taggers is shown in Table 4.5. This ratio of efficiencies (correction factor) is measured using b-jets in inclusive jet Monte Carlo samples and then by comparing the tagging efficiency of these with b-jet candidates with evidence of semi-leptonic b-decays [33].

Ratio of b-tagging efficiencies $\epsilon_{data}^{b-tag}/\epsilon_{MC}^{b-tag}$				
Tagger	SECVTX Tight	SECVTX Loose	Combined Tight	Combined Loose
$\epsilon_{data}^{b-tag}/\epsilon_{MC}^{b-tag}$	0.909 ± 0.060	0.927 ± 0.066	0.89 ± 0.06	0.90 ± 0.07

Table 4.5: Ratio of data and Monte Carlo b-tagging efficiencies for the four different taggers.

We apply the correction factor $c_{corr}^{b-tag} = \epsilon_{data}^{b-tag}/\epsilon_{MC}^{b-tag}$ to the Monte Carlo sample on a jet-by-jet basis. For each jet that is b-tagged in the Monte Carlo sample, we randomly reject a fraction of $1 - c_{corr}^{b-tag}$ of such jets. Because the above event flows already take into account this correction, the Monte Carlo acceptance A_{MC} does not need to be further corrected for the differences in b-tagging efficiency between the Monte Carlo and data

samples.

There is also a correction factor that needs to be applied to the efficiency of identifying electron and muon candidates. This correction factor is determined by comparing the electron and muon identification efficiencies for Z boson candidates with Monte Carlo samples [34]. These correction factors are shown in Table 4.6.

Ratio of lepton identification efficiencies $\epsilon^{id}_{data}/\epsilon^{id}_{MC}$			
Lepton Type	CEM electrons	CMUP muons	CMX muons
$\epsilon^{id}_{data}/\epsilon^{id}_{MC}$	0.996 ± 0.004	0.921 ± 0.011	1.000 ± 0.006

Table 4.6: Ratio of data and Monte Carlo lepton identification efficiencies for CEM electrons, CMUP muons, and CMX muons.

Because we require exactly one identified electron or muon in our event selection, we apply the lepton identification efficiency scale factors to the Monte Carlo acceptance A_{MC}.

A final correction to the Monte Carlo acceptance is the trigger efficiency [36]. These efficiencies are shown in Table 4.7.

Trigger Efficiencies			
Trigger Type	CEM electrons	CMUP muons	CMX muons
ϵ_{trig}	0.979 ± 0.003	0.905 ± 0.005	0.962 ± 0.005

Table 4.7: Trigger efficiencies for CEM electrons, CMUP muons, and CMX muons.

The estimated acceptance for $p\bar{p} \to t\bar{t}H$ at $E_{CM} = 1.96$ TeV is given by

$$A_{evt} = A_{MC} \times \frac{\epsilon^{id}_{data}}{\epsilon^{id}_{MC}} \times \epsilon_{trig}. \tag{4.2}$$

We show this evaluated acceptance as a function of m_H in Figure 4.1.

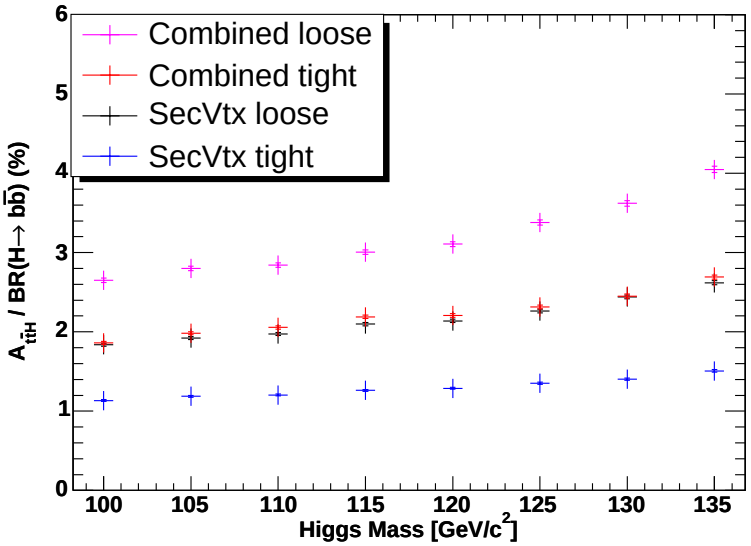

Figure 4.1: The $t\bar{t}H$ acceptance divided by $H \to b\bar{b}$ branching ratio as a function of Higgs mass. The uncertainties shown are statistical only.

4.3 Systematic Uncertainties on the Event Acceptance

Systematic uncertainties on the event acceptance arise from a variety of sources. The largest systematic uncertainty on the event acceptance is due to the uncertainty on the b-tagging efficiency in data, quantified in Table 4.5. We also include systematic effects from the lepton identification efficiency, which is quantified in the lepton identification efficiency correction factor in Table 4.6. The lepton identification efficiency must also take into account the uncertainty of the Monte Carlo simulation on lepton identification efficiency as a function of the event jet multiplicity[1] [35]. The systematic uncertainty of the acceptance from these effects is obtained by varying the correction factors for the b-tagging and lepton identification efficiencies by $+1\sigma$ and -1σ and propagating this to

[1] Because lepton efficiency studies are performed on events with one jet or less, we assign an additional 5% systematic uncertainty to the extrapolation of the lepton identification efficiency in events with 4 or more jets.

the evaluation of A_{evt}.

Other systematic uncertainties on the event acceptance include uncertainties arising from the trigger efficiency, shown in Table 4.7, the jet energy scale, the choice of parton distribution function (PDF), the Monte Carlo modeling of initial state (ISR) and final state (FSR) radiation, and the Monte Carlo modeling of $t\bar{t}H$ events.

The effect of the uncertainties on the trigger efficiency, the jet energy scale, and ISR/FSR on the acceptance is obtained by varying these quantities by one standard deviation and calculating their effect on the event acceptance. We also estimate the systematic uncertainty on Monte Carlo modeling by calculating the difference in event acceptance when we use the Herwig Monte Carlo program [37] instead of the Pythia Monte Carlo generator.

The systematic uncertainty due to the choice of PDF is obtained by comparing the differences in event acceptance by varying the CTEQ6M PDF [38] within the set of allowed variations and also by investigating the effect of MRST PDFs [39] on the acceptance.

Table 4.8 lists the different sources of systematic uncertainties and their effect on the event acceptance. With the exception of the uncertainty from b-tagging efficiency, these systematic effects have been calculated for one Higgs mass ($m_H = 120$ GeV/c^2), and applied to all Higgs masses. The systematic uncertainty from the b-tagging efficiency is calculated for each Higgs mass separately.

We show the event acceptance divided by $BR(H \to b\bar{b})$ with systematic uncertainties in Figure 4.2. From the acceptance we can calculate the predicted event yield using equation 4.1. The predicted event yield is shown in Figure 4.3.

Uncertainties (%)	Tight SECVTX	Loose SECVTX	Tight Combined	Loose Combined
Jet Energy Scale	3.5	4.3	4.3	3.5
PDF	0.5	0.6	0.6	0.6
ISR/FSR	1.5	2.0	1.0	1.9
Monte Carlo Model	0.6	0.6	0.6	0.6
Lepton ID (CEM)	5.0	5.0	5.0	5.0
Lepton ID (CMUP)	5.2	5.2	5.2	5.2
Lepton ID (CMX)	5.1	5.1	5.1	5.1
b-tagging efficiency	17	16	18	18
Total Uncertainty	18	18	19	19

Table 4.8: Systematic uncertainties on the $t\bar{t}H$ event acceptance.

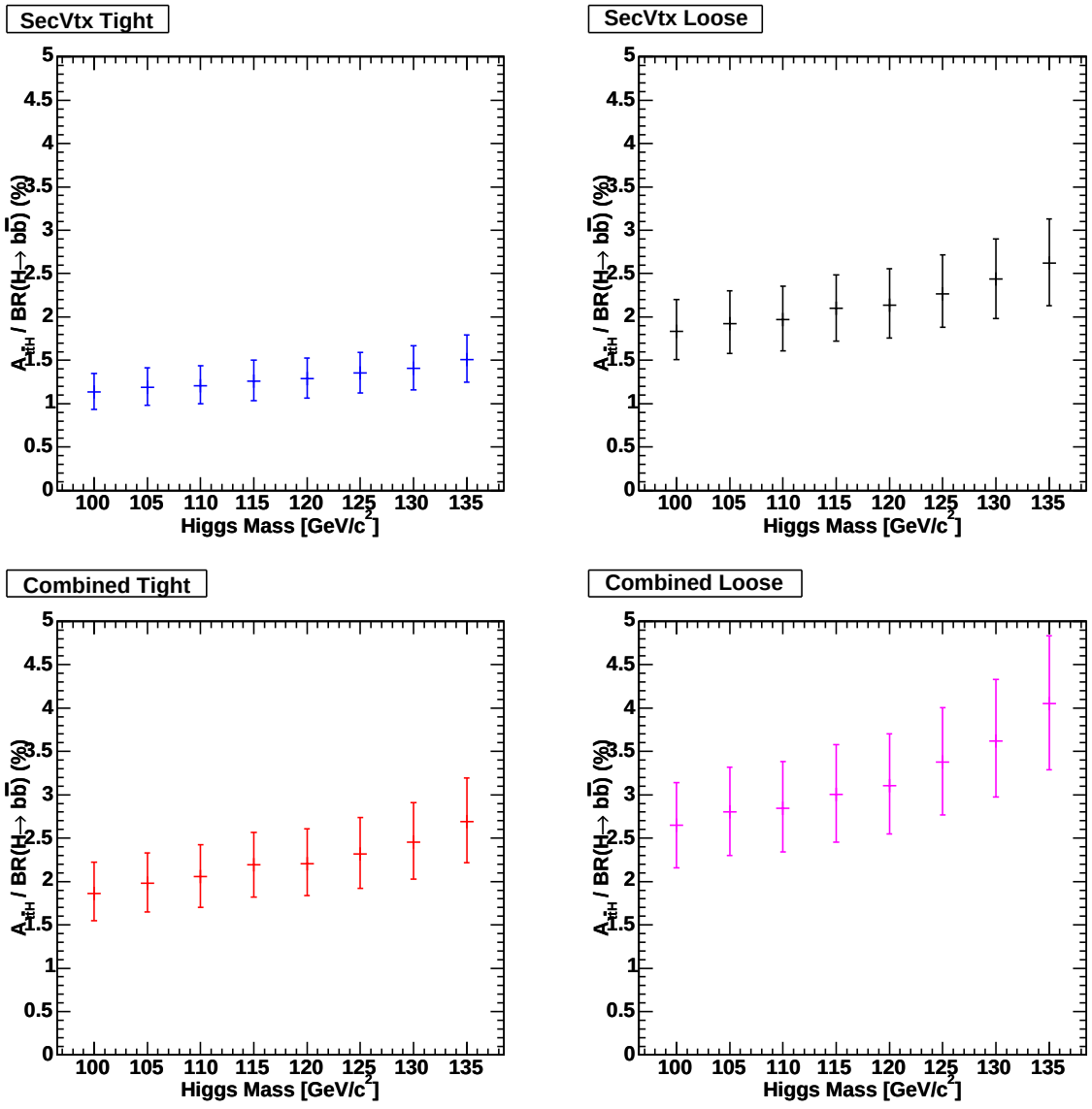

Figure 4.2: The $t\bar{t}H$ acceptance divided by $H \to b\bar{b}$ branching ratio as a function of Higgs mass. The uncertainties shown include systematic uncertainties.

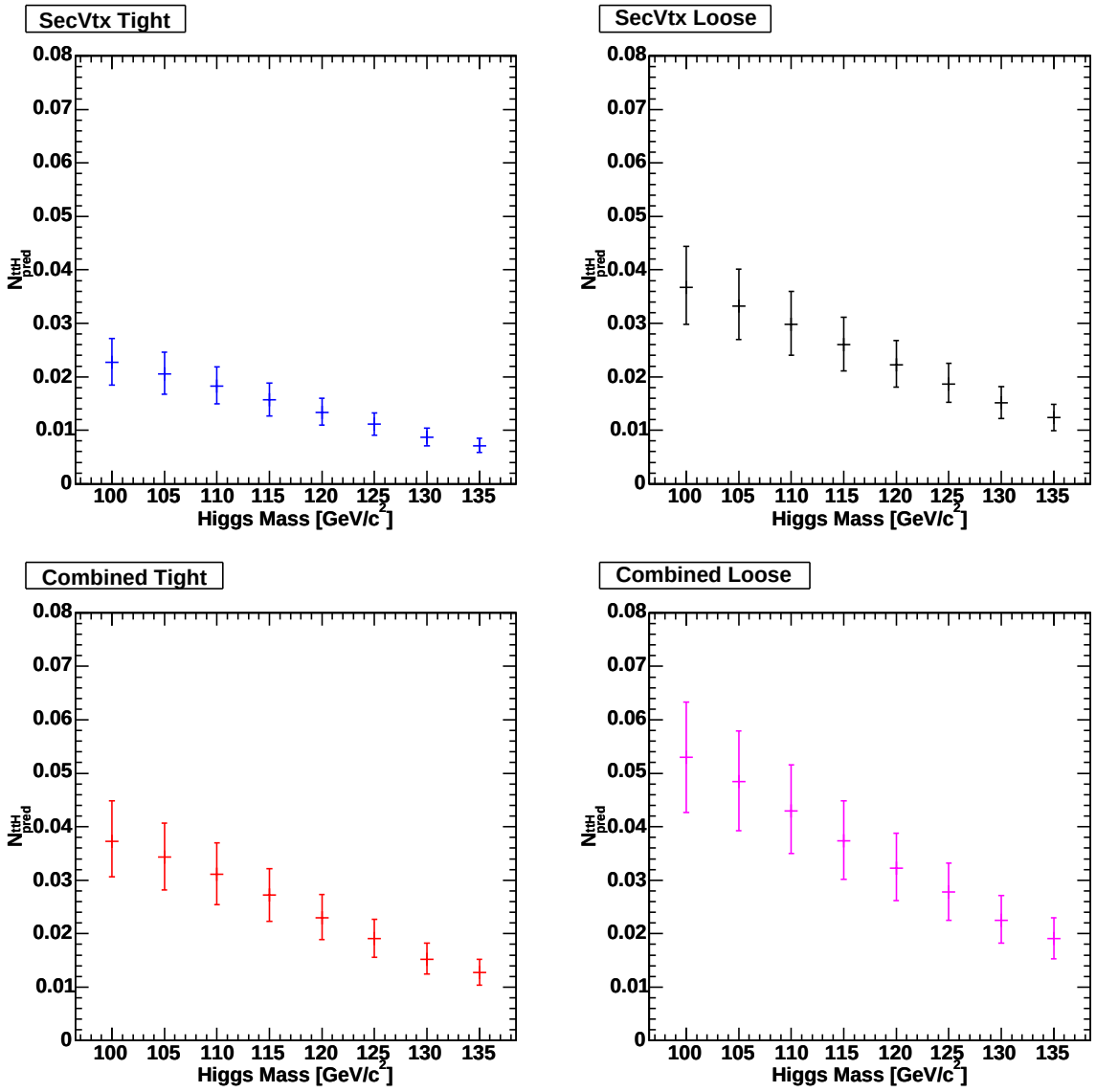

Figure 4.3: The expected $t\bar{t}H$ signal event yield as a function of Higgs mass for a data sample of 319 pb^{-1}.

Chapter 5

Background Estimates

In our search, the events that pass the event selection criteria are a mixture of $t\bar{t}H$ signal events and Standard Model background events. In this chapter, we estimate background yield that contributes to the signal region that we have defined.

We divide the Standard Model background into three categories: mistag background, multijet background, and irreducible background. Mistag background events are events that have less than three heavy flavour jets (b-jets or c-jets), but nevertheless have three jets that are b-tagged. Multijet background events are those that do not have have a real leptonic W decay ($W \to e\nu_e, W \to \mu\nu_\mu$), but include a jet that mimics a leptonic signature in the detector. Finally, irreducible background events are those with the same final state signature as $t\bar{t}H$ events: a charged lepton (e or μ), missing transverse energy, and at least three final state heavy flavour jets.

We will describe our method of estimating the background yields for each of these three types of background. However, we will first discuss how we predict the probability of mistagging a light quark jet as originating from a heavy flavour quark.

5.1 Predicting Mistag Rates

All estimates of the background composition in the signal region rely on evaluating the probability that a light quark jet (jets originating from u, d, s quarks) is misidentified as originating from a heavy flavour quark (jets originating from b, c quarks).

In order to evaluate the mistag rate for a given jet, the concept of a "negative" tag is used. For the SECVTX algorithm, a negatively tagged jet is a jet that has tracks that form a secondary vertex displaced away from the jet axis relative to the primary vertex. A positively tagged jet is a jet that has tracks that form a secondary vertex that is displaced towards the jet axis relative to the primary vertex. Figure 5.1 illustrates secondary vertices that would give negative and positive b-tagged jets.

For the JETPROB algorithm, no secondary vertex is formed. Therefore, a negatively tagged jet for the JETPROB algorithm are jets whose jet probabilities are below the probability threshold using tracks with negative impact parameters. Positively tagged jets for the JETPROB algorithm are those with jet probabilities that pass the given requirements using positive impact parameter tracks.

Figure 5.2 illustrates the concept of tracks with positive impact parameters and tracks with negative impact parameters. The angle between the jet axis and the impact parameter vector forms an acute angle (shown as ϕ_1) for a track with a positive impact parameter. Conversely, for a negative impact parameter track, this angle (shown as ϕ_2) is obtuse.

Jets that are negatively b-tagged arise due to mismeasurements in the track trajectories and vertex fits, because such jets are not the result of long-lived heavy flavour hadrons that travel in the direction of the jet axis before subsequently decaying. Therefore, the negative tag rate of jets gives us the probability that a light flavour jet is mistagged.

We parameterize the negative tag rate of jets as a function of five variables that are correlated with the mistag probability: the jet E_T, jet η, jet ϕ, the number of tracks in

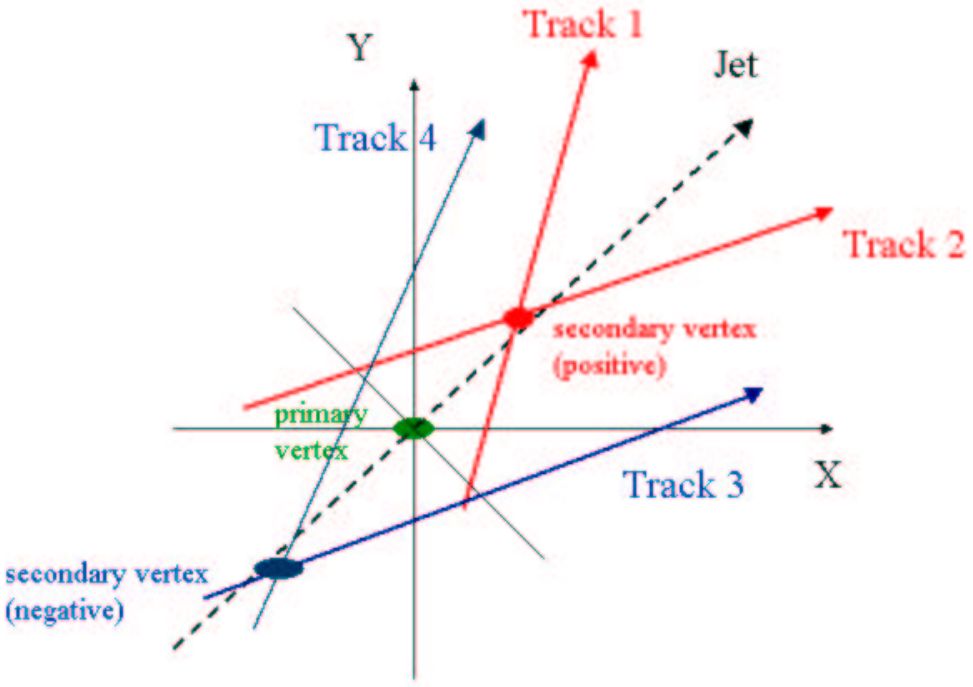

Figure 5.1: Illustration of secondary vertices that give positive b-tags (red) and negative b-tags (blue).

a jet N_{trk}, and the scalar sum of jet transverse energy in the event $\sum_{jet} E_T$. The negative tag rate is measured using inclusive jet data samples, and extensive cross checks are performed to ensure that this parameterization has good predictive power [40].

Figures 5.3 and 5.4 show that this parameterization can predict the variation of the jet tag rates as a function of instantaneous luminosity for the tight and loose SECVTX taggers, respectively. Here the parameterization is formed with only half the events in the inclusive jet sample, and cross checked with the other half of the events. The prediction of the parameterization is compared with the observed tag rates. The tag rate as a function of other variables are also checked including the z-coordinate of the primary vertex, the

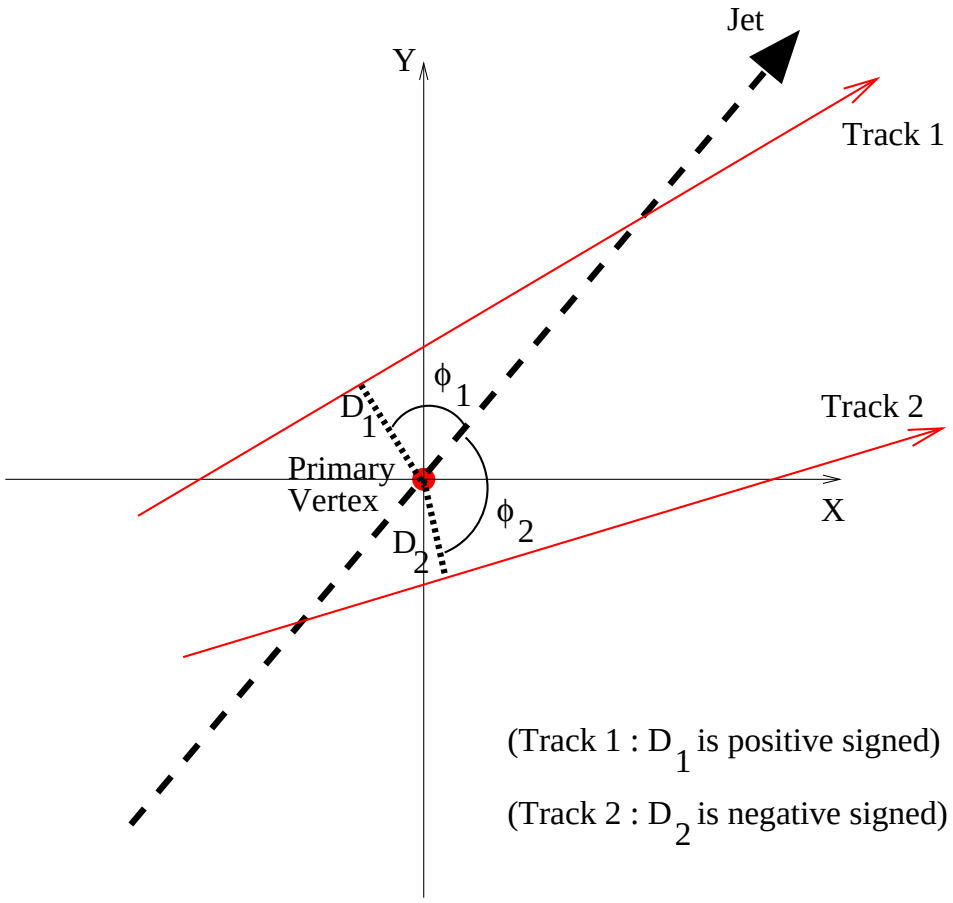

Figure 5.2: Illustration of a positive impact parameter track (Track 1) and a negative impact parameter track (Track 2).

vertex resolution in the transverse plane, and the jet multiplicity of the event. Analagous checks are performed with the Combined Tagger.

We use the parameterization of mistag rates from the inclusive jet sample to predict the mistag rates in our high p_T lepton samples. Figures 5.5 and 5.6 confirm that the negative tag rate prediction is consistent with our observation of the negative tag rate, as a function of jet E_T and η, respectively, for the loose SECVTX tagger. This consistency holds true for all b-tagging algorithms considered here.

It is known however, that the negative tag rate underestimates the fake positive tag rates [41]. This is because the negative tag rate does not take into account fake b-tags due to secondary material interactions or secondary vertices that are formed from K_s and Λ

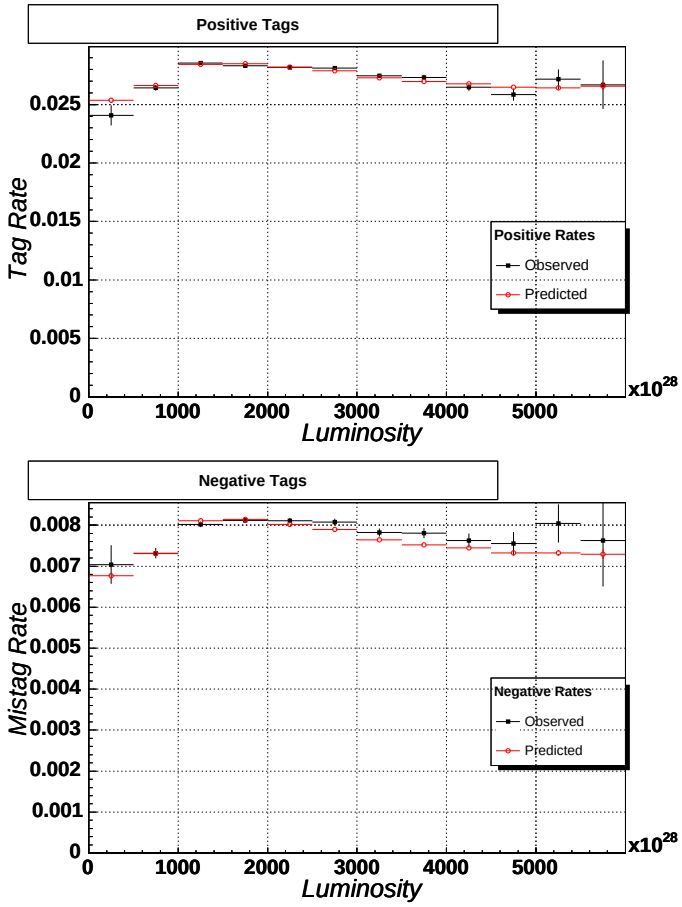

Figure 5.3: Observed and predicted tag rates for the tight SECVTX tagger in inclusive jet events as a function of the instantaneous luminosity. The luminosity is measured in units of $\text{cm}^{-2} \cdot \text{s}^{-1}$. The positive tag rate appears in the upper plot, and the negative tag rate appears in the lower plot.

particles. Studies have shown that the negative tag rate needs to be increased by a factor of R_{asym} in order to account for these effects. This asymmetry is $R_{asym} = 1.37 \pm 0.12$ for the SECVTX algorithm [42] and $R_{asym} = 1.57 \pm 0.13$ for the JETPROB algorithm [43]. These factors are determined by fitting a quantity called the pseudo-$c\tau$ of jets in inclusive jet samples, defined by

$$\text{pseudo-}c\tau = L_{xy} \times \frac{M_{vtx}}{P_T^{vtx}} \tag{5.1}$$

where M_{vtx} is the invariant mass formed using tracks from the jet vertex, and P_T^{vtx} is

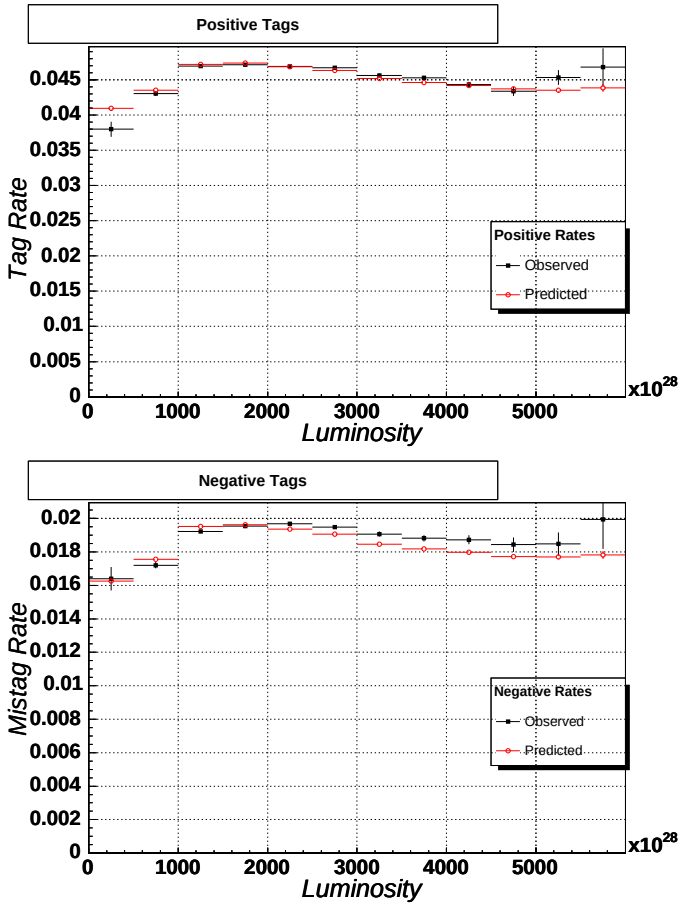

Figure 5.4: Observed and predicted tag rates for the loose SECVTX tagger in inclusive jet events as a function of the instantaneous luminosity. The luminosity is measured in units of $cm^{-2} \cdot s^{-1}$. The positive tag rate appears in the upper plot, and the negative tag rate appears in the lower plot.

the vector summation of the transverse momenta of those tracks. By comparing the pseudo-$c\tau$ distributions in inclusive jet samples to Monte Carlo events and heavy flavour enriched samples, a measurement of the mistag asymmetry can be made.

5.2 Mistag Background

We use the mistag parameterization to predict the number of background events that have been mistagged. We need to consider three types of mistagged events: events

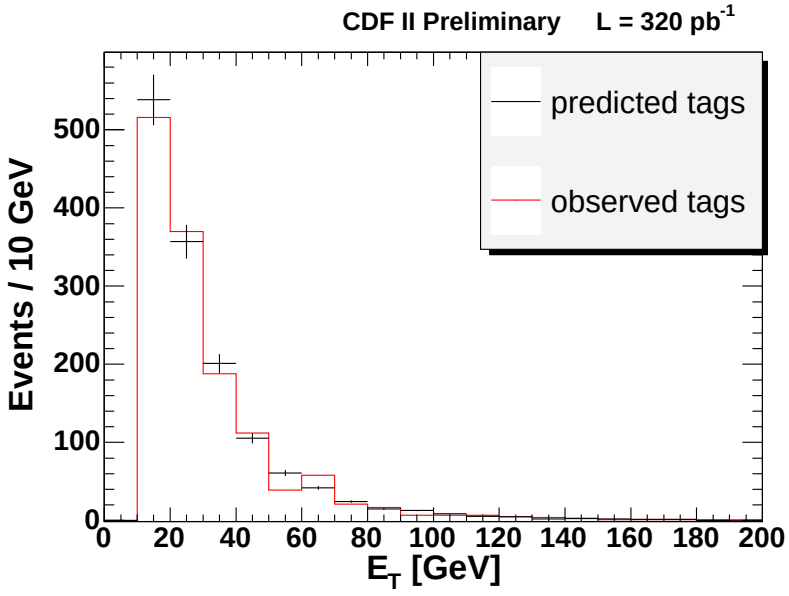

Figure 5.5: Comparison of the prediction of negative tags from the inclusive jet sample with the observed number of negative tags in the high p_T lepton sample as a function of the jet E_T for the loose SECVTX tagger.

with one single mistag, events with two mistags, and events where there all three b-jet candidates are mistagged.

To calculate the probability that an event is mistagged, we first define some mathematical quantities. We define m as the mistag rate (equal for negative and positive mistags), ϵ_+ as the b-tagging efficiency, and ϵ_- as the rate for tagging a b-jet negatively. We find that in the case of single, double, and triple mistagged events, that the probability that an event is mistagged is given by

$$P(+++) = P(++-) - P(+--) + P(---), \tag{5.2}$$

where $P(++-)$ is the event probability of obtaining two positive b-tags and a negative b-tag, $P(+--)$ is the event probability of obtaining one positive b-tag and two negative b-tags, and $P(---)$ is the event probability of observing three negative b-tags. Table 5.1 illustrates this mathematical relationship for three jet events with topologies bbq (two real b-jets and a light quark jet), bqq (one real b-jet and two light quark jets), and qqq (three

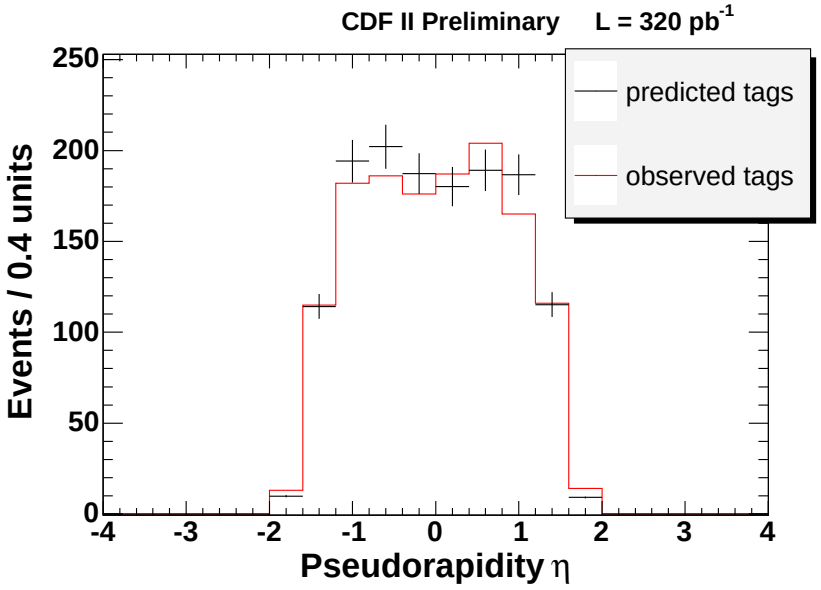

Figure 5.6: Comparison of the prediction of negative tags from the inclusive jet sample with the observed number of negative tags in the high p_T lepton sample as a function of the jet η for the loose SECVTX tagger.

light quark jets). It can be shown that this relationship also holds for events with jet multiplicities greater than three.

Jet Topology	bbq	bqq	qqq
$P(++-)$	$\epsilon_+^2 m + 2\epsilon_+\epsilon_- m$	$2\epsilon_+ m^2 + \epsilon_- m^2$	$3m^3$
$P(+--)$	$2\epsilon_+\epsilon_- m + \epsilon_-^2 m$	$\epsilon_+ m^2 + 2\epsilon_- m^2$	$3m^3$
$P(---)$	$\epsilon_-^2 m$	$\epsilon_- m^2$	m^3
$P(+++)$	$\epsilon_+^2 m$	$\epsilon_+ m^2$	m^3

Table 5.1: Mathematical quantities illustrating the relationship in Equation 5.1.

We sum all the event probabilities $P(++-), P(+--), P(---)$ in our data sample for each event. To obtain $\sum_{evt} P(++-)$, we look at events with two observed positive b-tags, and use the mistag parameterization to find the probability that any other jet is mistagged. For the event probability $P(+--)$, we look for events with one observed

positive b-tag, and calculate the probability for at least two other jets to be mistagged. Finally to estimate $\sum_{evt} P(---)$, we sum up the event probabilities for all events to have three or more jets mistagged.

The sum of event probabilities for the mistag background is shown in Table 5.2 for the different b-tagging algorithms. These event probabilities have been corrected for the mistag asymmetry factor R_{asym}.

Tagger	Tight SECVTX	Loose SECVTX	Tight Comb.	Loose Comb.
$\sum_{evt} P(++-)$	0.18 ± 0.09	0.60 ± 0.23	0.87 ± 0.29	1.59 ± 0.53
$\sum_{evt} P(+--)$	0.013 ± 0.003	0.114 ± 0.025	0.074 ± 0.021	0.36 ± 0.10
$\sum_{evt} P(---)$	0.00044 ± 0.00006	0.016 ± 0.002	0.0055 ± 0.0008	0.045 ± 0.006
$\sum_{evt} P(+++)$	0.17 ± 0.09	0.50 ± 0.23	0.80 ± 0.29	1.27 ± 0.54

Table 5.2: Sum of event probabilities for $P(++-), P(+--), P(---)$ and the predicted mistag component $\sum_{evt} P(+++)$ when at least five jets are required in the event. Uncertainties shown are statistical only.

Though the mistag rate per jet for the Tight Combined tagger is lower than the loose SECVTX tagger, we estimate a larger yield of mistag background events for the Tight Combined tagger. This is due to the events in the sample used to calculate $P(++-)$, which come from events with 2 or more b-tagged jets. For the Tight Combined tagger, 9 events are observed to have 2 or more b-tagged jets, while for the loose SECVTX tagger, only 7 events are observed with this same property. This results in an apparent upward fluctuation of the mistag estimate using the Tight Combined tagging algorithm.

We assign systematic uncertainties to the estimate of the mistag background. The parameterization of the mistag rates in the inclusive jet data samples has a systematic uncertainty arising from sample and trigger biases [40]. We also assign a systematic un-

certainty due to the uncertainty of the mistag asymmetry factor R_{asym}. The systematic uncertainty on the background estimate due to R_{asym} is evaluated by varying the asymmetry factor by $\pm 1\sigma$ and investigating its effect on the mistag background estimate. The effect of these systematic uncertainties on the mistag background estimate is shown in Table 5.3. In Table 5.4, we display the mistag background prediction for all the taggers and jet requirements.

Source	Tight SECVTX	Loose SECVTX	Tight Comb.	Loose Comb.
Parameterization	8%	6%	9%	7%
R_{asym}	8.5%	7.5%	8.8%	7.6%

Table 5.3: Systematic uncertainties on the mistag background estimate for the different b-tagging algorithms.

Tagger	Tight SECVTX	Loose SECVTX	Tight Comb.	Loose Comb.
Mistag Estimate	0.17 ± 0.09	0.50 ± 0.23	0.80 ± 0.31	1.27 ± 0.56

Table 5.4: Mistag background estimate as the number of candidate events for the different b-tagging algorithms.

As a cross check, we compare the mistag parameterization prediction with the observed number of events with: one single negative tag ($-$), two negative tags ($--$), three negative tags ($---$), one positive and one negative tag ($+-$), one positive and two negative tags ($+--$), and two positive and one negative tag ($++-$). We remove the requirements on $\not\!\!E_T$ and jet multiplicity to increase the statistical size of the sample. These predictions are shown in Table 5.5, and show that the mistag parameterization provides a reliable method of predicting mistags in the sample.

Tagger	Tight SecVtx	Loose SecVtx	Tight Comb.	Loose Comb.
$\sum_{evt} P_{predict}(-)$	525 ± 42	1383 ± 83	1360 ± 120	3030 ± 210
$\sum_{evt} P_{observe}(-)$	521	1348	1380	2974
$\sum_{evt} P_{predict}(--)$	0.69 ± 0.12	4.27 ± 0.51	4.07 ± 0.77	15.8 ± 2.2
$\sum_{evt} P_{observe}(--)$	0	5	4	13
$\sum_{evt} P_{predict}(+-)$	9.35 ± 0.75	32.1 ± 1.9	30.5 ± 2.7	84.0 ± 5.9
$\sum_{evt} P_{observe}(+-)$	10	26	27	93
$\sum_{evt} P_{predict}(---)$	0.0015 ± 0.0004	0.0021 ± 0.0004	0.0019 ± 0.0006	0.014 ± 0.003
$\sum_{evt} P_{observe}(---)$	0	0	0	0
$\sum_{evt} P_{predict}(+--)$	0.038 ± 0.006	0.28 ± 0.03	0.25 ± 0.05	1.17 ± 0.16
$\sum_{evt} P_{observe}(+--)$	0	0	0	2
$\sum_{evt} P_{predict}(++-)$	0.727 ± 0.058	2.76 ± 0.17	2.49 ± 0.22	6.78 ± 0.5
$\sum_{evt} P_{observe}(++-)$	0	2	3	8

Table 5.5: Cross checks on the predicted rates of various combinations of tags using the mistag parameterization on the signal sample without the $\not\!\!E_T$ and jet multiplicity cuts.

5.3 Multijet Background

The multijet background arises when a jet has been misidentified as an electron or muon candidate in our event selection. In order to estimate the background arising from this source, we investigate events outside the signal region where the multijet background dominates.

Events with a real leptonic W decay tend to have large $\not\!\!E_T$ due to the undetected

neutrino and an isolated electron or muon. However, multijet background events lack a neutrino or a real lepton, thus they tend to have smaller $\not\!\!E_T$ and charged leptons that are not well isolated from hadronic energy in the calorimeter.

Therefore, we characterize events in a two dimensional Isolation vs. $\not\!\!E_T$ parameter space, shown in Figure 5.7. Here, we have divided this two-dimensional parameter space into four regions: region A contains events with $\not\!\!E_T < 10$ GeV and an identified electron or muon with isolation $I > 0.1$; region B contains events with $\not\!\!E_T < 10$ GeV and an electron or muon with $I < 0.1$; region C contains events with $\not\!\!E_T > 10$ GeV and an electron or muon with $I > 0.1$; and region D is our signal region that contains events with $\not\!\!E_T > 10$ GeV and an electron or muon with $I < 0.1$.

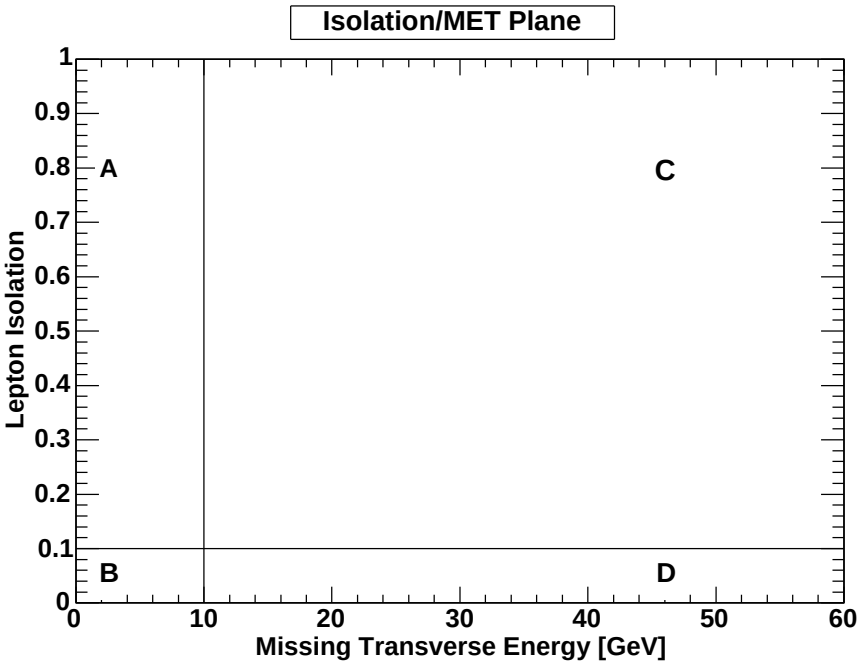

Figure 5.7: Illustration of the two dimensional lepton isolation vs. $\not\!\!E_T$ parameter space. Four regions are mapped out in this parameter space. The signal region is labeled as region D.

The ratio of multijet background events in regions A and B are assumed to be the same as the ratio of such events in regions C and D. This assumption is based on the

hypothesis that the $\not\!\!E_T$ in the event does not affect the lepton isolation distribution for multijet events. Based on this, we can predict the number of multijet events in the signal region D as

$$N_D^{multijet} = \frac{N_B^{multijet} \times N_C^{multijet}}{N_A^{multijet}}. \tag{5.3}$$

In Table 5.6 , we list the observed events in the regions A, B, C, and the estimated multijet component in the signal region D. The events are based on the standard event selection criteria, without any requirement on b-tagged jets. The lepton isolation and $\not\!\!E_T$ requirements have been modified to account for each respective region in the two-dimensional parameter space.

Region	≥ 5 jets
A	28
B	2
C	58
$D_{predicted}^{multijet}$	4.1 ± 2.9

Table 5.6: Observed event yields in regions A, B, C and the estimated multijet component in signal region D. There is no requirement on the number of b-tagged jets observed. Uncertainties for the prediction of multijet events in region D are statistical only.

Prior to requirements on the number of b-tagged jets, we predict there are 4.1 ± 2.9 multijet background events that fall into the signal region. To estimate the multijet background yield for events with at least three b-tags, we assume that the ratio of triple tagged multijet events to multijet events where no b-tag requirement has been made in the signal region D is the same as in the other three regions:

$$N_D^{tripletag} = \frac{N_{A+B+C}^{tripletag}}{N_{A+B+C}^{pretag}} \times N_D^{pretag} \tag{5.4}$$

Because events in regions A, B, C are dominated by multijet background, the events with three b-tagged jets will predominantly come from $b\bar{b}$ events with an additional

mistag. We evaluate $N_{A+B+C}^{tripletag}$ by requiring events with two observed positive tags and calculating the probability for any other jet to be misidentified as a b-jet. We then use this to evaluate the triple tag multijet background component in the signal region D. The values for the quantity $\frac{N_{A+B+C}^{tripletag}}{N_{A+B+C}^{pretag}}$ for each tagger and jet requirement are shown in Table 5.7. The uncertainties for these numbers take into account the systematic uncertainty of the mistag asymmetry factor and the parameterization of mistag rates.

Tagger	Tight SECVTX	Loose SECVTX	Tight Combined	Loose Combined
$\frac{N_{A+B+C}^{tripletag}}{N_{A+B+C}^{pretag}}$ (%)	0.48 ± 0.22	1.58 ± 0.58	1.03 ± 0.42	2.49 ± 0.88

Table 5.7: The evaluation of the quantity $\frac{N_{A+B+C}^{tripletag}}{N_{A+B+C}^{pretag}}$ in percent for each b-tagging algorithm.

Based on this evaluation, we can predict the number of multijet events that pass the full selection criteria. The estimates for the multijet background yield are shown in Table 5.8. We can see that the background component from multijet events is much smaller than the component from mistagged events.

Tagger	Tight SECVTX	Loose SECVTX	Tight Combined	Loose Combined
$N_{background}^{multijet}$	0.020 ± 0.017	0.06 ± 0.05	0.04 ± 0.03	0.10 ± 0.08

Table 5.8: The estimate for the multijet background as the number of candidate events in the signal region.

5.4 Irreducible Background

Irreducible backgrounds are Standard Model processes with the same final state signature as the $t\bar{t}H$ signal. Processes that contribute non-negligibly to the signal region include: $t\bar{t}$ where one of the W daughter bosons in the event decays via $W \to cs$ and where

extra jet candidates can arise from initial or final state radiation, $t\bar{t}+jj$ that includes a $W \to cs$ decay and j is a jet that originates from u, d, or s quarks, $t\bar{t}c\bar{c}$, and $t\bar{t}b\bar{b}$.

All these processes can have the same final state signature as the $t\bar{t}H$ signal: a real lepton and neutrino coming from the decay of a W daughter, three or more heavy flavour jets, and 4 or more jets. To estimate the irreducible background component of the signal region, we use a combination of Monte Carlo and data studies.

We evaluate the ratio of expected Monte Carlo event yields for the irreducible background and the double-tagged mistag background, and multiply this factor by the mistag background evaluated in data studies to obtain the expected background yield for the irreducible background in the signal region. We use the equation

$$N_{irreducible} = \frac{N^{MC}_{irreducible}}{N^{MC}_{mistag}} \times N_{mistag} \tag{5.5}$$

to make this estimation. Here, N_{mistag} is the number of mistagged background events evaluated from data, whereas $N^{MC}_{irreducible}$ and N^{MC}_{mistag} are the background event yields evaluated from Monte Carlo estimates. This combination of Monte Carlo and data methods to estimate the irreducible background has been used for other measurements such as the $t\bar{t}$ production cross section and has been cross checked extensively [44].

The mistag and irreducible backgrounds are dominated by events with top quarks. To evaluate $N^{MC}_{irreducible}$, we generate the processes $t\bar{t}b\bar{b}$, $t\bar{t}c\bar{c}$, $t\bar{t}+jj$ with a $W \to cs$ decay, and $t\bar{t}$ with a $W \to cs$ decay using the ALPGEN Monte Carlo generator [45] and shower the jets using the Pythia generator [29]. To evaluate the factor N^{MC}_{mistag}, we use events from $t\bar{t}+jj$ and $t\bar{t}$ without the presence of a $W \to cs$ decay. Processes without a top quark such as W + jets events have a small contribution and are assumed to contribute at the same rate for both $N^{MC}_{irreducible}$ and N^{MC}_{mistag} so that their effect can be ignored.

The quantity $N^{MC}_{irreducible}/N^{MC}_{mistag}$ is given simply by

$$\frac{A^{MC}_{irreducible} \times \sigma^{LO}_{irreducible}}{A^{MC}_{mistag} \times \sigma^{LO}_{mistag}}, \tag{5.6}$$

where $A^{MC}_{irreducible}$ and A^{MC}_{mistag} are the event acceptances for irreducible and mistag pro-

cesses. The integrated luminosity cancels out since it appears both in the numerator and denominator of this ratio. Table 5.9 shows the ALPGEN leading order cross sections for the processes involved in the background estimate. We assign a 5% systematic uncertainty to the ratio of leading order cross sections given by ALPGEN [44].

Process	σ_{LO} (fb)
$t\bar{t}b\bar{b}$	21.4
$t\bar{t}+jj$	1590
$t\bar{t}$	6020

Table 5.9: ALPGEN leading order cross sections for $t\bar{t}b\bar{b}$, $t\bar{t}+jj$, and $t\bar{t}$.

Event Acceptance (%)	Tight SECVTX	Loose SECVTX	Tight Comb.	Loose Comb.
$t\bar{t}b\bar{b}$	0.286	0.504	0.488	0.761
$t\bar{t}+jj$ (irreducible)	0.030	0.066	0.068	0.125
$t\bar{t}$ (irreducible)	0.006	0.016	0.015	0.035
$t\bar{t}+jj$ (mistag)	0.032	0.081	0.068	0.202
$t\bar{t}$ (mistag)	0.008	0.020	0.032	0.060

Table 5.10: Event acceptances in percent for $t\bar{t}b\bar{b}$, $t\bar{t}+jj$, and $t\bar{t}$.

In Table 5.10, we show the event acceptances for the various processes. Based on the event acceptances and cross sections for these processes, we can evaluate the ratio of event yields $N^{MC}_{irreducible}/N^{MC}_{mistag}$. Other than the 5% uncertainty on the ratio of production cross sections, we find there is a 7% uncertainty due to the systematic uncertainty on the b-tagging efficiency per jet. Other systematic sources such as the jet energy scale and lepton identification efficiency cancel out in the ratio. The ratio $N^{MC}_{irreducible}/N^{MC}_{mistag}$ is shown in Table 5.11 for the different b-tagging algorithms.

We take the ratio $N^{MC}_{irreducible}/N^{MC}_{mistag}$ and multiply it by the mistag estimate N_{mistag}

Tagger	Tight SECVTX	Loose SECVTX	Tight Comb.	Loose Comb.
$N^{MC}_{irreducible}/N^{MC}_{mistag}$	0.91 ± 0.08	0.85 ± 0.07	0.69 ± 0.06	0.62 ± 0.05

Table 5.11: The quantity $N^{MC}_{irreducible}/N^{MC}_{mistag}$ derived from Monte Carlo studies.

from data studies in Table 5.4 to obtain our estimate of the irreducible background. These estimates appear in Table 5.12.

Tagger	Tight SECVTX	Loose SECVTX	Tight Combined	Loose Combined
$t\bar{t}b\bar{b}$	0.01	0.02	0.03	0.05
$t\bar{t}+jj$	0.08	0.21	0.29	0.37
$t\bar{t}$	0.06	0.20	0.24	0.39
$N^{irreducible}_{background}$	0.15 ± 0.08	0.43 ± 0.20	0.55 ± 0.21	0.79 ± 0.34

Table 5.12: The estimate for the irreducible background as the number of candidate events.

5.5 Summary of Background Estimates

We have made estimates of the three types of background that contribute to the event yield in the $t\bar{t}H$ signal region. These background yields are summarized in Table 5.13. The irreducible background and mistag backgrounds make up the largest components, with the multijet background having a very small contribution to the signal region. We also list in the Table the expected signal yield for a Higgs boson with $m_H = 115$ GeV/c^2.

Based on this evaluation of the expected *a priori* event yields, we decide to set the limit on the quantity $\sigma_{t\bar{t}H} \times BR(H \to b\bar{b})$ using the Loose Combined tagger. The Loose Combined tagger algorithm gives the highest event acceptance, which has been one of the primary goals of this search. In addition, because the uncertainties on the background

Source	Tight SECVTX	Loose SECVTX	Tight Comb.	Loose Comb.
Mistag	0.17 ± 0.09	0.50 ± 0.23	0.80 ± 0.31	1.27 ± 0.56
Multijet	0.020 ± 0.017	0.06 ± 0.05	0.04 ± 0.03	0.10 ± 0.08
Irreducible	0.15 ± 0.08	0.43 ± 0.20	0.55 ± 0.21	0.79 ± 0.34
Tot. Background	0.34 ± 0.12	0.99 ± 0.31	1.39 ± 0.37	2.16 ± 0.66
$t\bar{t}H$ Signal	0.016 ± 0.003	0.026 ± 0.005	0.027 ± 0.005	0.037 ± 0.007

Table 5.13: Background yields for the different sources of background when five or more jets are required. The signal yield for $m_H = 115$ GeV/c^2 is also given.

estimates are also statistics limited, the determination of the background is more reliable for the Loose Combined tagger as our control samples are larger.

At the same time, we also attempt to find kinematic variables that further separate the $t\bar{t}H$ signal from the Standard Model background. The following kinematic variables are investigated: the total transverse energy of the event H_T; the electron or muon p_T; the largest, second largest, and third largest b-tagged jet E_T; and the largest, second largest, and third largest invariant $b\bar{b}$ pair mass. The total transverse energy of the event H_T is the scalar sum of the jet transverse energies, the electron E_T or muon p_T, and the $\not\!\!E_T$. Distributions for $t\bar{t}H$ events with $m_H = 115$ GeV/c^2, $t\bar{t}b\bar{b}$, $t\bar{t} + jj$, and $t\bar{t}$ events are shown for these variables in Figures 5.8-5.11. These distributions are normalized to unit area for each process.

Though these distributions show a slight difference between the $t\bar{t}H$ signal and the dominant backgrounds, there is not enough distinction to make any further kinematic selection. Due to the low event yield, we also elect not to fit the observed data to the expected distributions.

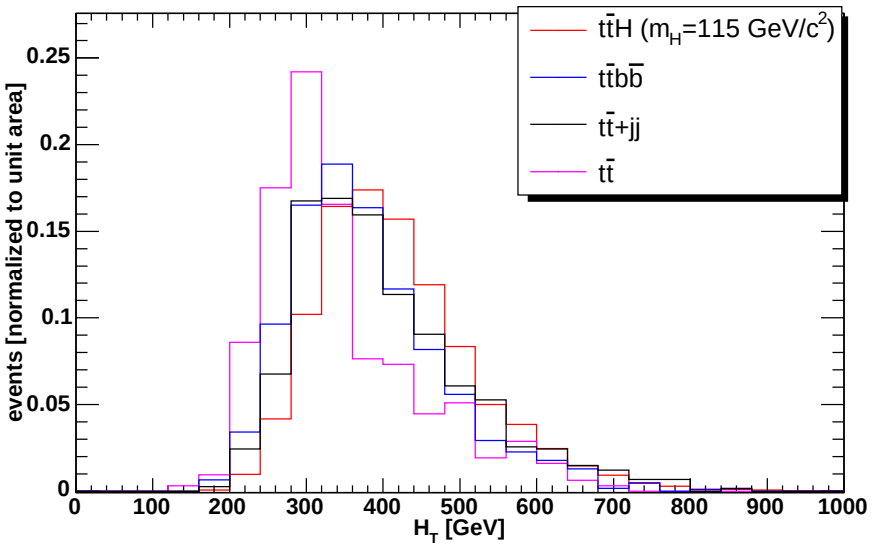

Figure 5.8: Predicted distribution of relevant processes as a function of H_T. All distributions have been normalized to unit area.

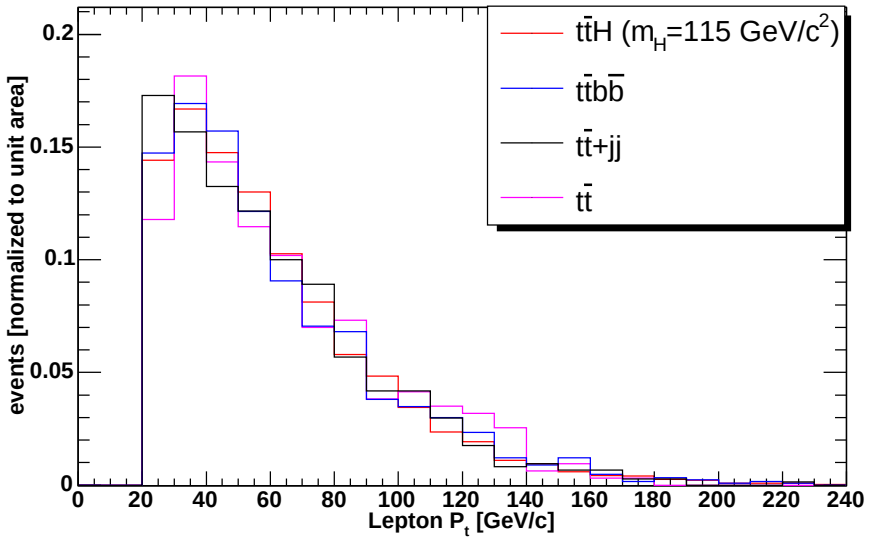

Figure 5.9: Predicted distribution of relevant processes as a function of lepton p_T. All distributions have been normalized to unit area.

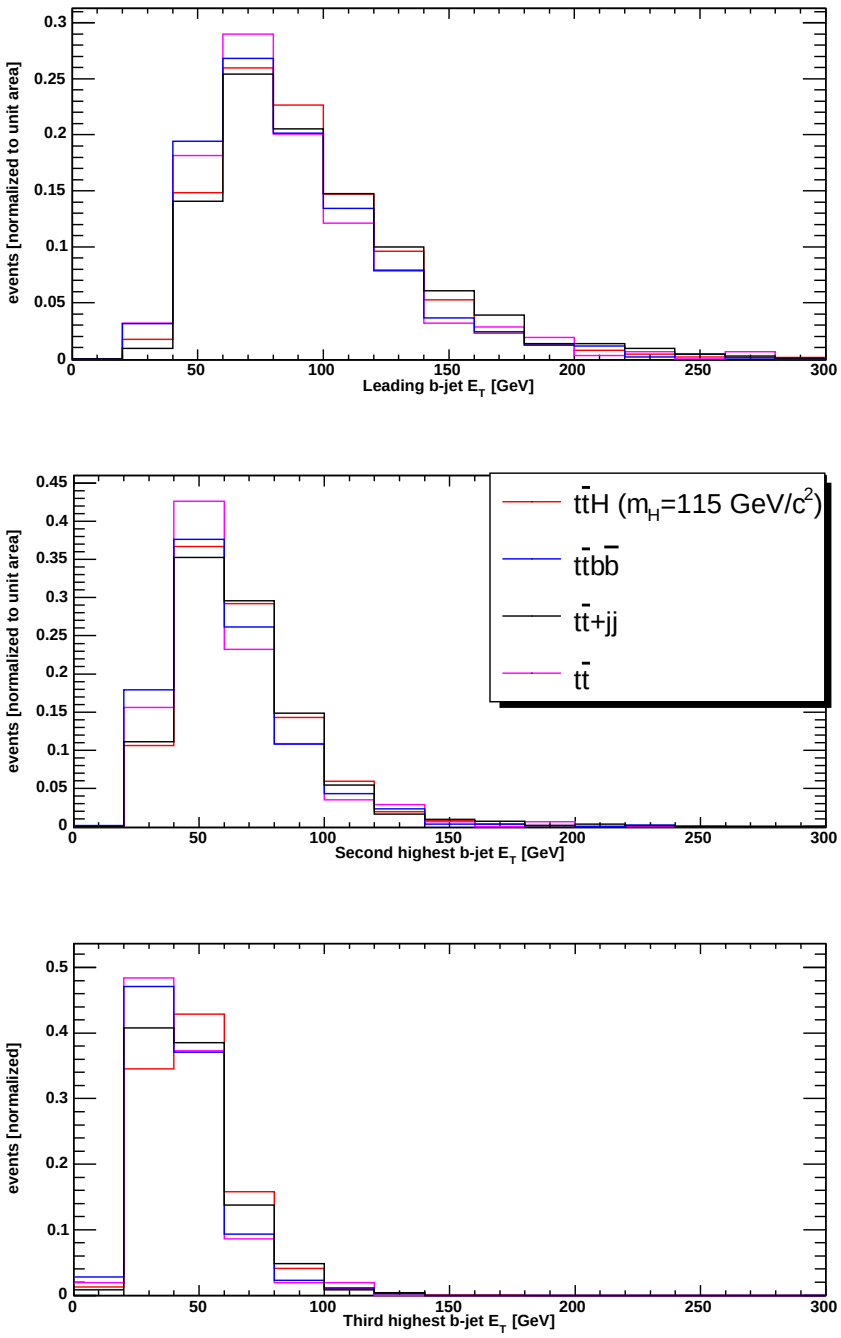

Figure 5.10: Predicted distributions of relevant processes as a function of the largest, second largest, and third largest b-jet E_T. All distributions have been normalized to unit area.

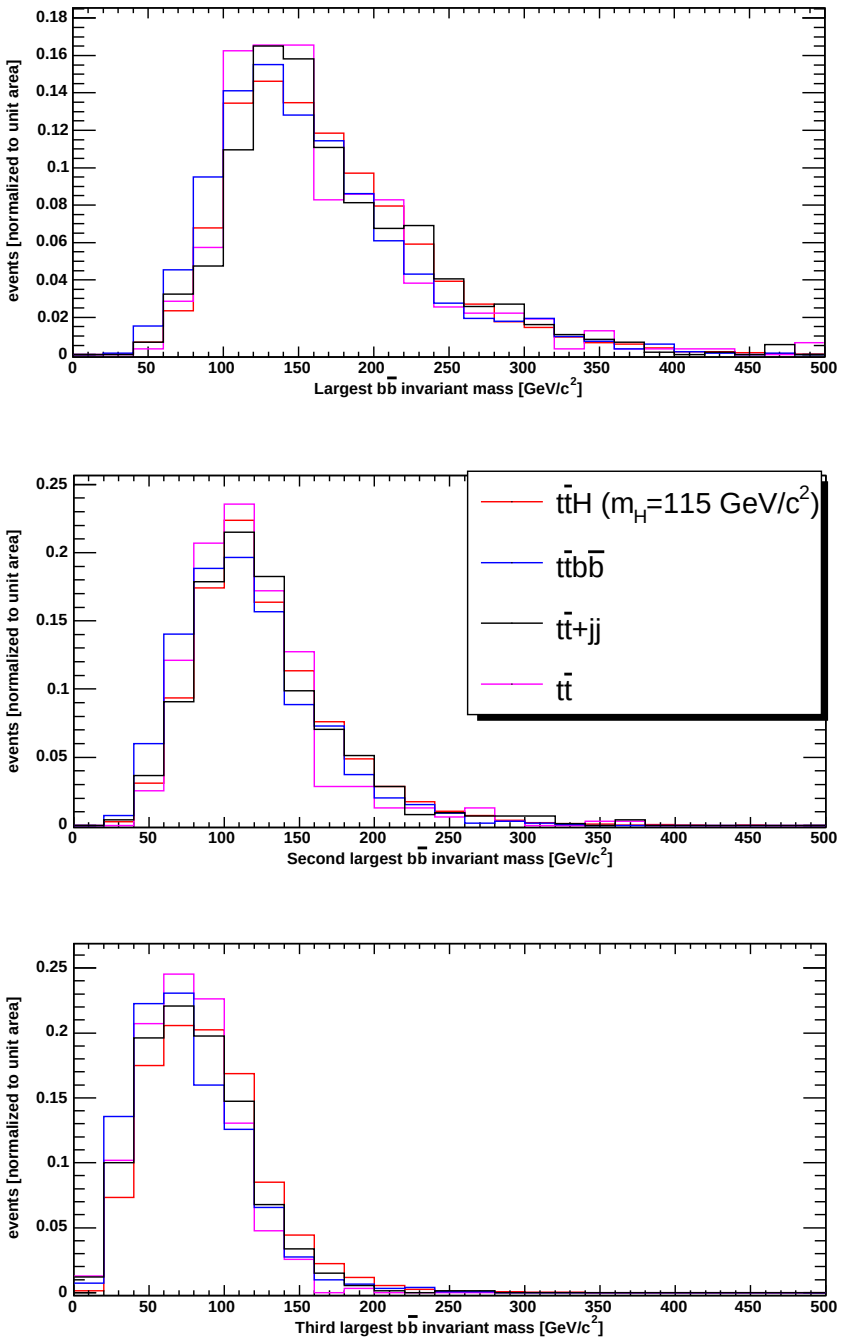

Figure 5.11: Predicted distributions of relevant processes as a function of the largest, second largest, and third largest $b\bar{b}$ invariant mass. All distributions have been normalized to unit area.

Chapter 6

Limits on the $p\bar{p} \to t\bar{t}H$ Production Cross Section

Having evaluated the $t\bar{t}H$ signal acceptance and estimated the background yields that pass our event selection criteria for the various b-tagging algorithms and jet multiplicity requirements, we proceed to evaluate the corresponding *a priori* limits. We also show the expected distributions for selected kinematic variables for $t\bar{t}H$, $t\bar{t}b\bar{b}$, $t\bar{t}+jj$, and $t\bar{t}$ events.

After doing this, we find how many events pass our event selection and set upper limits on $p\bar{p} \to t\bar{t}H$ production at $E_{CM} = 1.96$ TeV. We also show the expected and observed distributions for selected kinematic variables.

6.1 Limits and Confidence Intervals

The Poisson probability distribution function (PDF)[1] $P(n;\lambda)$ gives the probability of observing n events in a given interval when such events occur independently of one

[1] Though PDF was used to abbreviate "parton distribution function" in previous chapters, in this chapter it will be used to abbreviate "probability distribution function".

another at an average rate of λ per interval. The expression for this PDF is

$$P(n;\lambda) = \frac{e^{-\lambda}\lambda^n}{n!}. \tag{6.1}$$

In an ideal case where no background processes exist, frequentist 95% confidence level limits can be placed on an unknown parameter λ after a measurement of the event rate, n_{meas}, has been made. The probability distribution for n allows one to form a 95% confidence interval (λ_1, λ_2) so that for any value of $\lambda \in (\lambda_1, \lambda_2)$, the observed number of events will be less than a value n_{meas} 95% of the time. For an observed value n_{meas}, we can determine the value of λ for which the probability of observing the events exceeding n_{meas} is less than 5%. This value, λ_{limit} is the 95% C.L. upper limit on the unknown parameter λ.

We form these limits by performing pseudo-experiments where the expected background yield $B \pm \sigma_B$ is treated as a nuisance parameter and marginalized [46]. The signal event yields are also allowed to fluctuate, consistent with a normal distribution with the respective uncertainties. The 95% C.L. upper limit on the signal event yield, λ_{limit}, is the value that gives the number of observed events n_{meas} or greater, in only 5% of pseudo-experiments. This 95% C.L. upper limit on the event yield is converted to an upper limit on $\sigma_{t\bar{t}H} \times BR(H \to b\bar{b})$ using the equation

$$\sigma_{t\bar{t}H} \times BR(H \to b\bar{b}) < \frac{\lambda_{limit} \times BR(H \to b\bar{b})}{A_{evt}^{t\bar{t}H} \times \mathcal{L}_{int}} \text{ (95\% C.L.)}. \tag{6.2}$$

6.2 Results from the Data

The procedure that we have adopted ensures that our limit is not biased by the events in the signal region itself. All the selection criteria and the determination of the method to set limits on $t\bar{t}H$ production have been chosen without examining the observed signal yield.

With the full selection criteria finalized and the resulting background and signal yield estimates, we look at the number of events that satisfy the selection criteria. For the

Loose Combined b-tagging algorithm, we find that three events pass the full selection criteria, consistent with the background expectation of 2.16 ± 0.66 events. Of these three events, one of them also passes the selection criteria for the Tight Combined, loose SECVTX, and tight SECVTX b-tagging algorithms.

Based on the observation of three events in the signal region with the Loose Combined tagger, we proceed to set upper limits on the signal event yield. The result on this upper limit at 95% C.L. is 6.50 events. Based on the signal acceptance, we translate this into an upper limit on $\sigma_{t\bar{t}H} \times BR(H \to b\bar{b})$ at 95% C.L. The limits for this are shown in Figure 6.1 as a function of the Higgs boson mass.

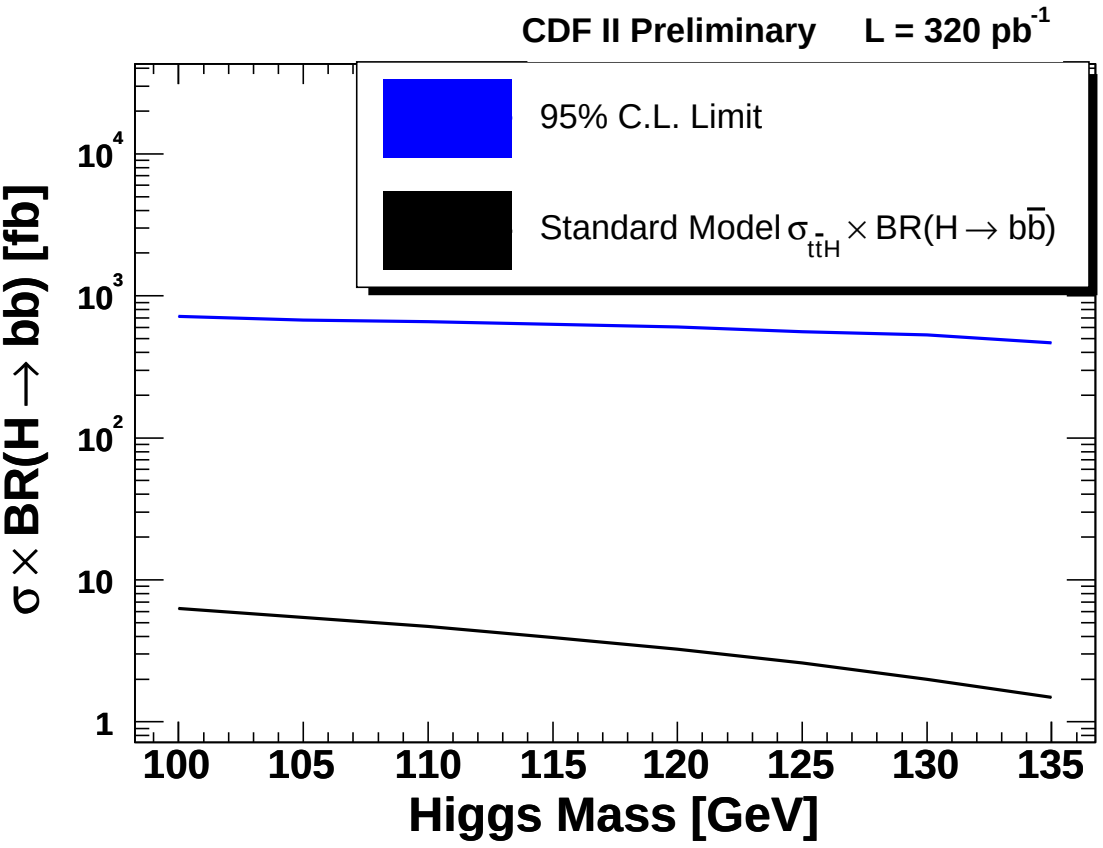

Figure 6.1: The 95% C.L. upper limit on $\sigma_{t\bar{t}H} \times BR(H \to b\bar{b})$ as a function of the Higgs boson mass.

For a Higgs boson mass of 115 GeV/c^2, we obtain $\sigma_{t\bar{t}H} \times BR(H \to b\bar{b}) < 690$ fb at 95% C.L. This is a factor of 176 times the Standard Model prediction for $t\bar{t}H$ production.

These are the first limits set for $t\bar{t}H$ production.

Based on the observation of one event satisfying all selection criteria for each of the other three taggers, we can calculate what would have been the upper limit set on the quantity $\sigma_{t\bar{t}H} \times BR(H \to b\bar{b})$ had we chosen *a priori* one of the other three taggers. This is shown in Table 6.1 for a Higgs boson mass of 115 GeV/c^2. All observed event yields are consistent with the *a priori* determination of background and signal yield estimates.

Tagger	Tight SECVTX	Loose SECVTX	Tight Comb.	Loose Comb.
Expected Event Yield	0.36 ± 0.12	1.02 ± 0.31	1.42 ± 0.37	2.20 ± 0.66
Observed Events	1	1	1	3
Upper Limit (fb)	1160	666	619	690
Ratio (Limit/SM)	297	170	158	176

Table 6.1: The 95% C.L. upper limits on $\sigma_{t\bar{t}H} \times BR(H \to b\bar{b})$ that would have been obtained for the different b-tagging algorithms for $m_H = 115$ GeV/c^2. The final limit is set with the Loose Combined tagger, since this algorithm was chosen to set the limit prior to examining the signal region.

6.3 Event Details and Kinematic Distributions

We show displays of events that have passed the full event selection criteria. These displays project the electron, muon, jets, and missing transverse energy onto the transverse plane. The event that passes the full selection criteria for all four b-tagging algorithms is shown in Figure 6.2. In addition, two other events pass the criteria for the loose Combined Tagger. These displays are shown in Figures 6.3 and 6.4.

In Figures 6.5 to 6.9, we show the expected distribution of events as a function of the following kinematic variables: the event H_T; the electron or muon p_T; the missing transverse energy $\not\!\!E_T$; the largest, second largest, and third largest b-tagged jet E_T; and

the largest, second largest, and third largest invariant $b\bar{b}$ pair mass. We also show the observed distribution for comparison. The observed event distributions are consistent with the expected distributions for all the kinematic variables shown.

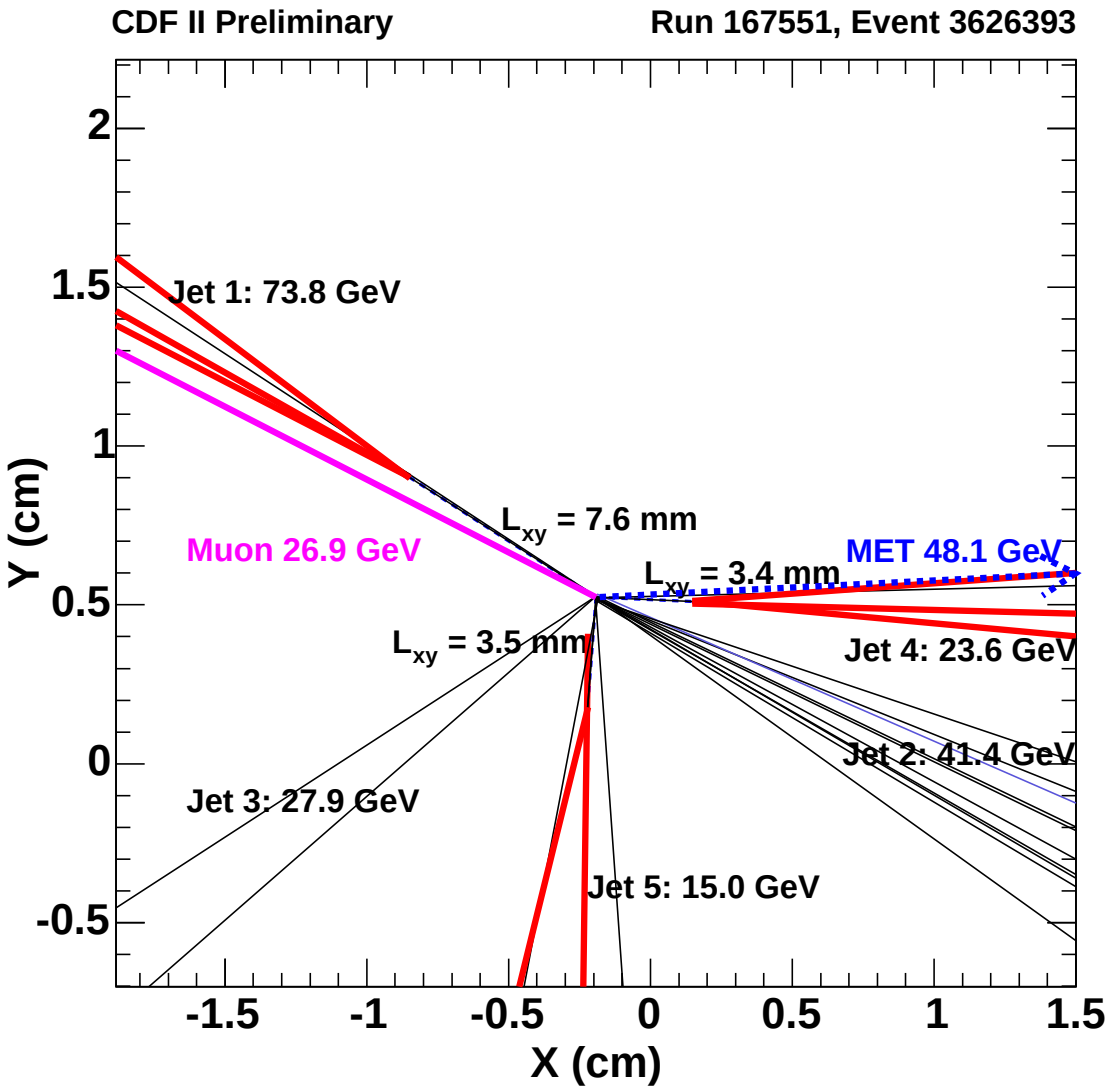

Figure 6.2: Event display of the event that passed the selection criteria for all four b-tagging algorithms. The muon is shown in purple, the missing transverse energy in blue, the jets and their associated tracks are shown in black. Tracks which are fit to a displaced secondary vertex are highlighted in red.

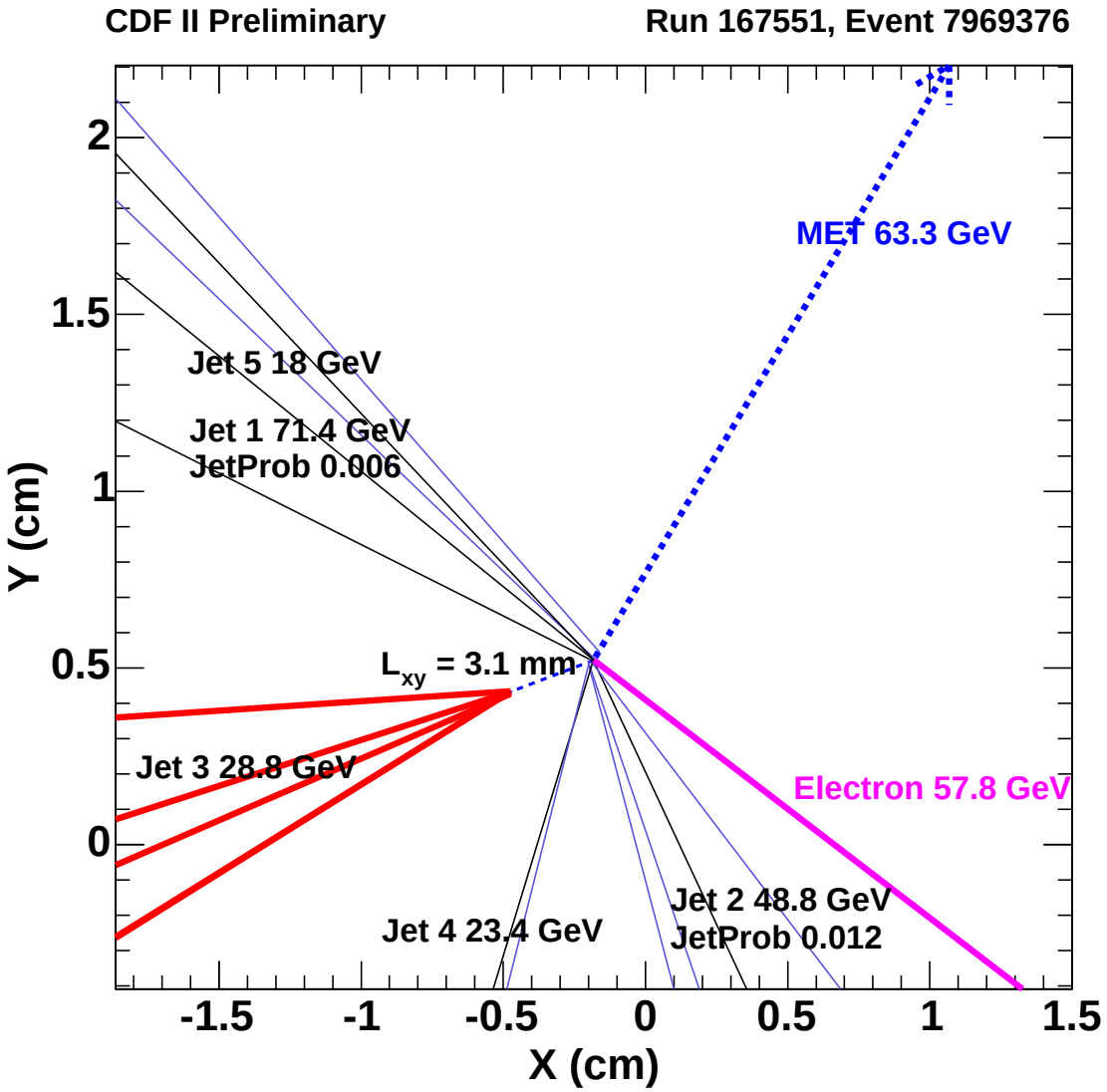

Figure 6.3: Event display of the event that passed the selection criteria for the loose Combined tagger. The electron is shown in purple, the missing transverse energy in blue, the jets and their associated tracks are shown in black. Tracks which are fit to a displaced secondary vertex are highlighted in red.

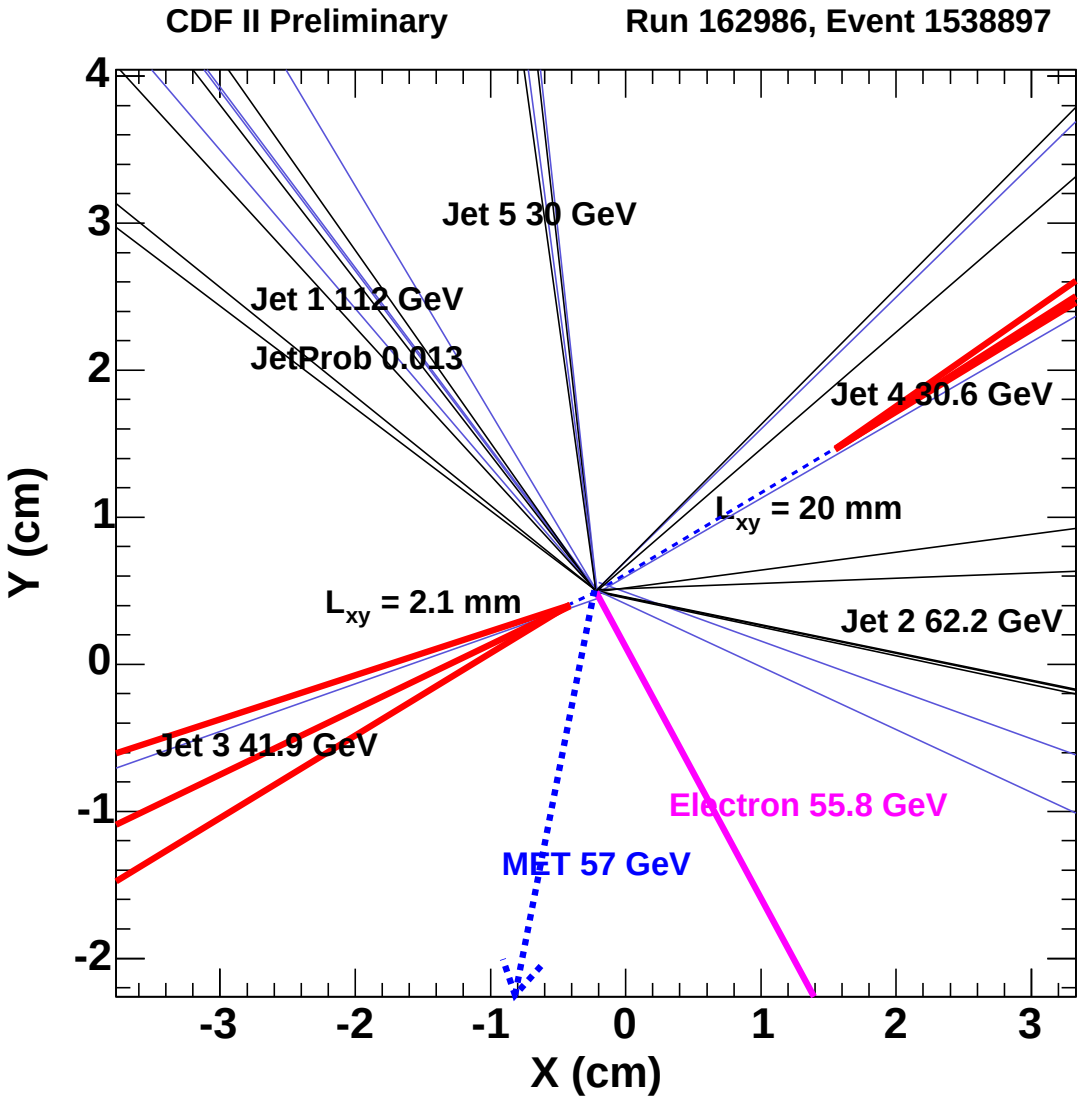

Figure 6.4: Event display of the event that passed the selection criteria for the loose Combined tagger. The electron is shown in purple, the missing transverse energy in blue, the jets and their associated tracks are shown in black. Tracks which are fit to a displaced secondary vertex are highlighted in red.

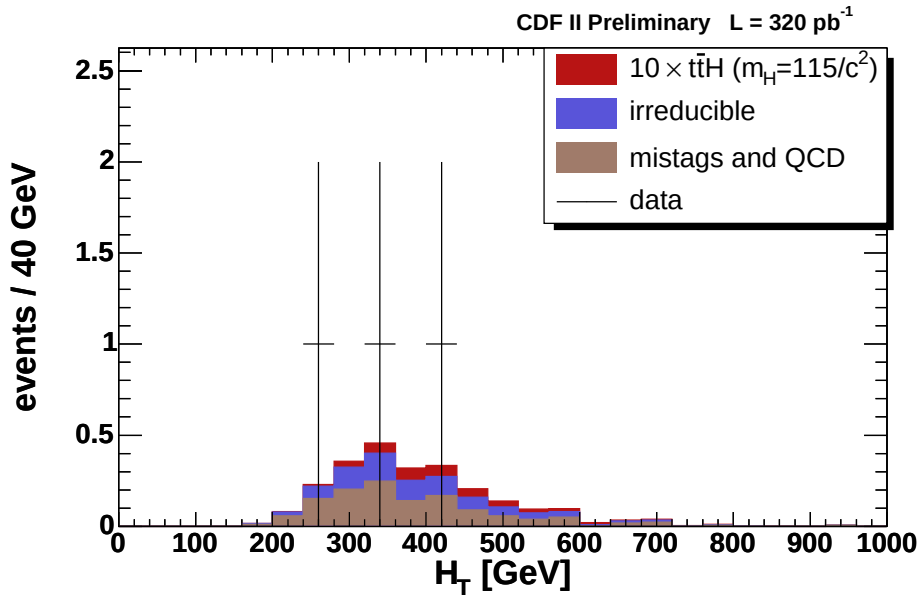

Figure 6.5: Predicted and observed distribution of events as a function of H_T.

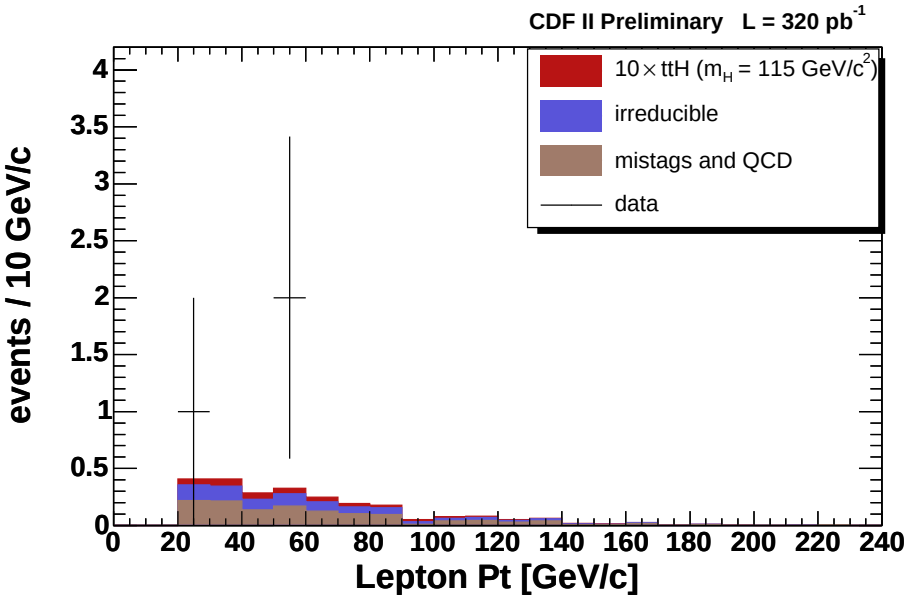

Figure 6.6: Predicted and observed distribution of events as a function of lepton p_T.

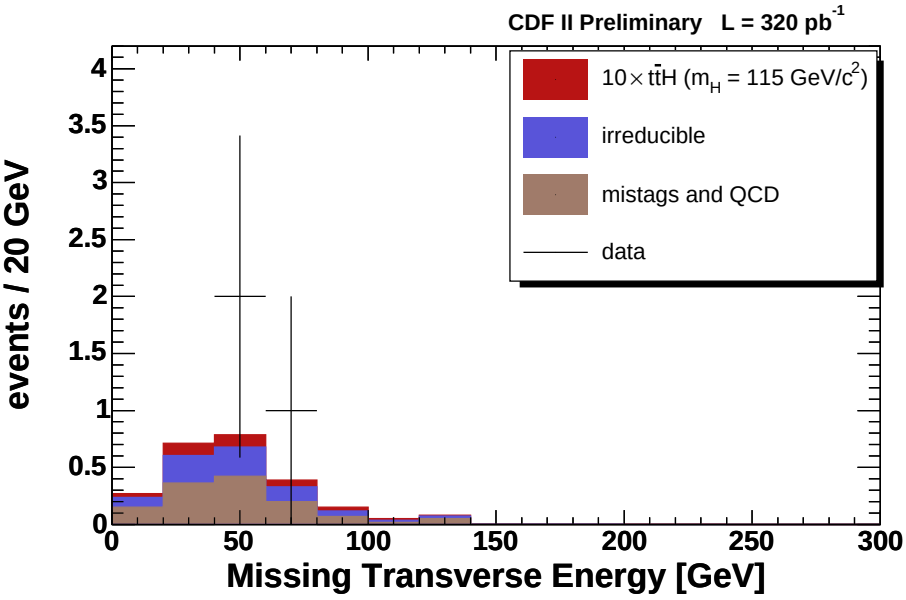

Figure 6.7: Predicted and observed distribution of events as a function of the missing transverse energy.

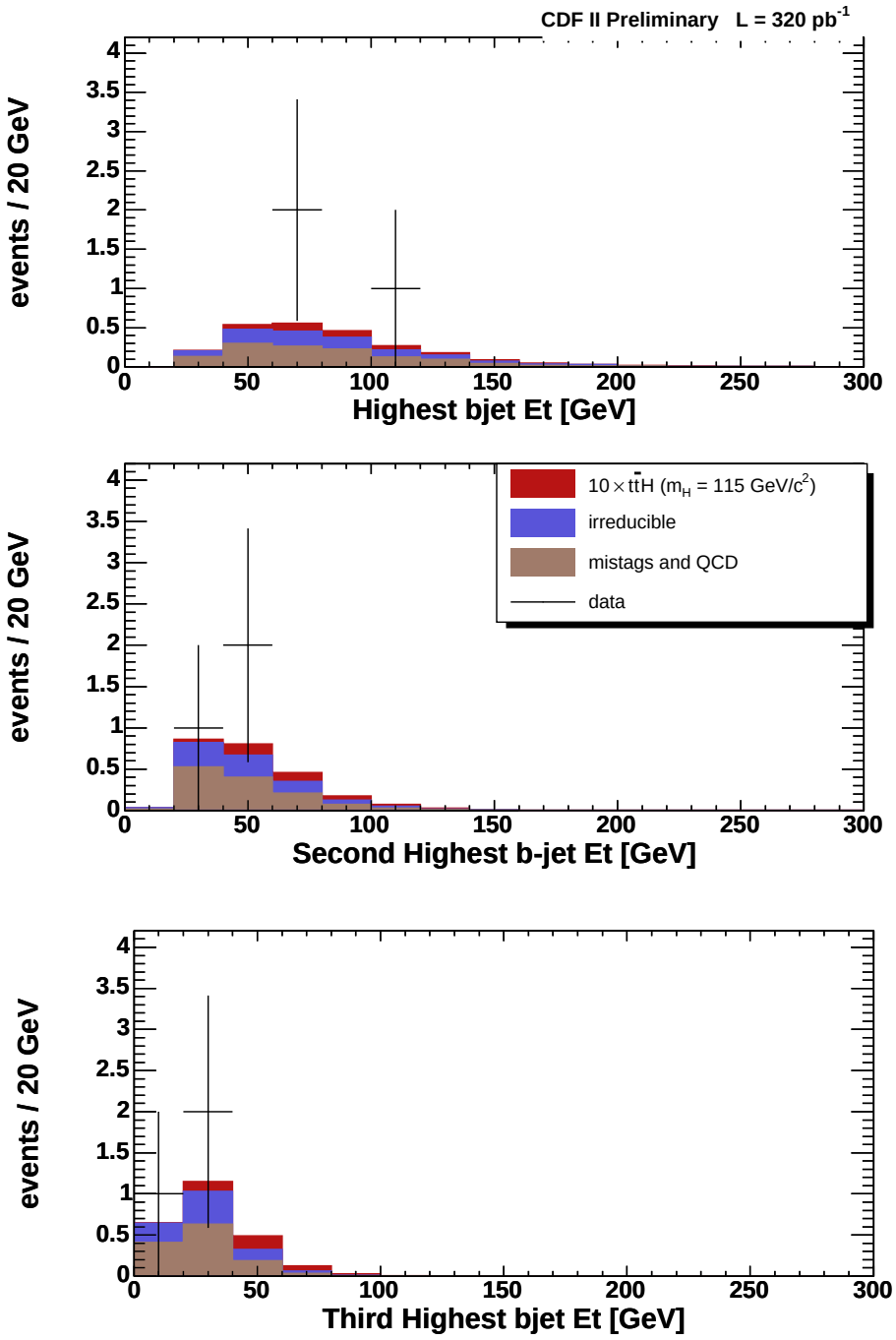

Figure 6.8: Predicted and observed distributions of events as a function of the largest, second largest, and third largest b-jet E_T.

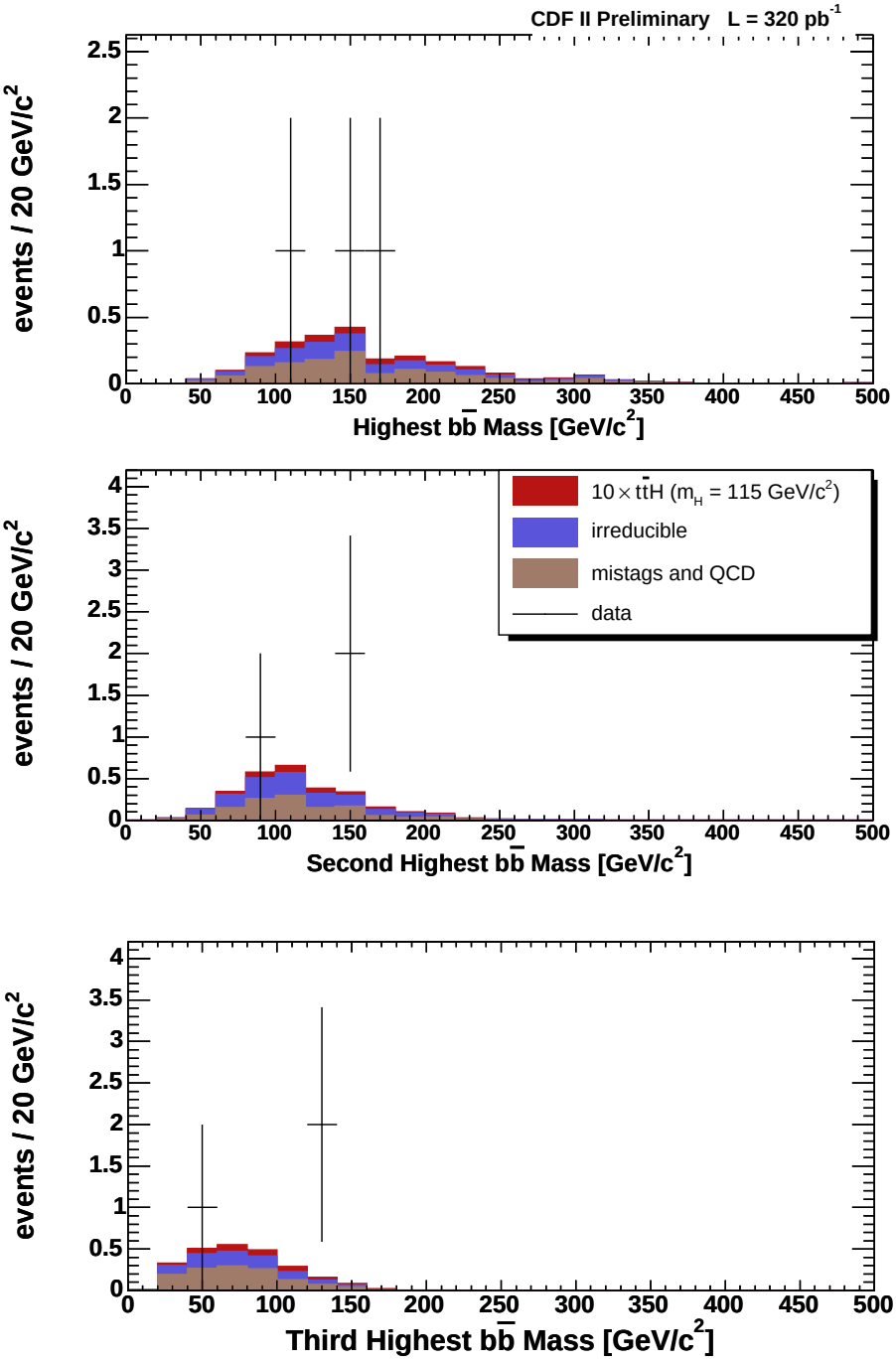

Figure 6.9: Predicted and observed distributions of events as a function of the largest, second largest, and third largest $b\bar{b}$ invariant mass.

Chapter 7

Conclusions and Outlook

In this thesis, we have reported on the results of the first search for $p\bar{p} \to t\bar{t}H$ production at $E_{CM} = 1.96$ TeV using the CDF detector using 319 pb^{-1} of data.

Events that are $t\bar{t}H$ candidates are required to pass triggers for high p_T electrons or muons. These events are subject to additional selection requirements that indicate the presence of a W boson, at least three b-jets, and a jet multiplicity of five or more. We describe four different algorithms to identify b-quark jets: the tight and loose SecVtx algorithms, and the Tight and Loose Combined tagging algorithms.

We evaluate the $t\bar{t}H$ signal acceptance to obtain the expected event yield for all four b-tagging algorithms. These event yields have been calculated as a function of the Higgs boson mass. We also evaluate the different background processes that contribute events to the signal region. This evaluation is done without examining events and their properties in the signal region itself.

For the Loose Combined tagger, we predict a signal yield of 0.037 ± 0.007 events for a Higgs boson mass of 115 GeV/c^2. The combined total of mistag, multijet, and irreducible background is predicted to be 2.16 ± 0.66 events.

We observe three events in the signal region, consistent with *a priori* expectations. Based on this observation, we are able to set an upper limit on the Standard Model

prediction for $\sigma_{t\bar{t}H} \times BR(H \to b\bar{b})$ at 95% C.L. These limits are placed as a function of Higgs mass. For $m_H = 115$ GeV/c^2, we find that $\sigma_{t\bar{t}H} \times BR(H \to b\bar{b}) < 690$ fb at 95% C.L., which is a factor of 176 above the Standard Model prediction.

The current search for $t\bar{t}H$ is both background and statistics limited. Therefore future searches at CDF for $p\bar{p} \to t\bar{t}H$ with more data will significantly improve the limit on the Standard Model production cross section times branching ratio, provided that backgrounds are further reduced without significant loss of signal efficiency.

Because a higher integrated luminosity at CDF will translate into a higher signal yield, this instantly adds sensitivity to the $t\bar{t}H$ search. This increased signal yield allows us to use more stringent event selection criteria, and improve the signal to background ratio. In addition, further improvements in b-tagging algorithms and lepton identification will aid in distinguishing the signal events from Standard Model background contributions.

With 5 fb^{-1} of data, statistical gains alone will be able to reduce the upper limit by a factor of four. This would translate into an upper limit of approximately 160 fb on the $t\bar{t}H$ cross section times the $H \to b\bar{b}$ branching ratio, or a factor of 40 above the Standard Model prediction. However, expected improvements in the b-tagging algorithm, lepton identification, and background reduction can drastically improve this projection.

Additional searches at CDF can also combine searches using all hadronic (both W boson daughters decaying hadronically) and dilepton (both W boson daughters decaying leptonically) modes to further improve sensitivity.

In addition, the Large Hadron Collider (LHC) is expected to manufacture proton-proton collisions at $E_{CM} = 14$ TeV. This centre-of-mass energy is seven times higher than that of the Tevatron accelerator. As a consequence, the Standard Model cross sections for Higgs boson production are much larger at the LHC than at the Tevatron. Figure 7.1 shows the Higgs production cross sections at the LHC. For $t\bar{t}H$ production, these cross sections are approximately two orders of magnitude larger than that at the Tevatron.

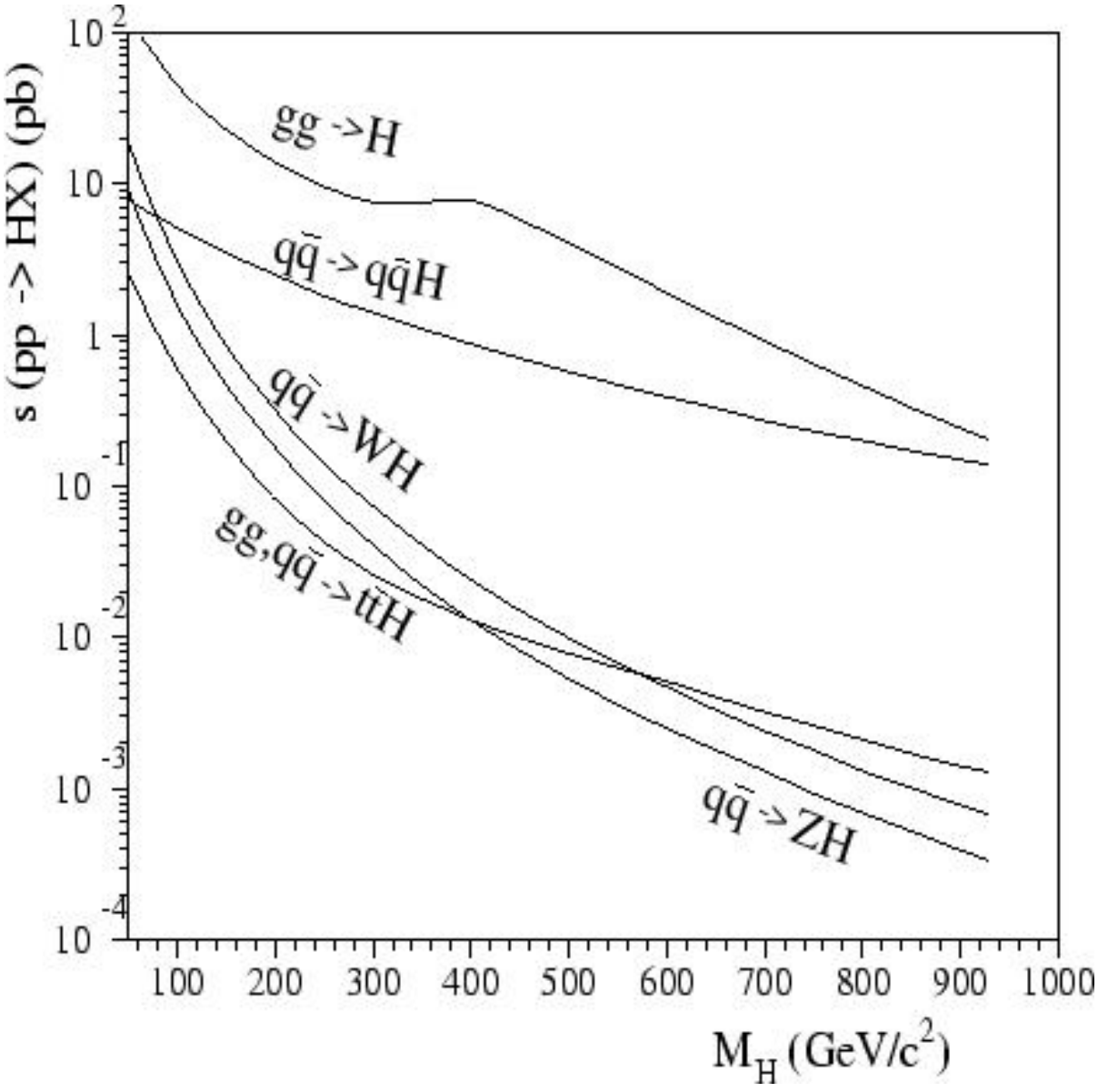

Figure 7.1: Higgs production cross sections in 14 TeV proton-proton collisions.

If the Higgs boson is not observed at the Tevatron, the ATLAS and CMS experiments at the LHC should be able to observe the Higgs boson over its entire allowed mass range with 30 fb^{-1} of integrated lumnosity. The statistical significance of a Higgs boson signal as a function of the Higgs mass for 30 fb^{-1} of integrated luminosity for ATLAS is shown in Figure 7.2. For a Higgs boson of mass between 100 GeV/c^2 to 130 GeVc^2, the $pp \to t\bar{t}H$ production mechanism is the largest contributor to the search sensitivity. The coverage

at CMS is very similar to that of ATLAS [47].

The search we have performed at CDF gives us some indication of what to expect of a $t\bar{t}H$ search at the LHC. The $t\bar{t}H$ search at the LHC is also expected to be background limited [48]. The techniques we have introduced for evaluating mistag and irreducible background can also be used in the LHC environment. To suppress $t\bar{t}b\bar{b}$ and $t\bar{t}+jj$ background, four b-jet candidates will have to be identified, and the Higgs and top quarks reconstructed.

It is expected that the Higgs boson, if it indeed exists, will be observed in the next few years. This anticipated observation of the Higgs boson will mean that all of the Standard Model particles will have been detected experimentally. But because the Higgs coupling to particles increases with larger masses, and the Higgs mass itself is sensitive to quantum effects at the energy scales of physics beyond the Standard Model, precision measurements involving the Higgs boson can lead us to understand new phenomena that have not been described by the Standard Model.

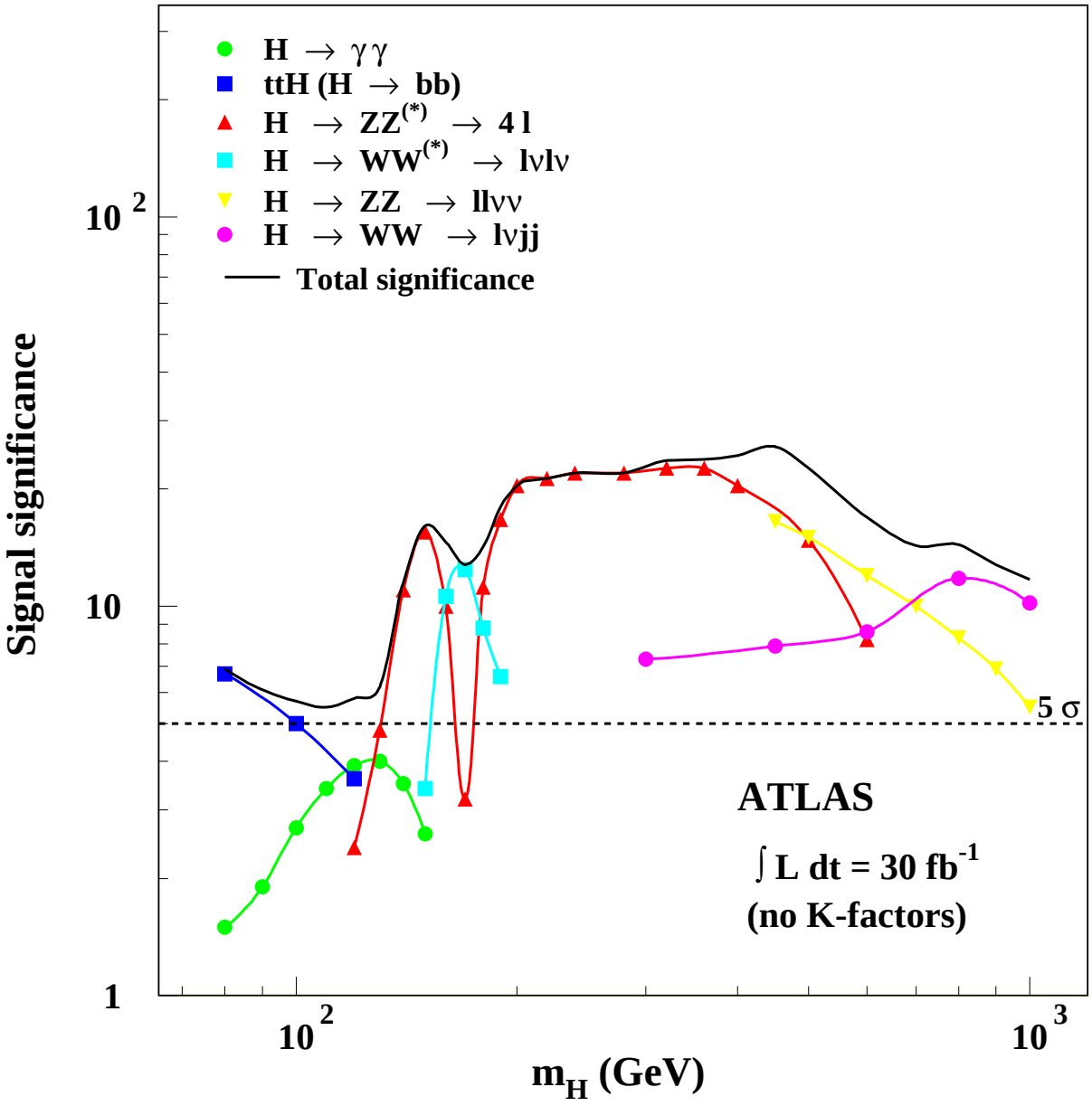

Figure 7.2: Prospects for the observation of the Higgs boson for ATLAS with 30 fb^{-1} of integrated luminosity. The statistical significance is shown as a function of Higgs mass.

Contributions

My contributions to the CDF collaboration include the:

- Operation and maintenance of the silicon vertex detector positioning system.
- Measurement of the transverse beamspot size and determination of beam parameters.
- Realtime operation of the CDF detector.
- Optimization and tuning of the SecVtx algorithm.
- Development of the Combined Tagger.
- Efficiency measurements and mistag parameterization of the Combined Tagger.
- Search for $p\bar{p} \to t\bar{t}H$ production at CDF.

Bibliography

[1] Y.-M. Yao *et al.*, (The Particle Data Group), J. Phys. G: Nucl. Part. Phys. 33 1 (2006).

[2] S. Glashow, Nucl. Phys. **22**, 579 (1961); S. Weinberg, Phys. Rev. Lett. **19**, 1264 (1967); A. Salam, *Proceedings of the 8th Nobel Symposium*, ed. N. Svartholm (Almqvist and Wiksell, Stockholm), 367 (1968).

[3] G. Altarelli, *Status of the Standard Model and Beyond*, 38th Rencontres de Moriond, hep-ph/030605 (2003)

[4] P.W. Higgs, Phys. Rev. Lett. **13**, 508 (1964); P.W. Higgs, Phys. Rev. **145**, 1156 (1966).

[5] T. van Ritbergen and R.G. Stuart, Phys. Rev. Lett. **82**, 488 (1999).

[6] ALEPH, DELPHI, L3, OPAL Collaborations, Phys. Lett. B **565** 61 (2003).

[7] A. Abulencia *et al.*, (CDF Collaboration), hep-ex/0512051 (2006); V.M. Abazov *et al.*, (DØ Collaboration), Phys. Rev. Lett. **96**, 011801 (2006).

[8] T. Affolder *et al.* (CDF Collaboration), Phys. Rev. D **64**, 052001 (2001); B. Abbott *et al.* (DØ Collaboration), Phys. Rev. D **62**, 092006 (2000).

[9] *LEP Electroweak Working Group Report*, CERN-EP-2001-021 (2001).

[10] A. Abulencia *et al.*, (CDF Collaboration), hep-ex/0510049 (2005).

[11] *LEP Electroweak Working Group*, http://lepewwg.web.cern.ch/LEPEWWG/ (2005).

[12] K. Riesselmann, hep-ph/9711456 (1997).

[13] M. Spira, hep-ph/9810289 (1998).

[14] J. Goldstein *et al.*, Phys. Rev. Lett. **86**, 1694 (2001).

[15] A. Abulencia *et al.*, (CDF Collaboration), hep-ex/0512051 (2005).

[16] W. Beenakker *et al.*, Phys. Rev. Lett. **87**, 201805 (2001); L. Reina and S. Dawson, Phys. Rev. Lett. **87**, 201804 (2001) .

[17] K.G. Chetyrkin *et al.*, Phys. Rev. D **60**, 114015 (1999).

[18] A. Roodman, physics/0312102 (2003).

[19] D. Mohl *et al.*, Phys. Rept. **58**, 73 (1980).

[20] *The CDF II Detector Technical Design Report*, FERMILAB-PUB-96/390E (1996).

[21] D. Acosta *et al.*, Nucl. Instrum. Meth. A **461**, 540 (2001).

[22] A. Abulencia *et al.*, (CDF Collaboration), *"First Measurements of Inclusive W and Z Cross Sections from Run II of the Tevatron Collider"*, submitted to PRD (2006).

[23] F. Abe *et al.*, (CDF Collaboration), Phys. Rev. D **45**, 1448 (1992).

[24] A. Bhatti *et al.*, *"Central Calorimeter Scale for Jets in CDF Run II"*, CDF Note 6930 (2004).

[25] C. Neu *et al.*, *"SecVtx Optimization Studies"*, CDF Note 7578 (2005).

[26] D. Acosta *et al.*, *"Introduction to Run II Jet Probability Heavy Flavor Tagger"*, CDF Note 6315 (2003).

[27] S. Lai and P.K. Sinervo, *"A Combined Heavy Flavour Tagger for Gen5 using SecVtx and JetProb Algorithms"*, CDF Note 7437 (2005).

[28] K. Bloom *et al.*, *"$t\bar{t}$ Event Selection and Detection Efficiency for Winter 2003 Lepton+Jets Analyses"*, CDF Note 6084 (2003).

[29] T. Sjöstrand *et al.*, J. High Energy Phys. **05**, 026 (2006).

[30] E.A. Gerchtein and M. Paulini, ECONF **C0303241**, TUMT005 (2003).

[31] R. Brun *et al.*, CERN-DD/EE/84-1 (1984).

[32] G. Grindhammer *et al.*, Nucl. Instrum. Meth. **A290**, 469 (1990).

[33] H. Bachacou *et al.*, *"Combining the SecVtx B-Tagging Scale Factors"*, CDF Note 7480 (2005); T. Spreitzer and S. Lai, *"Efficiency and Scale Factor Measurements for the Combined SecVtx and JetProb Tagger"*, CDF Note 7776 (2006).

[34] C. Hill *et al.*, *"Electron Identification in Offline 5.3.3"*, CDF Note 7309 (2005); U. Grundler *et al.*, *"High p_T Muon Recommended Cuts and Efficiencies"*, CDF Note 7956 (2005).

[35] R. Erbacher *et al.*, *"High pT Lepton ID Efficiency Scale Factor Studies"*, CDF Note 6858 (2004).

[36] V. Boisvert, *"Trigger Efficiencies for the High E_T Central Electrons"*, CDF Note 7939 (2005); U. Grundler *et al.*, *"High p_T Muon Recommended Cuts and Efficiencies"*, CDF Note 7956 (2005).

[37] G. Corcella *et al.*, J. High Energy Phys. **0101**, 010 (2001).

[38] H.L. Lai *et al.*, Phys. Rev. D **55**, 1280 (1997).

[39] A.D. Martin *et al.*, hep-ph/0307262 (2003).

[40] J. Guimaraes da Costa and S. Rappoccio, *"SecVtx Tag Matrices"*, CDF Note 7326, (2004).

[41] H. Bachacou *et al.*, *"SecVtx Tag Composition and Heavy Flavour Fraction Studies in QCD Jets*, CDF Note 6739, (2004).

[42] D. Sherman *et al.*, *"Measurement of the SecVtx Mistag Asymmetry*, CDF Note 7585, (2005).

[43] A.Sukhanov *et al.*, *"Efficiency of Jet Probability Heavy Flavor Tagger"*, CDF Note 7444 (2005).

[44] D. Acosta *et al.*, (CDF Collaboration), Phys. Rev. D **71**, 052003 (2005).

[45] M. Mangano *et al.*, J. High Energy Phys. **0307**, 001 (2003).

[46] W. Rolke *et al.*, Nucl. Instrum. Meth. **A551**, 493 (2005).

[47] *The ATLAS Detector and Physics Performance*, CERN/LHCC 99-14/15, (1999); *CMS Physics: Technical Design Report*, CERN/LHCC 2006-001, (2006);

[48] J. Cammin and M. Schumacher, *"The ATLAS discovery potential for the channel* $t\bar{t}H$, $H \to b\bar{b}$*"*, ATL-PHYS-2003-024, (2003).